PAUL SCHERRER INSTITUT

PSI

Annual Report 2017

Laboratory of Radiochemistry

Cover
Group photo March 2018 during Laboratory
excursion to Zurich Airport.

PAUL SCHERRER INSTITUT

PSI

Annual Report 2017

Laboratory of Radiochemistry

Editors

R. Eichler, A. Blattmann

TABLE OF CONTENTS

IV

EDITORIAL

Dear reader,

The Annual Reports of the Laboratory for Radiochemistry of the Paul Scherrer Institute have a long standing tradition. They provide a yearly summary of the status of the ongoing research projects and other activities of the Laboratory. Please find at hand the report for the year 2017.

2017 has been an intensive year for PSI's Laboratory of Radiochemistry (LRC) and for the Swiss Radiochemistry.

In March, the yearly retreat of PSI's Nuclear and Safety Department (NES) leaders to the beautiful city of Weggis at the banks of Lake Luzern had a special emphasis. Significant structural changes related to the creation of a new laboratory for high performance computing within the NES department have been constructively discussed. While having direct impact on the budget and personnel of most of the NES laboratories, LRC remained untouched.

In June the head of the LRC Prof. Andreas Türler has surprisingly stepped down from his PSI-related functions and retreated focusing on Bern University (UniBe) only. Within the following two month I was appointed as laboratory head ad interim for the coming year (and hopefully beyond) in an internal selection procedure. Being with LRC since almost twenty years this appointment was a great honor for me. With pleasure I took up the responsibility for a fully functioning research unit. I would like to thank at this point my predecessors and particularly the staff members of the LRC for their invaluable work within our unit for the benefit of Radiochemistry Switzerland. Clearly, my new additional tasks reveal some challenges that I am mastering with the great professional support of all my colleagues and friends at LRC officially since September 1, 2017. So thank you all for the support!

In July 6 we had a great laboratory excursion to the Black forest perfectly organized by Dorothea Schumann, Rugard Dressler and Angela Blattmann. The exciting trip included fascinating visits to a manufacture "Cafe zum gscheiten Beck" at Feldberg-Bärental where we witnessed a live show preparation of the famous cherry cake "Schwarzwälder Kirschtorte" with subsequent tasting, of course. In nice weather we hiked up to the Feldberg, and back to Feldberg-Bärental we visited the Liqueur-Museum with its fancy distillery artifacts.

In September, supported by ETH Zurich and Congressi Stefani Francini (CSF) the Swiss Heavy Elements research community (LRC and UniBe) hosted the 9th Workshop on the Chemistry of the Heaviest Elements at the marvelous conference center Monte Verità in Ascona, Ticino. I would like to thank Angela Blattmann for her great help with all the administrative and organizational tasks connected to the big success of this event. The workshop was held in a relaxed and very fruitful atmosphere and the discussed science was well received by the over 40 participants from ten countries. Unfortunately, this year our good colleague and friend the famous German nuclear chemist from Mainz University Prof. Günter Herrmann passed away. His invaluable scientific contributions and his life-long support for nuclear chemistry and radiochemistry have been honored at this workshop by a dedicated memorial session held by Prof. Jens Kratz from Mainz University.

In November/December exciting news arrived about the approval of two major research grants from swissnuclear and SNF-Sinergia in Dorothea Schumann's group. My sincere congratulations to this important success.

It is my pleasure to announce that in December 2017, Katarina Domnanich has successfully defended her PhD thesis and graduated with "summa cum laude" at the University of Bern. On May 18-th Patrick Steinegger was awarded the renowned Eduard-Adolf-Stein Prize 2017 by the Faculty of Philosophy and Natural Sciences of the University of Bern for his excellent PhD thesis that he successfully defended in 2016. This is a great honor and I would like to take the chance here to congratulate him to his success.

The new PhD students started well into their respective projects as it is shown in their status reports herein. Our young scientists performed very well at the 9th NES PhD-day winning two awards. Congratulations go to Erik Karlsson who won in the category "1st-year PhD" and to Katharina Domnanich who won the category "3rd/4th-year PhD".

Altogether, I think LRC has been very successfully demonstrating its strength and vitality despite some rough seas in the year 2017. Let's keep on!

Robert Eichler

GAS CHROMATOGRAPHIC VERIFICATION OF THE INTERACTION OF SUPER HEAVY ELEMENTS Cn & Fl WITH SELENIUM

P. Ionescu, R. Eichler (Univ. Bern & PSI), A. Türler (Univ. Bern), A. Vögele, R. Dressler (PSI),
I. Pobelov (Univ. Bern), F. Li (PSI/LMX)

INTRODUCTION

This work aims to study the chemical interaction between super heavy elements (SHE) copernicium (Z = 112), flerovium (Z = 114) and elemental selenium using gas chromatography. The research is based on the foundation that group 12 and 14 elements readily form stable compounds with the chalcogens of group 16 in nature and can be found as the minerals Tiemannite and Clausthalite [1]. If one extrapolates the stability trends of groups 12 and 14 it is expected that the formation of FlSe is energetically more favourable, while CnSe is expected to be less stable than their respective lighter homologues [2]. With increasing atomic number, relativistic effects on the electron shells begin influencing the chemistry, an effect that can already be observed in mercury and lead [3].

Previous work on this subject established values for the enthalpy of adsorption of Hg on various allotropes of Se with ΔH_{ads}^{Hg}(a-Se) < -85 kJ/mol, and ΔH_{ads}^{Hg}(t-Se) > -60 kJ/mol [4]. Furthermore, during previous on-line experiments two Cn atoms were observed on a surface with approx. 95% t-Se (trigonal allotrope) coverage, indicating against expectations, that Cn likely has an affinity for t-Se, whereas Hg does not. Due to this unexpected result current work focuses on the interaction between the grey trigonal allotrope of Se specifically with the SHE.

Through this research, our understanding of relativistic effects on the elements will be furthered and current theory and models of Cn and Fl can be confirmed and expanded upon.

EXPERIMENTAL

The experimental is composed of two stages, preparatory modelling off-line experiments and on-line experiments at the FLNR accelerator facilities in Dubna, Russia.

Off-line experiments are composed of a gas chromatography setup which models the experiments with SHE using lighter homologues. Bulk amounts of selenium were melted inside quartz tubes at 280 °C and moulded into a cylindrical column by inserting a PTFE hose into the molten selenium. The resulting vitreous black selenium was tempered at 150 °C for 1 hour to produce grey trigonal selenium (t-Se) covered columns for gas chromatography. Metallic Tl pellets were irradiated at PSI's SINQ-NIS facility to produce tracer amounts of ^{197}Hg using the reaction induced by fast neutrons ^{nat}Tl(n,xn)^{297}Tl$\rightarrow$^{197}Hg.

The resulting ^{197}Hg doped Tl pellet was then heated to 350 °C under 25 ml/min He gas flow to transport the Hg tracer over to selenium columns in order to study the interaction of elements in an isothermal chromatography. An activated charcoal or gold trap at the outlet of the column ensured trapping of any volatile mercury that was not deposited on the stationary phase. The resulting columns were then measured by the centimetre using a collimated HPGe γ-detector.

On-line experiment preparations were made by producing thin thermal vacuum deposition (TVD) Se films on glass slides and α-particle detectors to analyse them and study the selenium allotropic conversion behaviour. The substrates were placed in a TVD chamber at a pressure of <10^{-5} mbar. Ground selenium powder was then heated in a tungsten crucible and evaporated. Subsequently, it was deposited on the substrate as a red amorphous a-Se layer. Atomic force microscopy was performed to measure the Se film thickness and topology. Heat and chemical surface treatment of the deposited a-Se films was done to study and accelerate the transition to t-Se, as required.

RESULTS AND DISCUSSION

Off-line measurements:
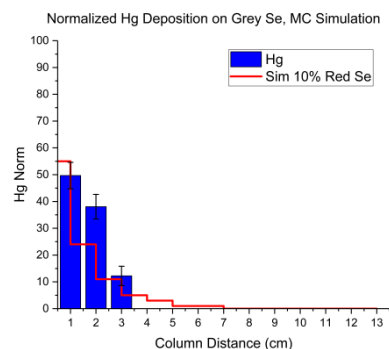
Fig. 1: Normalised mercury deposition on 13 cm selenium column (blue bars) with a Monte Carlo simulation assuming a 10% a-Se/90% t-Se surface (red line). MC parameters ΔH_{ads}(t-Se) = -45 kJ/mol, ΔH_{ads}(a-Se) = -85 kJ/mol.

Using a Monte Carlo simulation (MC) it was possible to rationalise the mercury deposition on columns. It was found that after heat treatment and conversion to grey selenium, there was still an approx. 10% coverage of red selenium on the surface. Despite best efforts, a total conversion to t-Se has not been achieved yet, leaving room for improvement on the method.

It was also found that compared to previous off-line results which used Se vapour deposition on quartz columns with a lesser surface coverage, bulk selenium behaved in the same way. This is an important discovery as there is no indication the method of

production affects the surface properties. It was also found that by treating selenium columns consistently, a reliable conversion to the grey allotrope can be achieved with <10 % variation in results.

On-line Preparation:
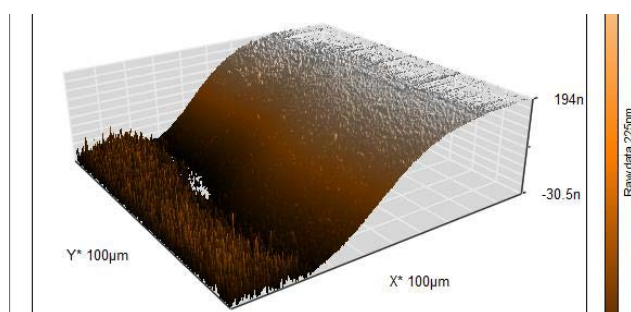
Fig. 2: Atomic force microscopy image of the α-detector quartz-selenium interface. The deposited selenium (right, elevated plateau) shows a very smooth surface with a thickness of approx. 225 nm.

The freshly deposited a-Se layers showed a high smoothness with a root mean square surface roughness of 1.36 nm. A smooth surface is beneficial, as it ensures an undisturbed gas flow through the column when performing a chromatography.
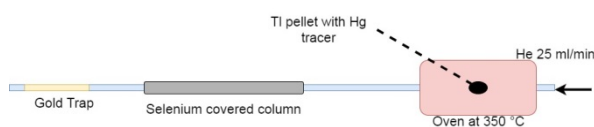
Fig. 3: Isothermal chromatography setup showing the 25 ml/min He flow over an oven at 350 °C with Hg tracer. Selenium column can consist of Se covered quartz slides or a solid selenium tube. The gold trap captures any Hg that did not deposit on the column.
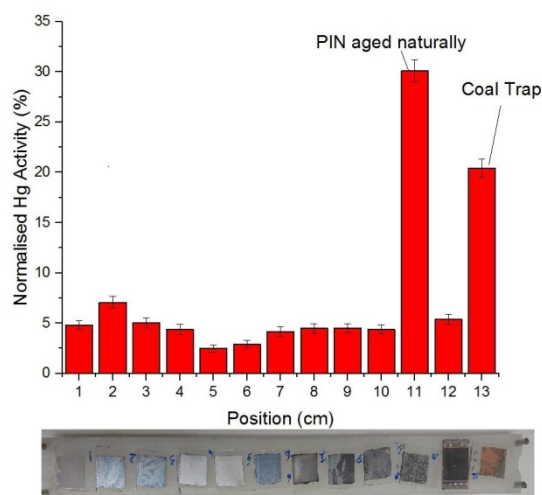
Fig. 4: Normalised mercury deposition pattern on grey selenium glass slides (top). The selenium glass slide column (bottom).

The conversion from a-Se to t-Se was found to be most successful when heating up samples at 2.5 °C/min from room temperature to 70 °C and keeping them at this temperature for 24 hours. The resulting selenium samples were visibly grey, reflective to light but still appeared red transparent when shining light through them (see Figure 3). The deposition of the tracer [187]Hg on to the produced selenium samples showed a consistent deposition pattern. Despite visible differences in the surface crystallisation pattern the deposition and transformation was obviously quite reliable. Currently, some mercury deposits on all samples which can be attributed to an incomplete conversion from a-Se to t-Se, therefore leaving reactive sites for mercury to adsorb. Alternatively, it is possible that there are open, unlinked t-Se chain ends which act as active binding sites to mercury. This will be further investigated by prolonging the heating cycle at 70 °C for better conversion.

X-ray diffraction measurements were performed on TVD samples, as well as samples converted by annealing (Fig. 5).
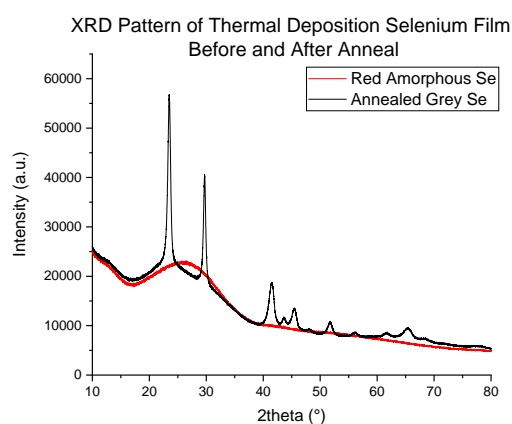
Fig. 5: XRD signal of TVD selenium film on glass slide, before and after heat treatment.

As expected, the amorphous TVD layer resulted in a broad signal. By contrast, the annealed selenium sample gave multiple distinct peaks, which were found to be characteristic of grey t-Se.

Additionally, an alternative selenium conversion pathway was discovered, by exposing a freshly prepared red amorphous selenium film to the fumes of a 4:1 mixture of 1,2-diaminoethane and ethane thiol. The extent of conversion and chromatography results will be explored in the near future.

_____

[1] N. Wiberg, A. F. Holleman, *Inorganic Chemistry*, Academic Press, 2001, 1st ed. pp. 540 – 627.
[2] N. Chiera, Towards the Selenides of the Superheavy Elements Copernicium and Flerovium, PhD Thesis, University of Bern, 2016, p. 79.
[3] L. J. Norrby, J. Chem. Educ. **68**, 110 (1991).
[4] N. Chiera et al., Ann Rep. Lab. of Radio-& Environ. Chem., Univ. Bern & PSI (2014).

IMPROVEMENT OF ISOTHERMAL VACUUM CHROMATOGRAPHY TO DIFFERENTIATE BETWEEN [211]Pb AND [211]PbO

B. Kraus, R. Eichler (Univ. Bern & PSI), P. Steinegger (JINR), A. Türler (Univ. Bern)

The isothermal vacuum chromatography (IVAC) of Pb on quartz was further investigated and one of the challenges was to obtain and secure the elemental state of [211]Pb. Our approach to solve this problem was to introduce a Ta foil around the [211]Pb source comprised of a Pt/[227]Ac intermetallic. The source is placed in the hottest region of the setup, with a surrounding temperature of at least 950 °C [1].

At these elevated temperatures, tantalum is an excellent oxygen getter material. Additionally, we tried to reduce the possible oxygen interactions of the elemental Pb even further by pre-heating up the quartz tube in vacuum to eliminate a substantial amount of silanol groups on the surface [2], and recently, we were able to seal the setup and improve the vacuum by an order of magnitude to 2E-6 mbar, thus substantially reducing the amount oxygen in the entire system.

With such low amounts of residual gases inside the system, we think the elemental state of Pb is ensured even over longer measurement campaigns (longer than two weeks). In the past, we observed an exponential decrease in the count-rate within the first two weeks to a non-measurable level with an apparent half-life of about 50 hours, likely due to the oxidation of the tantalum.

The IVAC of Pb on quartz was investigated again to determine the adsorption enthalpy (ΔH_{ads}). A Monte Carlo simulation (MCS) [3] was used to obtain expectation data based on presumed ΔH_{ads} values, which were later compared to experimentally measured results. The anticipated ΔH_{ads} of Pb on quartz is expected to be in the range of -160 to -205 kJ/mol [4]. Accordingly, the breakthrough curve of Pb on quartz is expected in the temperature range between 300 °C and ca. 600 °C (see Fig. 1).
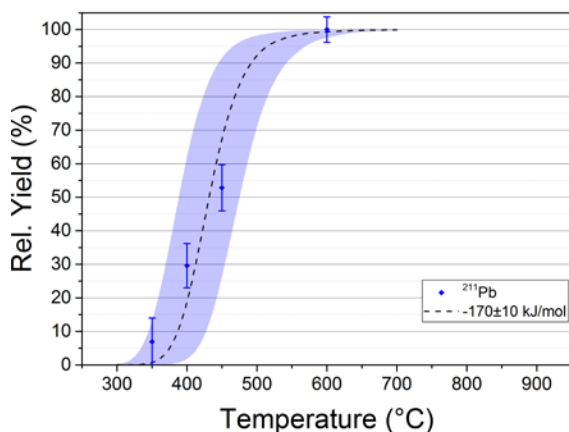
Fig. 1: Determination of the ΔH_{ads} of Pb on quartz by comparing the obtained experimental (blue symbols) values to simulated data (black dotted lines and blue shaded area).

As can be seen in Fig. 1 the experimentally determined values fit the simulated breakthrough curve of ΔH_{ads} = -170 kJ/mol within the range of ± 10 kJ/mol. This finding matches the expectations very well, and proves that IVAC is a suitable method to determine adsorption enthalpies of volatile elements.

However, not only volatile elements can be investigated, but also volatile compounds, such as e.g. PbO, dependent on their thermal stability in vacuum. As previously described, we observed several times an exponential decrease in count-rate within in two weeks' time due to small oxygen ingress. The temperature of the isothermal column was elevated to above 800 °C – a region where PbO should be volatilized [4]. Indeed we observed that the count rate of [211]Pb was increasing again (cf. Fig. 2) indicating higher transport efficiency due to the additional transport of [211]PbO.
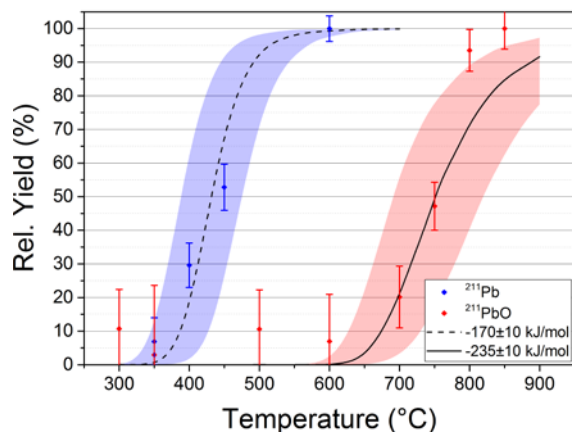
Fig. 2: The two observed species of elemental [211]Pb and the compound [211]PbO, with their determined adsorption enthalpies (Data of [211]PbO adapted from [4]).

Therefore, we conclude that even in IVAC care has to be taken to achieve as low as possible partial pressures of reactive gases (e.g. oxygen) to prevail elemental states of the species analyzed. Otherwise, this also shows that vacuum chromatography of simple molecular species might be possible, by adding minute amounts of certain reactive gases to the system.

_____
[1]   B. Kraus et al., Ann Rep. Lab. of Radiochem., Univ. Bern & PSI, 7 (2016).
[2]   L. T. Zhuralev, Colloid Surface A, **173**, 1 (2000).
[3]   I. Zvara, *The Inorganic Radiochemistry of Heavy Elements*. 1st Ed. (2008).
[4]   B. Kraus, *Isothermal vacuum chromatography of lead (Pb) on quartz (SiO₂)*. Masterthesis, Univ. Bern (2017).

OPTIMIZATION OF THE ISOTHERMAL VACUUM CHROMATOGRAPHY-SETUP FOR SUBSECOND CHEMISTRY OF SUPERHEAVY ELEMENTS

B. Kraus, R. Eichler (Univ. Bern & PSI), D.P. Herrmann (PSI), P. Steinegger (JINR), A. Türler (Univ. Bern)

The successful «proof-of-principle» experiment in 2014 conducted by P. Steinegger et al. [1] paved the way towards chemistry experiments with superheavy elements in subsecond time scales. The adsorption enthalpy of Tl on quartz (SiO_2) was determined as a homolog for its superheavy counterpart nihonium (Nh, element 113).

In order to be applicable for superheavy elements, such as the mentioned Nh, the setup needed to be optimized for maximum speed. At the same time the amount of adsorption possibilities of the species on the isothermal chromatographic surface has to be kept reasonably high to achieve "equilibrium-like" conditions - an important prerequisite for the determination of thermochemical data from the experimental results. In chromatographic systems, the numbers of adsorptions on a surface and the adsorption enthalpy determine the retention, thus having a direct impact on the decay loss of the short-lived species, while performing chromatographic experiments. Therfore, for IVAC a compromise has to be found for the geometrical parameters of the isothermal column.

For the optimization of the current setup Monte Carlo simulations (MCS) relying on Zvara's model [2] were employed, which used ^{284}Nh as a benchmark isotope (with the following properties: $t_{1/2} = 0.97$ s, predicted ΔH_{ads} on quartz ≈ 60 kJ/mol [3], $T_{iso} = 1000$ °C).

In order to find the best compromise for yield and resolution of the chromatography, but also respecting the technical constraints of the existing setup, it was decided to give yield priority over chromatographic resolution. Hence, the «optimum» for our setup was chosen to be a column with a length of 40 cm and a radius of 1.5 cm.

Tests with these newly defined parameters of the column, the MCS showed that we would not observe any retention on quartz, but on gold (cf. Fig. 2), suggesting that we should use a gold surface rather than quartz for a future experiment with elemental Nh. From the maximum yield achievable for ^{284}Nh in the MCS, we also could calculate the mean transport time of ^{284}Nh through the system (neglecting the diffusion from the hot catcher). This mean transport time is 195 ms, which is compared to other methods an advancement that opens up the subsecond range for the investigation of superheavy elements with half-lives below one second. However, an experimental prove is still missing.
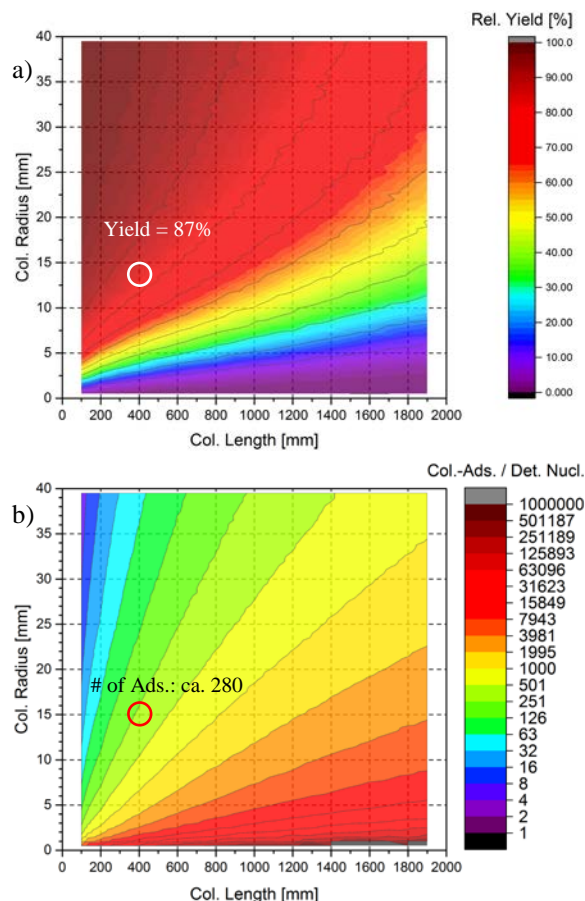
Fig. 1: a) The yield is plotted as function of radius and length of the column. The curving of the lines can be explained by the fact that the hot catcher volume (HCV) was included in the simulations and thus a more efficient transport between the HCV and the isothermal column is obtained at larger radii of the column. **b)** The number of adsorptions on the column per detected nuclide is plotted as function of radius and length of the column. Here, the adsorptions within the HCV are neglected.

In order to test the suitability of the optimizations, the setup was brought to the Hot Lab of the Department of Chemistry and Biochemistry at the University Bern. A weak ^{252}Cf-source was directly coupled to the setup and serves as a continuous nuclide generator for volatile (and non-volatile) fission products (FPs). The very short-lived volatile fission products shall indicate, whether subsecond transport times can be achieved as predicted by the MCS. The FPs vacuum chromatographic transport yield will be determined by measuring their activity at the end of the chromatography column using a shielded γ-spectroscopy HPGe detector (see Fig. 3).
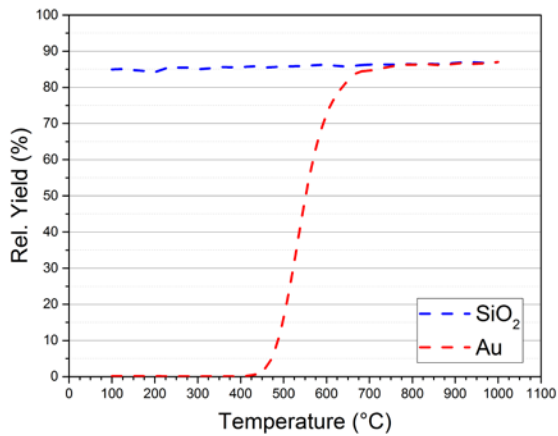
Fig. 2: The breakthrough curves obtained by MCS for the IVAC of ^{284}Nh on SiO$_2$ (blue) and Au (red). The maximum yield achieved with a column specific above, is 87% for both surfaces.
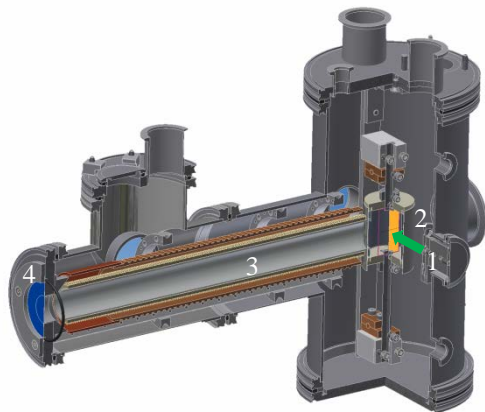
Fig. 3: Schematic of the optimized IVAC. The quartz column was enlarged to a diameter of 3 cm and a length of 40 cm, with **1** being the ^{252}Cf-source (the green arrow symbolizes the recoil path of the FPs to the HC), **2** the HCV with a hot Hf-foil, **3** the new and bigger isothermal quartz column, and **4** the detection flange, where a γ-detector can be placed in front of the opening of the column end to measure the FP's arriving there.

Furthermore, the influence of the hot catcher material on the transport yield will also be investigated by using various other metals. Maybe Hf is not the best choice for the hot catcher (HC), so we plan to test other high melting metals, e.g. Zr, Nb, Mo, W, Ni etc. based on recommendations given in [4,5].

_____

[1]   P. Steinegger et al., Journal of Physical Chemistry C, 120, 13 (2016).
[2]   I. Zvara, *The Inorganic Radiochemistry of Heavy Elements*. 1st Ed. (2008).
[3]   V. Pershina, Journal of Physical Chemistry C, 120, 36 (2016).
[4]   D. Wittwer et al., Radiochim. Acta 101(4) 211-219 (2013).
[5]   D. Wittwer et al., Nucl. Instr. & Meth. Phys. Res. B 297, 86-93 (2013).

BEHAVIOR OF DIAMOND-BASED RADIATION DETECTORS IN HIGH TEMPERATURE ENVIRONMENTS

B. Kraus, R. Eichler (Univ. Bern & PSI), P. Steinegger, N.V. Aksenov (JINR), R. Dressler, D.P. Herrmann (PSI), A. Türler (Univ. Bern), C. Weiss, E. Griesmayer (CIVIDEC Instrumentation GmbH)

With the development of the on-line isothermal vacuum chromatography (IVAC), it was also necessary to find a suitable replacement for silicon-based detectors. Such detectors work only in a complete dark environment up to temperatures of ca. 40 °C. However, detectors used in IVAC should be able to withstand not only higher temperatures, but also intense infrared and visible light loads, as occurring in the vicinity of hot surfaces. For this reason, detectors based on diamond material instead of silicon were designed [1-3]. The unique properties of diamond allow such sensors to be operated in high temperature environments up to the current limit of around 200 °C to 300 °C [2-5]. In contrast to the limit found by Steinegger et al. [2, 3] the theoretical limit for diamond sensors are approximately 1000 °C [6].

Herein, we present a study aiming at the further exploration and possible surmounting of this upper temperature threshold. A test setup for α-particle measurements was developed, which allowed the heating of diamond-based sensors up to temperatures of 600 °C (cf. Fig. 1). The Cr/Au-coated sensor was encapsulated in a RF-resistant printed circuit board (PCB), within which the sensor was contacted and held in place by a CuBe-spring. An ^{241}Am-source with an activity of 15 kBq was used as an α-source. Two PCBs were employed: one was made of polyimide ($T_{max} \approx 280$ °C), whereas the other one was made of alumina ($T_{max} > 280$ °C). All measurements were carried out with dedicated electronics from CIVIDEC Instrumentation GmbH and a LeCroy WaveRunner 640Zi Oscilloscope. The temperature was measured close to the enclosed diamond sensor with a type-K thermocouple inserted sideways in the PCB-structures.

In a first step, the temperature dependent charge collection with positive and negative biasing was investigated (see Fig. 2). For these measurements the polyimide PCB and the broadband current amplifier C2 (2 GHz, 40 dB, CIVIDEC Instrumentation GmbH) were employed.

Furthermore, Fig. 2 shows that the charge collection of holes (h^+) and electrons (e^-) is very stable up to a temperature of 220 °C. At higher temperatures however, it was not possible to obtain any signals for the holes, whereas the electrons were still measureable. By going to lower temperatures again, the detector performance fully recovered (Fig. 2, blue and yellow points), thereby confirming a reversible temperature effect in the diamond itself.
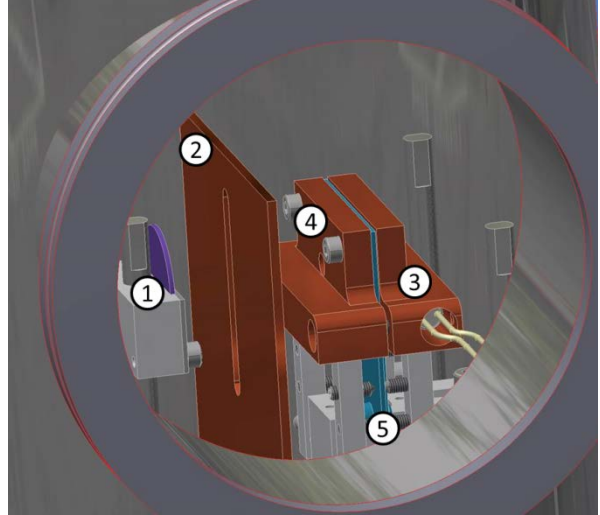
Fig. 1: Schematic of the setup used for the studies of a diamond-based detector in high temperature environments, with **1** being the ^{241}Am-source, **2** a copper heat shield with collimator to minimize the heat load of the ^{241}Am-source, **3** the copper heating block with inserted heating cartridge, **4** front copper heating block with collimator and **5** the PCB with the detector.
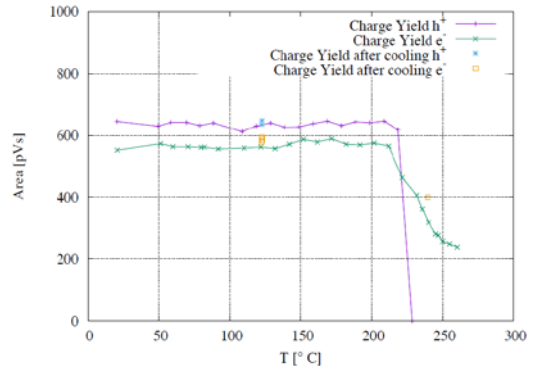
Fig. 2: The average area of the charge yield is plotted as function of the temperature. The purple line and blue crosses indicate the transmission of holes (h^+) through the diamond bulk, whereas the green line and yellow squares show the conduction of electrons (e^-).

Following the charge collection measurements, the spectroscopic properties were investigated using the spectroscopic shaping amplifier Cx (CIVIDEC Instrumentation) in combination with the diamond enclosed in the polyimide PCB. Relevant parameters such as charge amplitude and area, the FWHM, as well as the dark current were measured in dependence of the temperature (50 °C to 280 °C). Due to the limitation of positive bias for using the Cx amplifier, we could only investigate e^- conductivity. The investigated parameters were stable up to a temperature threshold of 220 °C. At higher

temperatures the amplitude, area and resolution decreased (see Fig. 3 a) whereas at the same time the dark current increased by almost two orders of magnitude within the range of 220 °C to 280 °C (see Fig. 3 b).
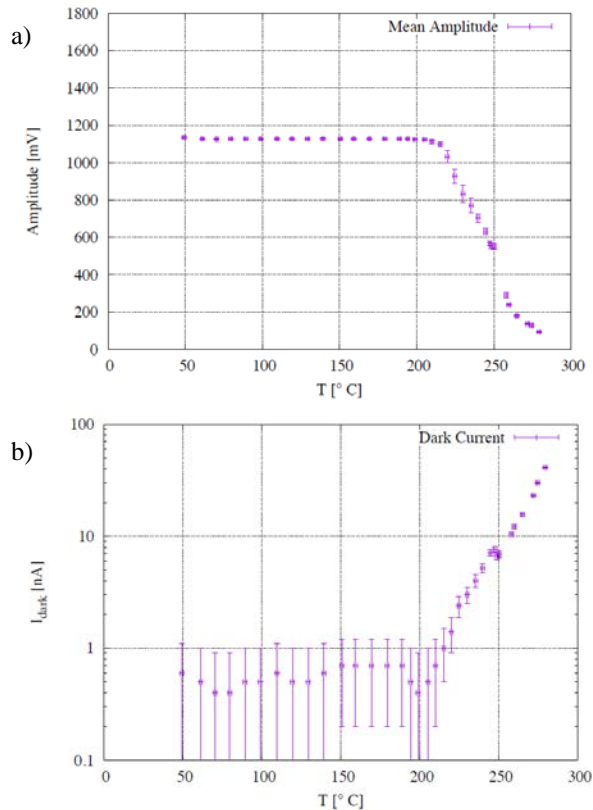
Fig. 3: a) Signal amplitude as function of temperature. **b)** Dark current as function of temperature. Both measurements were performed simultaneously.

In the final part of this study, we investigated the charge deposition at temperatures up to 500 °C. For these measurements the alumina PCB was used (cf. Fig. 4).
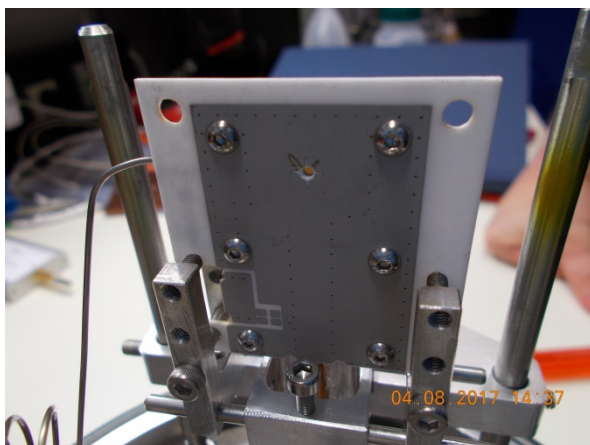
Fig. 4: The alumina PCB-structure containing the diamond-based sensor, mounted in the setup, without the heating cartridges; the type-K thermocouple can be seen on the left hand side.

These measurements were again recorded with the spectroscopic shaping amplifier Cx. Up to a temperature of 290 °C the bias was set to +500 V,

while at higher temperatures the bias had to be stepwise decreased down to +200 V at 450 °C and even +1 V at 500 °C in order to obtain a reasonable signal.

The herein found results confirm earlier findings with a drastically deteriorating performance at temperatures above 200 °C [3]. As concluded in [3], the reversibility of this degradation of the performance points to an intrinsic effect in the diamond material itself rather than to issues with the electrical contacting. Most probably responsible for this behavior are the impurities in the diamond structure. However, further investigations are needed and envisaged to clarify the exact processes behind this still unexpected temperature threshold.

_____
[1] Wort, C. H. J. et al., Mater Today **11**, 22 (2008).
[2] P. Steinegger et al., Ann Rep. Lab. of Radio-& Environ. Chem., Univ. Bern & PSI, p. 6 (2014).
[3] P. Steinegger et al., Nucl Instrum Meth A **850**, 61 (2017).
[4] Isberg, J. et al., Phys Status Solidi A **202**, 2194 (2005).
[5] Kumar, A. et al., Nucl Instrum Meth A **858**, 12 (2017).
[6] Vescan, A. et al., 55th Annual Device Research Conference – Digest 1997, 40-41, (1997).

GETTING INSIGHT INTO METAL-CARBONYL-COMPLEX FORMATION UNDER SINGLE-ATOM-CHEMISTRY CONDITIONS

Y. Wittwer, R. Eichler (Univ. Bern & PSI), D.P. Herrmann (PSI), A. Türler (Univ. Bern)

The first successful synthesis of Seaborgium-Hexacarbonyl, $Sg(CO)_6$, in 2016 by Even et al. [1] did pave the way to an entire new series of compounds, the transactinide carbonyl complexes. However, following experiments targeted at determining the First-Bond-Dissociation-Energy (FBDE) of this new compound appeared to be influenced by low chemical yields and the formation of yet unknown side-products, both not only strongly disturbing the investigation of $Sg(CO)_6$, but likely also challenging the synthesis of the other possible transition metalcarbonyl complexes including Bh, Hs, Mt that are expected to be affected by similar problems.

In 2016, theoretical preparations for the construction of a model system, allowing the studying of metal carbonyl complexes formed by short lived isotopes, were already presented. [2] In the meantime, the system was successfully completed and installed at the University of Bern. Briefly, the system is based on a ^{252}Cf fission source that is producing short-lived Mo-, Tc-, Ru- and Rh-isotopes as fission products serving as models for their corresponding chemical homologues including the lighter transactinides. The fission products are recoiling from the source into a reaction chamber, which is constantly flushed with a gas mixture containing carbon monoxide. In this chamber, volatile carbonyl complexes are formed and transported by a gas stream to a charcoal trap, where they are adsorbed until the decay of the metal atom is registered by a HPGe γ-detector.
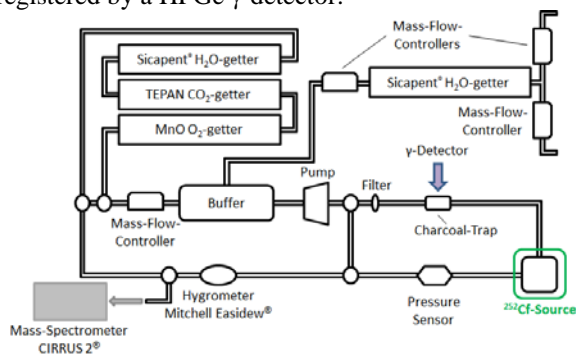
Fig. 1: Schematic representation of the model-system used for studying the formation of metal carbonyl complexes under single atom chemistry conditions.

The main focus of the system depicted in Fig. 1 lies in the establishment of well controlled and reproducible reaction conditions in order to avoid disturbing effects originating for example from varying amounts of impurities in the used reaction gas. For this purpose, extensive and permanent gas-purification as well as a in-situ monitoring of the gas quality is mandatory. The ^{252}Cf-source is additionally modified to allow for controlling the kinetic energy of the recoiling fission products. By using a wheel-like construction, it is possible to place aluminium foils with different thicknesses between the ^{252}Cf-source and the reaction chamber, thereby reducing the kinetic energy as a function of the used foil. [2]

Using this new setup, a series of measurements was performed targeted at investigating the influence of various reaction parameters on the carbonyl-complex formation reaction. The dependency on pressure, varied kinetic energy as well as on various gas mixtures was investigated in terms of the maximum carbonyl yield obtainable under each condition.

The relative yield was calculated using the following formalism:

$$Relative\ Yield_{i,d} = \frac{A_i}{\alpha_i * P_d * C_i}$$

where A_i is the activity of isotope i measured on the charcoal trap and corresponding to the amount of carbonyl complex transported, α_i is the cumulative fission yield of isotope i, P_d the total number of fission products entering the reaction chamber as a function of the aluminium foil thickness d and C_i is a correction factor including mostly transport losses. Especially the determination of P_d appears to be crucial, since it is very dependent on the thickness of the aluminum foil inserted between ^{252}Cf-source and reaction chamber. For the data shown in Fig. 2, experimental values obtained by using thick catcher foils and quantitative γ-spectroscopy with long-lived ^{252}Cf fission products where used for the evaluation of P_d. Those measured values are expected to be rather uncertain and are the main reason for the large standard deviations shown as error bars in Fig. 2 and Fig. 3. An additional method based on α- and SF-fragment spectroscopy will be used in the near future to improve the accuracy of P_d.

Fig. 2 depicts a very preliminary example of the data obtained with the new setup. The y-axis depicts the relative yield of carbonyl complexes produced under the given reaction conditions. The x-axis shows the thickness of the aluminium-foils used for reducing the kinetic energy of the recoiling fission products. Shown are data for ^{104}Mo and ^{107}Tc as representatives for elements of groups 6 and 7 of the periodic table. For low pressures, a rather strong dependency on the kinetic energy seems to exist, indeed. However this dependency vanishes quickly if the overall pressure inside of the reaction chamber is increased, leading however to a poorly understood decrease in overall yield which cannot be related to decay losses due to the transport time only, since e.g. the half-life of ^{104}Mo exceeds the transport time in any case by far.
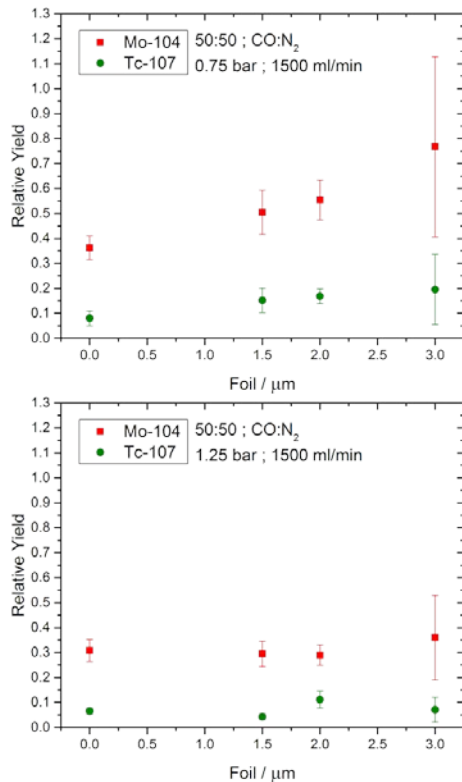
Fig. 2: Plot of the obtained relative yield (see text) of carbonyl complexes obtained for 50:50 mixtures of CO and N_2 and a gas flow rate of 1500 mL/min, different kinetic energies and two different pressures. Each measurement was repeated three times. The standard deviations, shown as error bars, were obtained by error propagation.

Fig. 3 preliminarily shows the dependency of the relative yield of carbonyl complexes for varied gas mixtures. In this example, mixtures of He and CO were used with different ratios of the two components. The top and bottom panel of the picture show the results where no Al degrader foil was inserted between ^{252}Cf-source and where a 3 µm Al foil was inserted, respectively. In general, higher amounts of CO lead to higher yields. However, with decreasing kinetic energy of the recoiling fission isotopes, the dependency on the CO-amount is reduced as well with the total yield appearing to be higher, despite this diminished CO-dependency. Like in Fig. 2, only data for ^{104}Mo and ^{107}Tc are shown as representatives for group 6 and group 7, respectively. The data for Ru and Rh are available but not shown here for the sake of clarity.

It is not entirely clear yet what causes this observation but it is assumed that it might be related to overall transport efficiency phenomena (such as decomposition of initially formed carbonyl) and to the varying degree of implantation losses into the walls of the reaction chamber. Extensive simulations using TRIM [3] and ANSYS® are envisaged to obtain further insights into the stopping and gas dynamical transport processes inside the new setup.
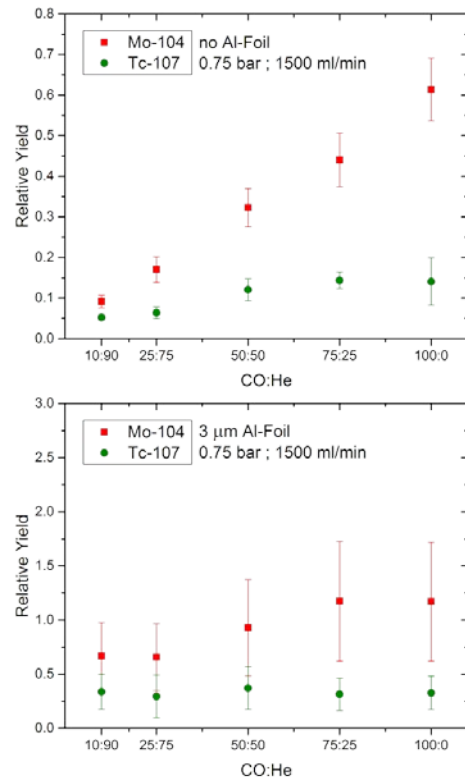
Fig. 3: Plot of the obtained relative yield (see text) of carbonyl complexes obtained for various mixtures of CO and He, whereby the ration between the two components was varied. Two different Al-foil thicknesses are shown, corresponding to two different kinetic energy distributions. The gas flow was set to 1500 ml/min and the pressure to 0.75 bar during the entire measurement series.

In conclusion, we managed to construct a new experimental setup for investigating the formation of metal-carbonyl complexes formed by short lived isotopes under single-atom chemistry conditions. The system was used to investigate the influence of various parameters on the formation of these compounds. However, the evaluation and interpretation of the data obtained is still challenging. By using simulations and supporting measurements, we hope to gain further understanding to finally get insight into the metal-carbonyl formation and transport process. From an experimental point of view, the setup shown in Fig. 1 will be further modified in the near future to allow the investigation of impurity effects in the carrier gases as well.

Acknowledgement

[1] J. Even et al., *Science* **345**, 1491 (2014).

[2] Y. Wittwer, Ann Rep. Lab. of Radiochem., Univ. Bern & PSI, p. 5 (2016).

[3] J. F. Ziegler et al., *Nuclear Instruments and Methods in Physics Research B* **268**, 1818 (2010).

PREPARATORY EXPERIMENTS FOR THE CHEMICAL INVESTIGATION OF NIHONIUM MONOHYDROXIDE

P. Steinegger, N. V. Aksenov, Y. V. Albin, G. A. Bozhikov, V. I. Chepigin, I. Chuprakov, S. N. Dmitriev,
N. S. Gustova, A. Sh. Madumarov, O. N. Malyshev, Y. A. Popov, A. V. Sabelnikov, A. I. Svirikhin,
M. G. Voronyuk, A. V. Yeremin (FLNR, JINR), R. Eichler, D.P. Herrmann, P. Ionescu, B. Kraus,
D. Piguet (Univ. Bern & PSI), B. Gall, Z. Asfari (Univ. de Strasbourg)

During the past few years, gas-phase chemical investigations of Superheavy Elements (SHEs) have been mainly focused on the relatively volatile elements copernicium (Cn, $Z = 112$) and flerovium (Fl, $Z = 114$). Despite the still on-going efforts with respect to the chemical characterization of these two elements, nihonium (Nh, $Z = 113$) increasingly attracts the attention of the community. Thus far, only two investigations targeted the chemistry of this element [1,2].

In a very first approach, without physical pre-separation, a chemical species *with a high volatility, a weak interaction with inert surfaces and an enhanced reactivity towards gold surfaces* was observed [1]. To clarify the chemical speciation of the transported nihonium species, the same experiment was repeated behind the Dubna Gas-Filled Separator [2]. Exclusively inert surfaces between the recoil transfer chamber (RTC) and the detector (i.e., Teflon) assumingly preserved nihonium in its elemental state. From an expected number of approximately five nihonium-related events, none was observed [2]. This none-observation was explained by a higher than expected adsorption interaction of elemental Nh on Teflon surfaces. Furthermore, it was concluded that indeed NhOH was the most likely species being transported during the first attempts [1]. The production of NhOH can be readily explained by the interaction of Nh with quartz surfaces: In accordance with observations made for the lighter homolog thallium, the mere presence of a quartz surface may likewise promote the formation of the monohydroxide form for the heaviest member of group 13 of the periodic table of elements [3].
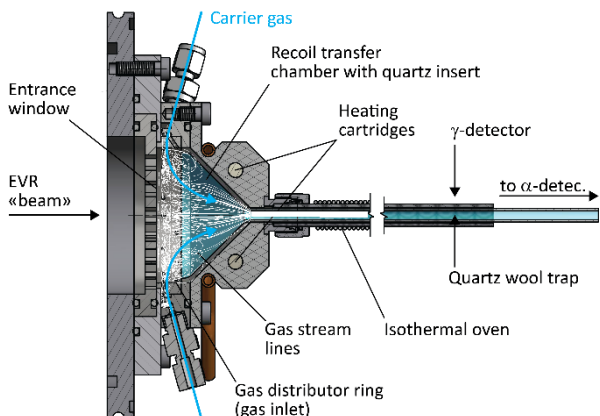
Fig. 1: The experimental setup with the conical recoil transfer chamber and the adjacent isothermal chromatography unit; the white lines indicate the simulated gas flow pattern, resulting in a minimum flushing time of < 1 s. Both possible detection

techniques are indicated.

After these initial experiments, the next logical step to be taken is the unambiguous identification of NhOH. For this reason, a new experiment has been developed, aiming at the fast chemical separation and identification of the investigated species.
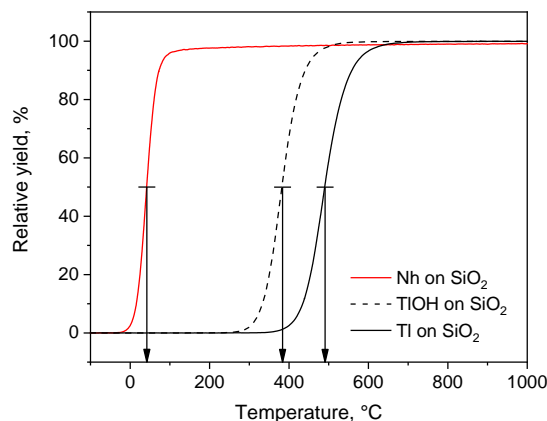
Fig. 2: Monte-Carlo simulations, using the microscopic kinetic model at zero surface coverage [4], for Nh (red line, $-\Delta H_{ads}^{SiO_2}(Nh) = 57.8$ kJ/mol), TlOH (black dashed line, $-\Delta H_{ads}^{SiO_2}(TlOH) = 134 \pm 5$ kJ/mol), and Tl (black line, $-\Delta H_{ads}^{SiO_2}(Tl) = 158.3 \pm 3$ kJ/mol) on quartz and under consideration of all experimental parameters; the arrows indicate the temperature at a relative yield of 50%.

Before targeting the transactinide element once again, online investigations with the lighter homolog thallium have been envisaged. These are essential to clarify the prospects of another SHE experiment, particularly with respect to the involved reaction kinetics. The formation and adsorption behavior of TlOH on gold and quartz was thoroughly studied offline using ^{200}Tl ($t_{1/2} = 26.1$ h) [3]. The longevity of the radioisotope allowed little to be revealed on the time needed for the formation of the chemical compound. Thus, the herein presented online experiments set out to complete and reproduce these results, this time using short-lived ^{184}Tl ($t_{1/2} = 10.1$ s), produced in the nuclear fusion-evaporation reaction ^{141}Pr(^{46}Ti, 3n). The primary ^{46}Ti-ion beam energy of 251 MeV was reduced to 203 MeV ($I_{beam} \leq 2.8$ µA) at the entrance of the target material by means of Ti-degrader foils and the target backing (total thickness: 6.5 µm). The designed setup (see Fig. 1) was optimized to fit the image size in the focal plane of the velocity filter SHELS [5]. The pre-separated reaction products entered the recoil transfer chamber through a thin aluminized Mylar

vacuum window (4.5 μm; $p_{separator} \approx 10^{-7}$ mbar → $p_{RTC} \approx 1000$ mbar) before being stopped in the adjacent RTC (equipped with a quartz insert). The thermalized reaction products were then rapidly flushed into the quartz column of the isothermal chromatography section by the concentrically entering carrier gas (four inlets, Ar/O_2 with H_2O [dew point < 20°C] admixture). The emerging species at the exit of the chromatography column were then either deposited due to the subsequent steep temperature gradient after the oven or retained with the help of quartz or charcoal traps. The deposition / trapping position after the chromatography oven was monitored by γ-spectroscopy for the radionuclide identification (see Fig. 1). Later experiments with NhOH may be conducted at considerably lower isothermal temperatures due to its lower adsorption enthalpy (see Fig. 2). This allows for the required application of event-by-event α-spectrometry and SF-detection for the identification of SHEs (see Fig. 1).
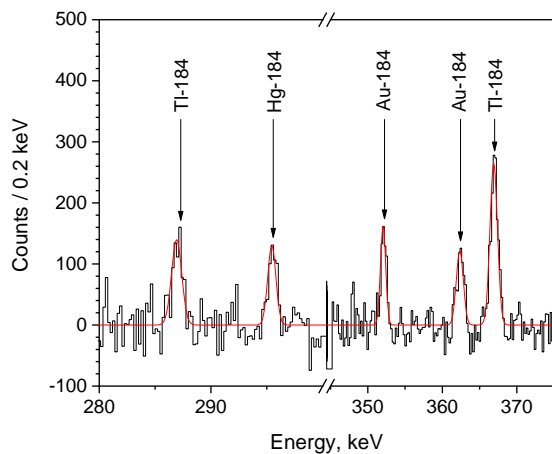
Fig. 3: Excerpt of a background subtracted γ-spectrum (black line) and the corresponding fit (red line), recorded during the collection for a direct catch measurement ($t_{live} = 3600$ s); the two main γ-lines of ^{184}Tl are clearly visible.

Direct catch measurements (see Fig. 3, i.e., the online monitoring during collection) behind the vacuum window helped to establish the injected amount of ^{184}Tl into the RTC by means of its long-lived daughter ^{184}Ir ($t_{1/2} = 3.0$ h). For this purpose, a full consideration of radioactive equilibration during the collection and after the end of bombardment was included together with the respective decay characteristics. Furthermore, side reactions populating the same isobar below ^{184}Tl were taken into account, namely the 1p2n- (^{184}Hg), as well as the 2p1n-reaction (^{184}Au) [6]. At constant production conditions, this result in approx. 70 atoms/s ($I_{beam} \approx 1.7$ μA), being injected into the RTC. These results are in agreement with theoretical expectations.

Despite the applied high temperatures of $T_{RTC} = 550$°C and $T_{ISO} = 700$°C, the employment of various deposition/trapping techniques behind the chromatography column and offering optimum conditions for the formation of TlOH (see [3] for more

details), it has not yet been possible to reproduce previous findings [3].

However, a thallium species with an unexpectedly high volatility was able to overcome the chemical separation stage at room temperature (see Fig. 4). The yield of this species in the charcoal trap amounted to about 20% of the direct catch measurements. Aerosol-bound transport could not be ruled out completely but seems unlikely as this volatile species was even observed at room temperature in a pure argon carrier gas. Thus, two different chemical species of thallium were formed in the RTC: the rather volatile one as well as a species with a relatively high adsorption interaction on quartz, corresponding to a loss of ≈ 80%.
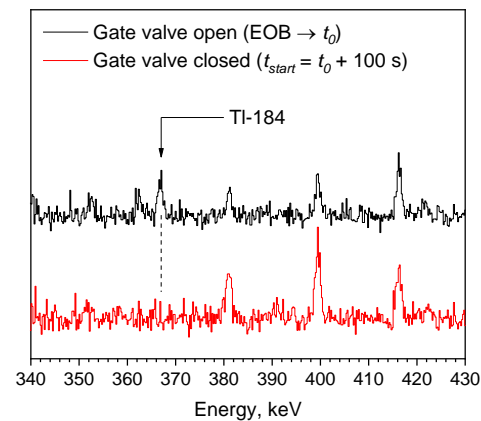
Fig. 4: Verification measurement of ^{184}Tl retained in the charcoal trap (spectra offset for convenience); gate valve open (top, black: $t_{live} = 913$ s) and another measurement started 100 s after the gate valve was closed (bottom, red: $t_{live} = 900$ s).

The discrepancies between the herein presented results and the ones gathered in [3] might be attributed to the initial state of thallium at the beginning of the respective experiments: Whereas in [3] thallium was released at high temperatures form an Au-matrix and passed over a Ta-foil (i.e., ensuring elemental state of Tl), the current studies started with a highly ionized ^{184}Tl^{x+}-species entering the RTC.

Follow-up studies are in preparation and will target the identification of the produced Tl species and the optimization of their yields after the chemical separation.

[1] S. N. Dmitriev et al., Mendeleev Commun. **24**, 5 (2014).
[2] N. V. Aksenov, P. Steinegger et al., Eur. Phys. J. A **53**, 158 (2017).
[3] A. Serov et al., Radiochim. Acta **101**, 7 (2013).
[4] I. Zvara, *The Inorganic Radiochemistry of Heavy Elements*, Springer Netherlands 1st ed. (2008).
[5] A. G. Popeko, A. V. Yeremin et al., Nucl. Instrum. Methods Phys. Res. B **376** (2016).
[6] A. V. Karpov et al., Nucl. Instrum. Methods Phys. Res. A **859** (2017).

SUBLIMATION BEHAVIOUR OF BINARY HEAVY METAL IODIDES IN INERT ATMOSPHERES IN 316L STAINLESS STEEL GRADIENT TUBES

E. Karlsson (Univ. Bern & PSI), J. Neuhausen, A. Vögele (PSI), C. W. Schneider (PSI/LMX),
R. Eichler (Univ. Bern & PSI), A. Türler (Univ. Bern)

Previously, experiments have been performed on the adsorption behaviour of iodine evaporated from lead-bismuth eutectic (LBE) [1]. These data are however not very useful if it is not possible to determine the iodine species evaporated. The purpose of this work is to support speciation by studying the evaporation and deposition behaviour of well-defined Pb- and Bi-iodides. This information can then aid in determining what species are present in the experiments where the sample is an LBE-matrix doped with iodine-nuclides. The sublimation data extracted from the experiments such as sublimation temperatures and potential speciation information is also of great use to determine release behaviour in accidents in LBE cooled reactors.

The experiments were conducted in two different gradient tube thermochromatography furnaces, one using a closed gas loop along with a starting furnace to initially evaporate the sample. The gas loop featured a Sicapent® moisture absorber, an oxygen getter and a dew point meter (Michell PuraOEM) to monitor the moisture content. Helium was used as the carrier gas for the experiments. For the second tube furnace, no gas loop was used and a water bubbler was added to the gas inlet to saturate the helium with water at room temperature. Temperature gradients were applied from 700 °C down to room temperature. At the end of the gradient furnaces charcoal filters were installed to catch species not deposited at room temperature and to prevent contamination.

Tab. 1: Overview of the different experimental parameters used in this work.

Experiment	$BiI/BiI_3/PbI_2$ in moist helium	BiI/BiI_3 in dry helium
Pressure	Atmospheric	1.2 bar
Flow	25 ml/min	45 ml/min
Time	2 hours	2 hours + 1 hour evaporation time
Sample amount	~50 mg	~50 mg

For the bismuth triiodide (Alfa Aesar, 99.999%) and lead diiodide (Alfa Aesar, 99.9985%) samples the commercial product was used directly whereas the bismuth monoiodide was synthesized following [2].

Stoichiometric amounts of bismuth (Fluka AG, 99.98%) and iodine (Merck, doubly sublimated, min. 99.5%), 1.2080 g and 0.7294 g respectively were placed in a fused silica ampoule which was evacuated to 4×10^{-4} mbar under liquid nitrogen cooling and then sealed. The ampoule was heated to 550 °C at a

rate of 60 °C/min and kept at this temperature over night before being quenched in a water bath. The synthesis was finished by tempering the sample at 283 °C for five days.

This process yielded mainly a metallic grey sintered powder as well as some reflective metallic plate-like crystals. These two products were examined using x-ray diffraction (XRD) from which it could be deduced that the powder was bismuth monoiodide whereas the crystals were bismuth triiodide. In figures 1 and 2 the XRD-patterns of the samples can be seen overlaid with reference XRD-patterns [3]. Note that in the XRD-pattern of BiI_3 the 00l-reflections are strongly enhanced, while most of the other peaks are suppressed due to the layer-structure of the material preferentially producing reflections of the {00l} planes.
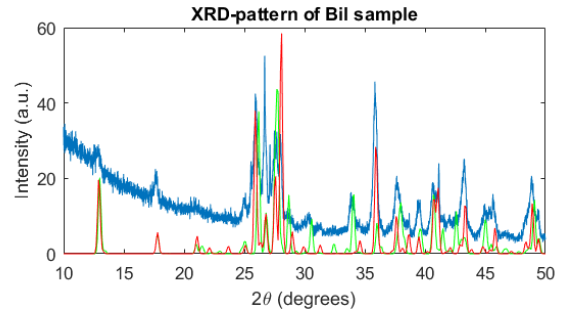
Fig. 1: XRD pattern of metallic grey sintered powder sample (blue) overlaid with reference XRD-pattern of α-BiI (green) and β-BiI (red).
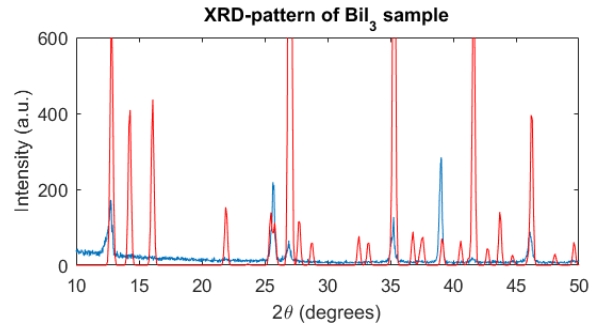
Fig. 2: XRD-pattern of metallic plate like crystals (blue) overlaid with reference XRD-pattern of BiI_3 (red).

An amount of 100 mg of each substance was weighed out and irradiated in the SINQ neutron source (1×10^{13} n/s × cm^2). The irradiation was done in cycles to ensure that the accumulated dose rate of the short-lived ^{128}I (formed by neutron capture) did not exceed the allowed limit. This was possible due to the longer half-life of the desired nuclide (^{126}I, formed by (n, 2n) reaction) allowing it to accumulate with each irradiation cycle.

The bismuth containing samples were each divided into two for their use in separate experiments at either dry or moist condition. For the gas chemical experiments, each sample was placed in a 316L stainless steel boat which was inserted into a column of the same material. For the dry condition experiments a starting furnace was used to evaporate the sample at experiment start, whereas the moist experiments used a pin with a hook to push the sample into the hot zone of the furnace at the beginning of the experiment. The starting furnace was set to 700 °C to evaporate the sample completely. When the materials in the sample are evaporated they travel down the steel column with the gas along the declining temperature gradient until they are deposited on the surface. This deposition point is dependent on the thermodynamic properties of the compound as well as the experimental parameters such as for example gas volume flow and sample amount. After an initial evaporation period of 60 minutes the starting furnace was turned off or the sample pin was retracted, respectively. The experiment continued for an additional two hours in the dry experiments and one hour in case of the moist experiments. The tube furnace was then switched off as well as the gas flow, concluding the experiment. Subsequently, the stainless steel column was measured using an HPGe-detector with a lead collimator in single centimetre steps. This yields a distribution of the activity inside the column.

The deposition patterns measured in the five experiments are depicted in Fig. 1.

In case of the BiI_3-experiments, ^{126}I and ^{206}Bi were detected, while in the BiI-experiments additional ^{203}Pb was found, obviously resulting from n,xn-reactions of a Pb-impurity in the bismuth used for BiI-preparation. In the PbI_2-experiment both ^{126}I and ^{203}Pb were found.

Naturally, the most likely candidates for the deposited compounds are the starting materials themselves, but in the experiments under moist conditions also hydroxides, hydroxyiodides, oxides and and oxyiodides may be formed. Since the main peaks of ^{126}I and the respective metals coincide, it can be concluded that in all cases compounds containing both metal and iodine are deposited. It can be seen that in moist conditions the deposition temperature in the experiments with BiI_3 and BiI is very similar. This gives an indication that the same compound is present in both cases. An explanation for this may be a decomposition of the bismuth triiodide [4] or that the monoiodide sample was actually a mixture of the two (this is indicated also by the XRD patterns).

By examining other nuclides involved such as the lead impurities one can also extract valuable speciation information. For example in the monoiodide experiments (Fig 1. b) there are coinciding lead and iodine peak at a temperature which aligns well with the deposition temperature observed in the PbI_2-experiment (Fig 1. c). The charcoal filter was devoid of any iodine in the moist experiments whereas a significant amount was found there at dry conditions. This indicates the presence of a volatile species, possibly molecular iodine. A more thorough interpretation of the results based on an analysis of thermodynamic data will follow.

a)
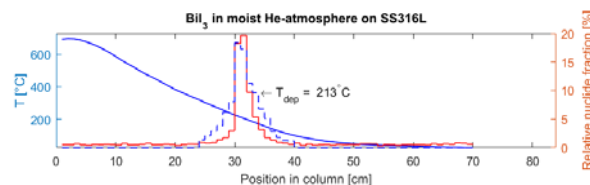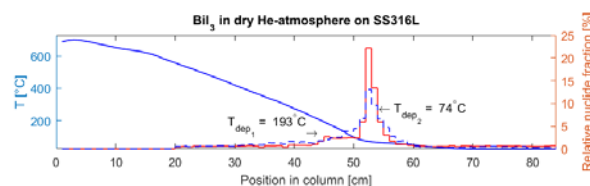
b)
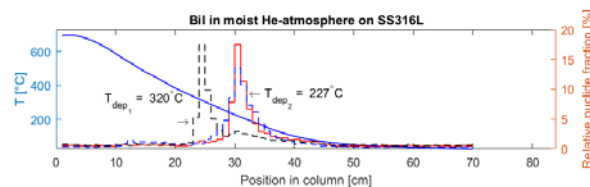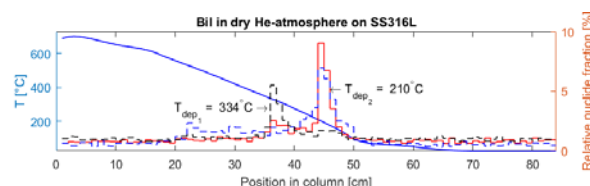
c)
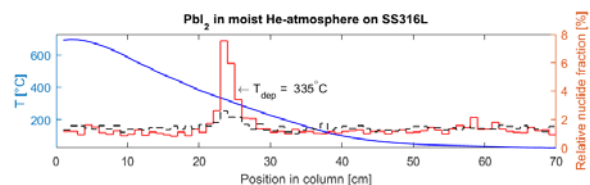
Fig. 3: Histograms of the radionuclide depositions observed in the experiments with SS316L and dry/moist helium with samples consisting of (a) BiI_3 (b) BiI (c) PbI_2 as well as the temperature at the point of deposition. The red solid line depicts the measured distribution of ^{126}I, the dashed lines are ^{206}Bi (blue) and ^{203}Pb (black). The solid blue line is the applied temperature gradient.

[1] E. Karlsson et al., Ann Rep. Lab. of Radiochem., Univ. Bern & PSI, p. 11 (2016).

[2] H. G. v. Schnering et al., Z. anorg. allg. Chem, **438**, 37 (1978).

[3] ICSD - Inorganic Crystal Structure Database http://www2.fiz-karlsruhe.de/icsd_home.html

[4] L.B. Pankratz, Thermodynamic Properties of Halides US-DoI, Bureau of Mines, 89 (1984).

MODELLING OF TRANSPIRATION EXPERIMENTS

R. Dressler, J. Neuhausen (PSI), I.I. Danilov, A. Türler (Univ. Bern & PSI)

The transpiration method [1] has been utilized extensively to determine the release of radionuclides from dilute solutions in liquid lead bismuth eutectic (LBE) and to quantitatively determine their vapour pressure above such solutions to support the safety assessments for future LBE-cooled nuclear reactors [2]. The transpiration setup used in our laboratory as well as the handling and preparation of samples is continuously improved to facilitate studying the influences of trace oxygen and moisture on the evaporation process and to allow studying highly sensitive volatiles such as caesium [3-5]. However, working under well-controlled conditions, e.g. in an inert gas box using sophisticated gas purification systems, makes experimentation much more laborious. Therefore, a more thorough understanding with respect to the conditions under which meaningful results can be acquired becomes necessary, both for planning experiments and for interpreting the results. This requires a rigorous analysis of the propagation of uncertainties. As a first step in this direction, we studied how the statistical uncertainties of activity measurement translate into uncertainties of the final data obtained from transpiration experiments.

In a typical transpiration experiment, the amount of material evaporated from a sample under given conditions (temperature, gas flow, experiment duration, sample mass) is determined. If the carrier gas is saturated with the evaporated species, equilibrium vapour pressures can be determined [1]. For dilute solutions, if the evaporation kinetics obeys a first order law, Henry constants can be determined from the measured fractional release of the substance [6]. In our case, amounts of substances are determined using radioanalytical methods. In a transpiration experiment, we measure the amount of radiotracer present in the original sample before the experiment, the amount remaining in the sample after the experiment and the amount of radiotracer evaporated and deposited in a cold zone downstream of the evaporation zone. The Henry constant can then be determined from the measured activities using the following equations [6]:

$$K_H = -\ln\left(\frac{A_{remaining}}{A_{before}}\right) \cdot m_{LBE} \cdot RT/(M_{LBE}\dot{V}t) \quad (1)$$

$$K_H = -\ln\left(1 - \frac{A_{evap}}{A_{before}}\right) \cdot m_{LBE} \cdot RT/(M_{LBE}\dot{V}t) \quad (2)$$

(K_H: Henry constant, $A_{before/remaining/evap}$: Activity of the sample before and after experiment and activity of evaporated material, respectively, m_{LBE}: mass of LBE, R: universal gas constant, T: temperature at which the volumetric flow is measured, M_{LBE}: molar mass of LBE, $\dot{V}$: volumetric flow, t: experiment duration).

As a consequence, the conditions where meaningful results can be extracted will depend on the precision the ratios A_{evap}/A_{before} and $A_{remaining}/A_{before}$ can be determined. A qualitative assesment reveals that increasing temperature, duration of the experiment and gas flow will tend to let $A_{remaining}/A_{before}$ approach zero, while at the same time the ratio A_{evap}/A_{before} will approach 1. On the other hand, decreasing the same parameters will tend to let $A_{remaining}/A_{before}$ approach 1 while A_{evap}/A_{before} approaches zero. In either case, limits on the precision of the determination of these ratios will be imposed by background rate and counting statisitics.

According to error propagation rules, the uncertainties in the measured activities will translate into uncertainties of the Henry constants derived from eq. (1) and eq. (2) as follows:

$$\Delta K_H = B\sqrt{\left(\frac{\Delta A_{before}}{A_{before}}\right)^2 + \left(\frac{\Delta A_{remaining}}{A_{remaining}}\right)^2} \quad (3)$$

and

$$\Delta K_H = B\frac{A_{evap}}{A_{before}-A_{evap}}\sqrt{\left(\frac{\Delta A_{before}}{A_{before}}\right)^2 + \left(\frac{\Delta A_{evap}}{A_{evap}}\right)^2} \quad (4)$$

with $B = m_{LBE} \cdot RT/(M_{LBE}\dot{V}t)$.

To evaluate the influence of the statistical uncertainties of the quantities A_{before}, $A_{remaining}$ and A_{evap} on the Henry constants calculated using eq. (1) and eq. (2) as a function of measurement parameters such as starting activity, detector efficiency, background rate and counting time as well as the remaining experiment parameters given above, we assess the number of counts obtained from each measurement. Due to the statistical nature of the decay process, the gross counts produced by a given activity (A_{before}, $A_{remaining}$, A_{evap}) can be modelled using a Poisson distribution. The net counts can be derived by background substraction from the corresponding gross counts.

$$N_n = N_g - t_c \cdot br \quad (5)$$

with the associated statistical uncertainty

$$\Delta N_n = \sigma(Nn) \cong \sqrt{N_g + t_c \cdot br}$$

$$(6)$$

The activities are then calculated according to

$$A = N_n/eff/t_c \quad (7)$$

(N_g: gross counts, N_n: Net counts, t_c: counting time, A: activity, *eff*: efficiency, *br*: background rate).

A key point here is the influence of the background term, which is independent from the other measuring parameters and causes an increase of the uncertainty of the net counts. In cases where $A_{remaining}$ or A_{evap} approach zero, the signal to background ratio becomes the key factor. In the limiting cases where $A_{remaining}$ or A_{evap} are almost equal to A_{before} the evaluation of K_H can be unfeasible because the net counts of $A_{remaining}$ or A_{evap} can exceed those of A_{before} due to fluctuations.

We can model series of transpiration experiments by calculating Henry constant values based on the net counts produced from A_{before}, $A_{remaining}$ and A_{evap}, respectively, determined using eq. (7). For simplicity, we assume the same efficincy, counting time and background rate for all measurements. $A_{remaining}$ and A_{evap} are obtained from A_{before} using a model function for the temperature function of the Henry constant based on an Antoine-type relation:

$$\log(K_H) = \alpha + \frac{\beta}{T} \qquad (8)$$

Fig. 1 shows the results of such model calculations obtained using the input parameters $t_c = 3600$ s, $A_{before} = 5$ kBq, $eff = 0.04$, $br = 0.866$ s^{-1}, $m_{LBE} = 0.6$ g, $\dot{V} = 100$ ml/min and $t = 7200$ s. The results for K_H-determination from $A_{remaining}$ and A_{evap} are shown as blue and red dots, respectively. As parameters for the model temperature function of the Henry constant, depicted as green line, we chose values of $\alpha = 12.18$ and $\beta = -6994.3$ K, derived from the nearly linear low temperature results on iodine evaporation from LBE presented in [5]. All data points measured in these experiments are shown as green diamonds. The parameters for all experiments except for the one at the lowest temperature were similar to those used for the simulations. To measure the data point at the lowest temperature, a significantly longer experiment time of $t = 240000$ s was used.
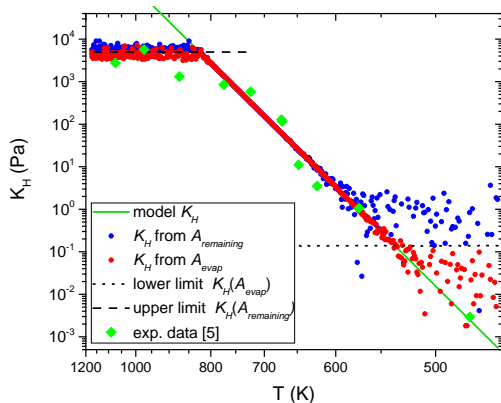
Fig. 1: Comparison of modelled Henry constant data and experimental data obtained from transpiration experiments (see text for detailed explanations).

The modelled values agree well with the input temperature function in the intermediate temperature range. When going to higher or lower temperatures, keeping the other parameters constant, the simulated K_H-values start to deviate from linear behaviour, showing larger scatter, particularly at low temperatures. The simulations also show nicely that – as expected – determining K_H-data close to the lower detection limit is advantageously done based on eq. (2), i.e. by evaluation of A_{evap}, while using eq. (1) allows for a slightly higher upper limit compared to eq. (2). Detection limits for these two cases, corresponding to A_{evap} or $A_{remaining}$ approaching zero, respectively, may be calculated based on 3 times the standard deviation of the background counts. These are indicated as black dashed and dotted lines in Fig. 1.

The results of modelling calculations respond in a reasonable way to the variation of the parameters. For

example, increasing the total number of net counts (i.e. raising the starting activity, the detector efficiency or the counting time) or decreasing the background count rate leads to an extension of the temperature range in which reliable results can be obtained. This range can be extended to lower temperatures or K_H values e.g. by increasing experiment duration and/or flow rate, respectively. Naturally, the variation of these experimental parameters is constrained by practical considerations such as limits of allowance and half-life of the studied nuclide, and the flow rate is limited to the range where saturation of the carrier gas with the volatile species is achieved.

While these qualitative correlations are intuitively clear from analysing eq. (1) and eq. (2), the model implemented here allows quantitative assessments that make the proper choice of experimental parameters straight forward, once a reasonable guess for the temperature function of the Henry constant becomes available. For an unknown system, such an estimate may be derived from thermodynamic data of analogous systems, or by experiments. The model also allows assessing the validity of the obtained data. Comparing experimental data with the results of model calculations at the high temperature region on the left hand side of Fig. 1 indicates that at least the three data points at the highest temperatures are outside the range where valid data can be obtained. The data point for the lowest temperature is clearly below the limit of determination for the set of parameters used in this particular simulation. However, it was obtained using much higher starting activity, experiment duration and counting time. A simulation using the proper parameters for this particular experiment (not shown) indicates that it is a valid data point as far as uncertainties resulting from counting statistics are concerned.

So far, only statistical uncertainties of the activity determination are incorporated in the model. Other sources of uncertainties will be included in the model in due course.

_____

[1] O. Kubaschewski et al., Metallurgical thermochemistry. Pergamon Press, 1979.
[2] Handbook on Lead-bismuth Eutectic Alloy and Lead Properties, OECD-NEA, 2015.
[3] I. I. Danilov et al., Ann Rep. Lab. of Radiochem., Univ. Bern & PSI, p. 15 (2016).
[4] I. I. Danilov et al., this report, p. 18.
[5] I. I. Danilov et al., this report, p. 20.
[6] B. Gonzalez Prieto et al., J. Nucl. Mater **450**, 299 (2014).

VOLATILIZATION OF [134]Cs FROM LEAD BISMUTH LIQUID METAL SOLUTIONS STUDIED BY THE TRANSPIRATION METHOD

I.I. Danilov (Univ. Bern & PSI), J. Neuhausen, A. Vögele, R. Eichler (PSI), A. Türler (Univ. Bern)

Introduction

The subject of this work are radiochemical investigations required for licensing of the MYRRHA reactor conducted within the MYRTE-project as part of the EU-Programm for Research and Innovation "Horizon 2020" [1]. In particular, it deals with studying the release of radionuclides from lead-bismuth eutectic (LBE) in liquid metal cooled nuclear reactors. Here, we describe the development and optimization of the experimental equipment used for volatilization studies, through which it became possible to obtain reliable experimental data. Various series of experiments have been performed using the optimized setup, using caesium, iodine, and polonium tracers. In this report, we summarize the methodological development and show results on caesium evaporation from LBE. Results of experiments on iodine and polonium evaporation will be presented in a separate report [2]. The extracted data for [134]Cs evaporation from LBE will be presented in comparison with existing literature data. The conclusions will summarize the work performed and give an outlook on prospects.

Transpiration method

The transpiration is a well-established method for the measurement of the vapour pressure of pure elements or volatile components of multi-phase alloys [3]. A stable flow of inert gas is led over the substance at a certain rate and at a constant temperature. The volatile components of the substance (in our case the elements Cs, I, and Po or their compounds) are transported by the carrier gas at a rate that depends on their partial pressures and on the velocity of the gas. The amount of (Cs/I/Po)-vapor that condenses or adsorbs in the colder part of the system is determined using the radiotracers [134]Cs / [131]I / [210]Po. By relating the amount of evaporated material to that originally present, Henry constants for the evaporation equilibrium can be determined [5].

Experimental

The preparation procedure for Cs-containing LBE-samples was already described in an earlier report [4]. Therefore, we focus here on a detailed description of the transpiration experiments. The experimental setup used consists of a gas loop in which the evaporation tube is integrated (Fig. 1). The evaporation tube, where the sample is placed and heated, is located inside an inert gas glovebox to facilitate handling of air-sensitive samples such as the Cs-doped LBE studied here. The loop configuration was chosen to achieve the lowest possible concentrations of impurities such as moisture and oxygen. The gas purification system of

the loop is located outside of the glove box. To carry out the transpiration experiment, several sequential tasks have to be performed. To get rid of excess moisture, it is necessary to outgas the quartz tube in which the tracers evaporate and condense under vacuum conditions. The vessel and the quartz fleece that protect the vessel from contact with the radioactive sample are outgassed simultaneously. After the system has cooled down, it is briefly opened to place the sample in the evaporation vessel and position the thermocouple (K-type: up to 1350 °C) next to it. In case of the present study, LBE samples containing a known amount of Cs produced according to [4] were used. The amount of Cs in the samples is determined by measuring the activity of [134]Cs produced by neutron activation in SINQ. After sample insertion, the system is evacuated by a turbomolecular pump. In this way, the tightness of the system is checked, which is necessary to conduct the experiment at a more or less constant pressure and without ingress of oxygen and moisture. Typical vacuum levels reached were 1×10^{-5} – 1×10^{-7} mbar. The system is then filled with carrier gas (helium, hydrogen, nitrogen, etc.) up to 0.5 bars above atmospheric pressure and the circulation pump is started which drives the gas through the circuit. The circuit is self-cleaning, since it contains two Sicapent® drying cartridges as well as a Ta-getter furnace and dual combined oxysorb cartridges that can be alternatively operated to remove traces of oxygen. Moreover, a filter with activated carbon and a mechanical filter of 0.5 microns are sequentially integrated into the circuit in order to protect the pump from radioactive contaminations and from mechanical damage by particles, respectively. Two Sierra mass flow controllers are incorporated into the loop that can be used to adjust the flow rate of the gases in the system in the ranges 10-110 ml/min and 100-1000 ml/min, respectively.
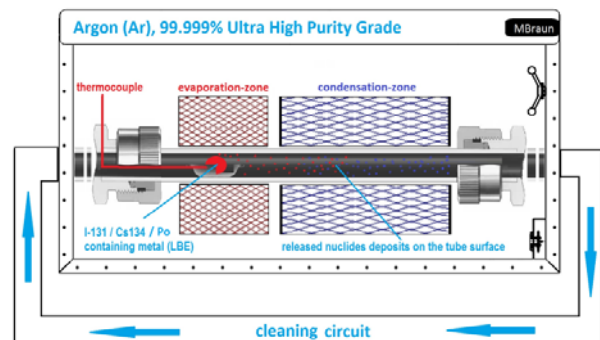

Fig. 1: Schematic outline of the transpiration setup.

To measure the pressure in the line, three sensors are built in, two of them are located at the inlet and outlet of the glove box, respectively, and the third one is

placed directly in front of the reaction tube. The furnace used to heat the sample is mounted on a moveable support. At the start of the experiment, it is heated to the desired temperature while it is positioned downstream of the sample. At the time the evaporation furnace reaches the operating temperature, the furnace is shifted so that the sample is in the centre of the isothermal evaporation zone, which allows to obtain more or less constant temperature (fluctuations at low T: ± 2 °C, at high T: ± 0.3 °C). The temperature of the cold part of the tube equals that of the glovebox atmosphere, regulated at a level of 21-22 °C. At the end of the experiment, the gas flow is stopped by closing valves and the furnace is moved away from the sample to its original position. After the sample has cooled down, all the components of the experiment are placed into plastic bags and measured on a γ-detector. The reaction tube is rinsed 3 times with 4 ml of 7M HNO$_3$ to completely remove the condensed material. The amount of ^{134}Cs in the rinsing solutions is determined by γ-spectrometry.

Data analysis

Henry constants can be evaluated from the activity of the sample before the experiment and the either the activity remaining in the sample or the activity evaporated from the sample using formulas discussed in [5]. These formulas have been used to determine the Henry constant values shown in Fig. 2. The overall uncertainties of the evaluated Henry constant values depend on uncertainties of many parameters of the experiments and measurements, such as those of activity, temperature and flow rate. The uncertainties given in Fig. 2 are preliminary estimates based on the assumption that uncertainties in the γ-spectrometry and the temperature measurement are dominating. These were assumed to be ±10% and ± 15K, respectively. A full treatment of uncertainty propagation will be undertaken in due course. A more thorough assessment of the influences of the counting statistics on the uncertainties of the determined Henry constant values is given in a separate report [5].

Results and discussion

Fig. 2 shows the results of two series of experiments on cesium evaporation from LBE, performed on two different specimens containing Cs in dilute solution in LBE. For both specimens, a linear functional relationship is observed when the logarithms of the Henry constants are plotted vs. the reciprocal temperature. Such a linear behavior is expected when a single species dominates the evaporation process, the carrier gas is saturated with the evaporated species and the samples can be considered ideally dilute. The linearity of the results indicates that the conditions during the experiments were reproducible and that one single evaporation process prevails. Thus, the systematic offset between the results obtained from the two specimens most likely are caused by the properties of the samples themselves. The two samples differed in Cs mole fraction by a factor of three and their masses differed by a factor of two. Causes for the different behavior of the two specimens may be a deviation from ideal dilute behavior induced by the variation of the mole fraction of Cs, or a varying degree of saturation of the carrier gas induced by the variation of the sample mass and size. These effects will be investigated in further experiments by systematically varying parameters such as Cs-concentration, sample mass and carrier gas flow rate. In Fig. 2 both sets of data obtained in the present study are compared with literature data on the evaporation of Cs from LBE [6], Bi [7], and Pb [8] as well as with the vapour pressure of pure caesium [9]. One can state that there is a retention effect of LBE that decreases the vapour pressure of Cs compared to that of the pure metal. The data obtained in our experiments, in particular those determined at higher temperature, are located close to the data determined for the Cs-Bi system [7], which seems to be reasonable considering the preferred formation of caesium-bismuth phases observed in some of the sample preparation experiments [4]. An in depth comparison of all the data is postponed until the causes of the offset observed between the results from the two specimens have been elucidated based on additional experiments.
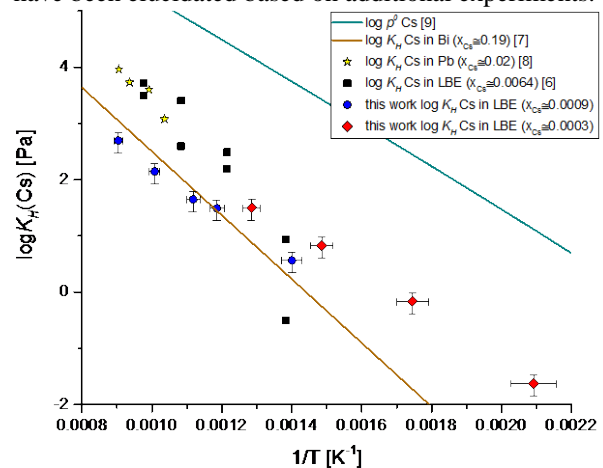
Fig. 2: Results of transpiration experiments using two specimens with different mass and mole fractions of Cs in comparison with literature data [6-9].

[1] https://myrte.sckcen.be/
[2] I.I. Danilov et al., this report, p. 20.
[3] O. Kubaschewski et al., Metallurgical thermochemistry. Pergamon Press, 1979.
[4] I.I. Danilov et al., Ann Rep. Lab. of Radiochem., Univ. Bern & PSI, p. 11 (2016).
[5] R. Dressler et al., this report, p. 16.
[6] S. Ohno et al., Proc. ICONE **15**, 6 (2007).
[7] I. G. Gverdtsiteli at al., Russ. J. Phys. Chem. **58**, 1189 (1984).
[8] L. F. Yamshchikov, Rasplavy. Vx. **2**, 34 (2001).
[9] K. D. Hill et al., Metrologia **33**, 307 (1996).

EVAPORATION OF IODINE AND POLONIUM FROM LIQUID LEAD-BISMUTH EUTECTICUM

I.I. Danilov (Univ. Bern & PSI), J. Neuhausen, A. Vögele (PSI), R. Eichler (Univ. Bern & PSI), E. Müller (PSI/LBR), A. Türler (Univ. Bern)

Introduction

In the continuation of the study of the evaporation of radionuclides from liquid lead bismuth eutectic (LBE) by the transpiration method described in [1], iodine-containing LBE samples were prepared, and the volatilization of iodine was studied. Despite some difficulties with the processing of samples, some interesting results were achieved in the studies with ^{131}I as tracer. Moreover, the evaporation behaviour of [210]Po, which was obtained as a by-product of irradiation of lead-bismuth eutectic, was studied. This report will describe several aspects of sample preparation and characterisation and present preliminary results of the transpiration experiments.

Preparation and irradiation of the samples.

One prerequisite for meaningful transpiration experiments on dilute iodine solutions in LBE is the availability of samples showing a homogeneous distribution of iodine in LBE. Here, we intend to study highly dilute solutions, quantifying iodine by γ-spectrometry measurements of [131]I. This nuclide can be produced in non-carrier added mounts by neutron irradiation of tellurium. Consequently, homogeneous dissolution of Te in LBE is required to obtain suitable samples. This can be achieved either by doping the LBE homogeneously with Te prior to irradiation or by irradiating elemental Te and preparing homogeneous solutions in LBE afterwards. For the 1st route, apart from ^{131}I activation products of Bi and Pb are formed, such as [210]Po, [204]Bi, [206]Bi, [202]Tl and [203]Hg. On one hand, these additional radionuclides are interesting candidates for transpiration studies themselves. On the other hand, they can reduce the sensitivity of the analysis of iodine by increasing the background in γ-spectrometry as discussed in [2]. This additional background can be avoided by following the 2nd preparation route. For both routes, Te was mixed with the appropriate amount of LBE and homogenized in an evacuated quartz ampoule. The conditions for homogenization of the samples and the irradiation procedure were similar to those reported in [3] for Cs-containing LBE.

Sample characterization with SEM

In order to confirm the required homogeneity of the samples, they were examined using a scanning electron microscope (SEM). The results show that slowly cooled samples show segregation especially at the surface, which is evident in both the visual appearance of the surface of the sample and through the occurrence of large grains of PbTe and phase separation in the metallographic section presented in Figure 1. In contrast, a rapidly cooled sample has a smooth surface and most importantly a rather homogeneous distribution of Te within the lead-bismuth matrix, as shown in Figure 2.
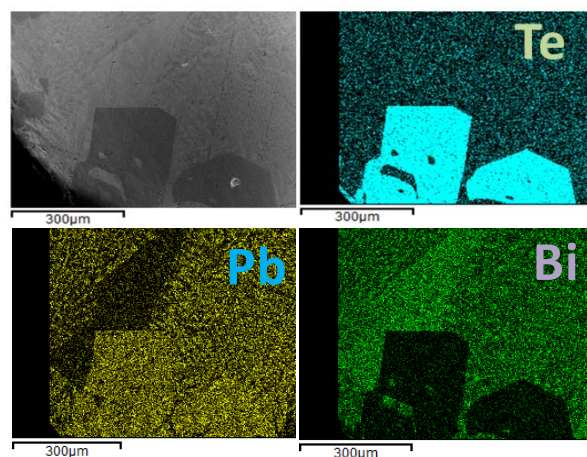
Fig. 1: Polished surface of the sample cross-section of LBE with 10% Te processed at 850 °C and slowly cooled to RT. SEM-Mag.: 149X / Mapping.
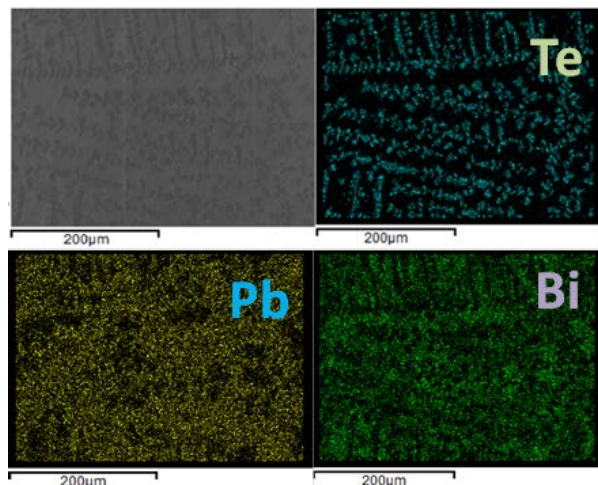
Fig. 2: Polished surface of the sample cross-section of LBE with 10% Te processed at 850 °C and rapidly solidified. SEM-Mag.: 149X / Mapping.

However, also in the rapidly solidified sample a preferred association of Te with Pb can be observed. The effect of this behaviour on the temperature dependent evaporation will be investigated in our further experiments.

Transpiration experiments and analysis

For the transpiration experiments presented in this report, samples prepared by mixing Te and LBE prior to irradiation with a Te-content of 0.5 mass% were used. The samples typically had a mass of 0.4 to 0.9 g and starting activities of 5 to 60 kBq ^{131}I, corresponding to ^{131}I mole fractions in the range of

4×10^{-12} to 4×10^{-11}. The procedure for the experiments was similar to that described in [1] except that the rinsing solutions used to retrieve the evaporated material have been adapted to avoid iodine losses. A sequence of four rinsing steps with 4 ml 4 M KOH, 4 ml H_2O and twice-thrice 4 ml 7 M HNO_3 was used. Additionally to the measurement of the ^{131}I activities by γ-spectrometry, the ^{210}Po-content of aliquots of the rinsing solutions and of the LBE samples has been determined using liquid scintillation counting (LSC).

Results and Discussion

Fig. 3 shows a comparison of Henry constant values for the evaporation of iodine from LBE calculated from data obtained in the present study by the method described in [2], with vapor pressure data of pure Pb and Bi-iodides calculated from tabulated thermochemical data [4]. Three data points obtained from experiments at higher temperatures have been discarded based on the analysis of uncertainties resulting from the counting statistics (see [2] for a detailed analysis). The remaining data show linear behaviour when plotting the logarithm of K_H vs. the reciprocal temperature, indicating a single uniform evaporation process throughout the evaluated temperature range. The values of the Henry constants are clearly lower than the vapor pressure of BiI_3 and fall in between those for the vapour pressures of the more metal-rich iodides PbI_2 and BiI. This is plausible, since the formation of the iodine-rich BiI_3 is highly unlikely in presence of only trace amounts of iodine.
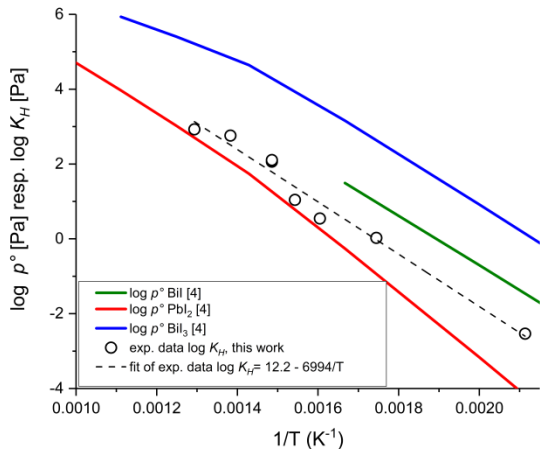
Fig. 3: Comparison of Henry constants of ^{131}I in LBE obtained in this work and the vapor pressures of pure PbI_2, BiI and BiI_3.

Fig. 4 presents a comparison of Henry constant values for the evaporation of ^{210}Po from LBE determined in the present study with literature data [5, 6]. At high temperatures the plot of log K_H vs. 1/T shows linear behaviour with a steep slope. At temperatures below 500 °C (1/T [K] > 0.0013) a decrease of the slope is observed that has been associated with the presence of two different chemical forms of polonium, including a more volatile one that dominates the evaporation behaviour at low temperatures when the LBE contains significant amounts of oxygen and water [6]. Since for the present study the LBE was reduced with Ta-metal at 1000 °C before use and a more sophisticated gas

purification was applied, the lower K_H-values found for T < 500 °C compared to those of [6] can be explained by the lower oxygen/water concentration in the present experiments.
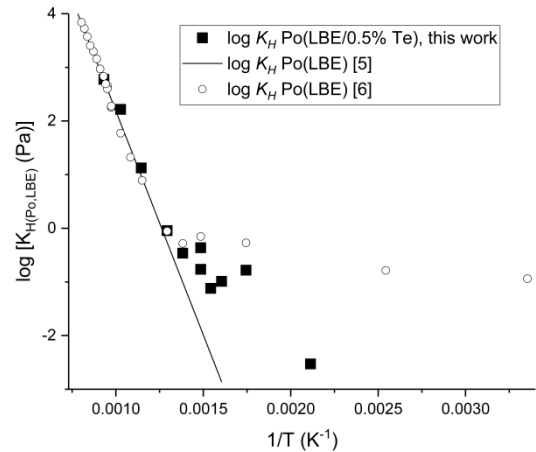
Fig. 4: Henry Constant of accompanying Po-release in comparison with other experimental data [5, 6].

K_H-values obtained for T > 500 °C in the present study seem significantly higher compared to the literature data. A possible explanation would be the formation of PoTe from the tellurium admixture, which should enhance polonium volatilization. This effect should be investigated in a follow-up study.

Conclusion and Outlook

The transpiration apparatus used in our laboratory as well as the associated analytical methods have been further developed to allow a reproducible determination of Henry-constants of trace iodine in dilute solution in LBE. Furthermore, the evaporation of polonium from LBE containing significant amounts of Te has been studied for the first time. Future studies will include a systematic investigation of the influence of the gas flow rate on saturation. A detailed analysis of the γ-spectra measured in this study indicates that additional data on thallium evaporation can be obtained. Otherwise, data on Te-evaporation may be obtained from conventional chemical analysis of the samples.

_____

[1] I. I. Danilov et al., this report, p. 18.
[2] R. Dressler et al., this report, p. 16.
[3] I.I. Danilov et al., Ann Rep. Lab. of Radiochem., Univ. Bern & PSI, p. 11 (2016).
[4] I. Barin, Thermochemical data of pure substances, 3rd ed., VCH, Weinheim, 1995.
[5] S. Ohno et al., J. Nucl. Sci. Tech. **43**, 1359 (2006).
[6] B. Gonzalez Prieto et. al., J. Radioanal. Nucl. Chem. **302**, 195 (2015).

THE NUPECC LONG RANGE PLAN 2017: CONTRIBUTION OF RADIOCHEMISTRY TO THE PERSPECTIVES IN NUCLEAR PHYSICS

D. Schumann (PSI)

The Nuclear Physics European Collaboration Committee – NuPECC - is an Expert Committee of the European Science Foundation. The objective of NuPECC is to "strengthen European Collaboration in nuclear science through the promotion of nuclear physics and its trans-disciplinary use and application in collaborative ventures between research groups within Europe and particularly those from countries linked to the ESF" [1].
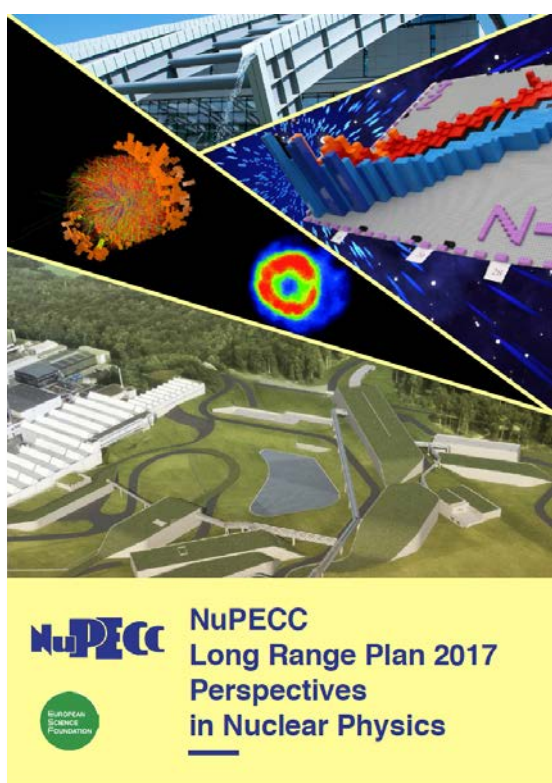
Fig. 1: Cover page of the NUPECC long range plan, released on 19 June, 2017.

Every 6 years, NUPECC evaluates the developments and needs in Nuclear Physics and gives recommendations on the support of European nuclear research and particular projects.

The present long range plan addresses the key issues in basic nuclear physics, hadron physics, properties of strongly interacting matter, nuclear structure and dynamics, nuclear astrophysics, symmetries and fundamental interaction as well as applications and societal benefits. Recommendations are given to complete the construction of FAIR, support world-leading ISOL facilities in Europe, exploitation of the existing and emerging nuclear research facilities, support for LHC and AGATA as well as nuclear theory.

For the first time, the importance of isotope and target production for the performance of numerous nuclear physics experiments is underlined in such an long range plan with the following recommendation:
« We strongly recommend the formation of a target preparation network and the support of target producing research groups to enable successful future experiments. » [2].

With this statement and the hopefully following support, the target preparation community can go ahead to establish an overarching research infrastructure service for target production and develop a tight cooperation between the target laboratories in Europe in order to improve the production technique of well-characterized samples/targets.

PSI plays a leading role in this community of target producers. On page 37, the NUPECC Long Range Plan, emphasizes:

« Activated materials are being processed by the Laboratory of Radiochemistry to extract rare isotopes, e.g. as targets for various nuclear physics experiments world-wide. » [3]

The entire document can be found on the NUPECC homepage :

http://www.nupecc.org/lrp2016/Documents/lrp2017.pdf.

_____

[1]   http://www.nupecc.org
[2]   NUPECC Long Range Plan 2017, p. 167.
[3]   NUPECC Long Range Plan 2017, p. 37.

MASS SEPARATION OF Mn ISOTOPES FOR THE PRODUCTION OF HIGH-PURITY Mn-53 SAMPLES

D. Studer, N. Kneip (Univ. Mainz), R. Dressler, D. Schumann, J. Ulrich (PSI), K. Wendt (Univ. Mainz)

For studies of stellar evolution the isotope ^{53}Mn is of special interest due to its half-life of approximately 4 My [1]. On Earth it is mostly visible via its decay product ^{53}Cr. Measurements of the ^{53}Cr abundance, which is dominated by the decay of ^{53}Mn, can be utilized to date events in the early solar system [2]. However such studies require precise data on the ^{53}Mn half-life as well as neutron capture cross sections in order to obtain information on its formation in stellar events.

For measurements of these nuclear properties, a high purity sample of ^{53}Mn is required. Sample amounts in the order of 10^{19} atoms could be collected within the ERAWAST initiative from activated structure material, such as beam dumps, of the PSI accelerator complex [3][4]. After chemical purification the dominant contaminants are ^{54}Mn ($t_{1/2}$ = 312 d) and ^{55}Mn (stable). While a major part of the former will be decayed until the planned measurement campaign in 2018, the stable contamination of ^{55}Mn/^{53}Mn $\approx$ 100 represents a significant problem for the neutron cross section measurements [5].

A separation of ^{53}Mn from the ^{54}Mn and ^{55}Mn contamination will be carried out at the RISIKO mass separator at Mainz University in early 2018 in order to reach the desired sample purity. The efficiency of the separation process was characterized with stable Mn and is presented below.

Laser resonance ionization of Mn

An efficient method for the production of high-purity ion beams is the resonance ionization mass spectrometry (RIMS), as often used at on-line radioactive ion beam facilities, such as CERN-ISOLDE [6]. Atoms of the desired element are excited stepwise along strong optical atomic transitions into auto-ionizing states or the ionization continuum by pulsed laser radiation. Due to the unique atomic structure of each element this process is element selective while being highly efficient at the same time. On the other hand laser ionization schemes have to be developed individually for each element. So far more than 50 elements are accessible by laser resonance ionization [7]. A combination of resonance ionization with techniques of mass spectrometry allows the production of monoisotopic ion beams.

For the ionization of Mn a new excitation scheme, as shown in Fig. 1, was developed recently at Mainz University. The scheme uses two transitions in the blue wavelength regime at 403 nm and 446 nm and an ionizing transition at 728 nm. In contrast to other Mn ionization schemes [6], no UV radiation is required,

which is advantageous in matters of simplicity of the laser setup and the available laser power.
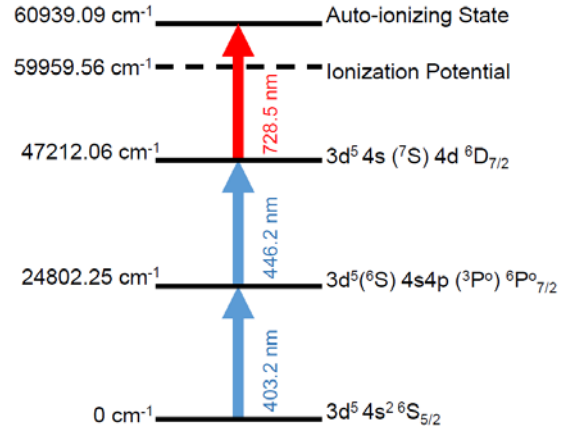
Fig. 1: Laser excitation scheme for Mn. Starting from the atomic ground state Mn atoms are resonantly ionizied via two intermediate bound states into an auto-ionizing state by pulsed laser radiation.

The laser system used for Mn ionization consists of three pulsed Ti:sapphire lasers of the Mainz type [8]. The lasers are operated at a pulse repetition rate of 10 kHz and pulse lengths of typically 50 ns. The output power reaches up to 4 W in the fundamental wavelength range from 680 nm to 960 nm with a spectral linewidth of 5 GHz. Using second, third and fourth harmonic generation, wavelengths from 215 nm to 480 nm can be accessed.

Mass separation at RISIKO

Tests with stable Mn for the characterization of the ion beam production were performed at the RISIKO off-line mass separator at Mainz University. The apparatus is a combination of a hot cavity laser ion source and a magnetic mass separation. Samples are prepared from Mn atomic absorption standard solution and evaporated on a Ta carrier foil, which also serves as reduction agent. The material is introduced into the sample reservoir, a resistively heated Ta capillary, and atomized at approximately 1300 °C. By thermal motion atoms reach the ion source, where they are laser ionized according to the ionization scheme in Fig. 1. Ions are accelerated to 30 keV, pass some ion optics for beam shaping and are mass separated in a 60° dipole magnet with a resolving power of $m/\Delta m \approx$ 800. A post focalization lens behind the separator slits focuses the beam onto the target, so that beam sizes of 0.5 mm FWHM in the focal plane can be reached.

Optimal operating conditions are met at smaller ion currents of < 100 nA, which can be controlled by the

heating current of the sample reservoir, while the atomizer is kept at a high temperature during operation to avoid adsorption of sample material on cold spots.
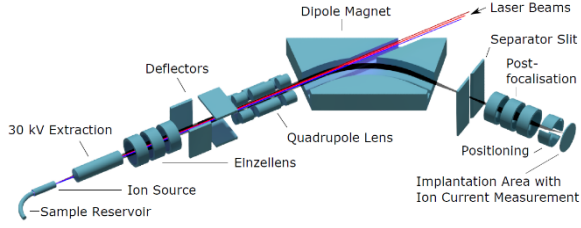
Fig. 2: RISIKO isotope separation and implantation unit. Laser-ionized sample atoms are extracted at 30 kV and separated by their mass to charge ratio in a 60° dipole magnet. Ions of the desired species pass the separator slit and are focused into the target unit.

The efficiency of the Mn implantation is defined as $\epsilon = Q/Ne$, where Q is the total accumulated charge in the target, N the number of sample atoms and e the elemental charge. A total of 10 efficiency measurements were performed with different sample sizes and different maximum ion currents. After each measurement a blank Ta carrier foil was heated in the ion source to quantify Mn traces in the foil and to verify that no sample from the previous measurement is left in the source. Like this an offset for each efficiency measurement can be calculated, reaching from -0.3(1) % to -6(2)% for the samples of 10^{16} and 10^{14} atoms, respectively. An overview of the results is shown in Tab. 1, where the offset is already included in the given efficiencies.

Measurements with samples of 10^{14} atoms were carried out at ion currents of 10 nA for a maximum of 30 minutes before the signal started to decay. With samples of 10^{15} atoms the source could be operated at maximum ion current for a longer time, so that the overall duration is similar to the measurements with 10^{14} atoms, with a small loss in efficiency. At higher currents of some 100 nA, as in the measurements with 10^{16} atoms, space charge effects may impair the ion beam quality and lead to a lower overall transmission through the apparatus. Also the vapour pressure inside the ion source leads to an increased release of atoms from the atomizer to the extraction region. Atoms which are ionized in the extraction field experience a lower acceleration and may appear at lower masses, however these ions are accelerated immediately and arrive very early at the target. This time structure of the ion beam can be utilized to suppress the low-mass tailing by fast switching of a deflector electrode, synchronized to the 10 kHz repetition rate of the laser pulses. Early, low-energy ions are deflected and do not reach to magnet.

For the reasons mentioned above the efficiency in the high-current measurements is significantly reduced, however it should be noted that an increase in the ion current by a factor of 50 leads to a loss in efficiency by a factor of only 3, so that high-current operation is favorable for the implantation of reasonable Mn amounts. In the ^{53}Mn implantation the total ion current has to be considered, because all Mn isotopes are equally laser-ionized. With the isotope ratio of ^{53}Mn/^{55}Mn $\approx 1/100$, an effective ^{53}Mn ion current of 5 nA can be realized.

#	atoms	I_{max} (nA)	duration (h)	ϵ (%)	$\bar{\epsilon}$ (%)
1		10	1.6	26	
2	10^{14}	10	1.7	33	
3		10	2.2	23	23(7)
4		10	1.5	12	
5		20	1.3	15	
6	10^{15}	10	2.3	19	17(2)
7		10	1.9	18	
8		500	2.2	8	
9	10^{16}	500	1	5	7(2)
10		500	1.3	9	

Tab. 1: Overview over the efficiency measurements for different sample sizes of stable Mn. The efficiency is given by the ratio of detected ions to sample atoms.

Conclusion

Resonance ionization mass spectrometry at RISIKO is a suitable method for the purification of ^{53}Mn samples. The strong contamination of ^{55}Mn can be suppressed by a factor of 10^4 to 10^5, while ^{53}Mn can be implanted with ion currents of effectively 5 nA and an efficiency of 7(2) %. In February 2018 four weeks of ^{53}Mn implantation are planned at Mainz University with the aim to produce samples amounts in the order of 10^{17} atoms.

[1] M. Heimann et al., Geochim. Cosmochim. Acta **38**, 217 (1974).
[2] R. Dressler et al., J. Phys. G: Nucl. Part. Phys. **39** (2012).
[3] D. Schumann et al., Nucl. Instrum. Methods Phys. Res. B **264**, 83 (2007).
[4] D. Schumann et al., Radiochim. Acta **97**, 123 (2009).
[5] R. Dressler et al., CERN-INTC-2014-12/ INTC-P-408 (2014).
[6] V. N. Fedoseyev et al., Hyperfine Interact. **127**, 409 (2000).
[7] RILIS Database, http://riliselements.web.cern.ch/riliselements/
[8] S. Rothe at al., J. Phys. Conf. Ser. **312**, 052020 (2011).

TOWARDS NEUTRON CAPTURE CROSS-SECTION MEASUREMENT OF Mn-53

J. Ulrich, R. Dressler, D. Schumann (PSI)

Mn-53 is one of the major radioisotopes produced during supernovae explosions in the universe. Due to its long-enough half-life of ca. 4 Ma it can undergo further processes in astrophysical environments. These reactions considerably influence the cosmic or stellar abundances of the stable isotopes. Sufficiently precise values of the half-life and the capture cross-section of Mn-53 over the whole incident neutron energy range from thermal up to MeV-energies are needed for accurate calculation of the rates of all involved nuclear reactions. These are essential for better description of explosive stages of star evolution, development and testing of numerical star models and understanding cosmic nucleosynthesis and its underlying processes.

Additionally, Mn-53 is produced in small amounts in spallation reactions of high-energy cosmic rays in surface-near rocks on the Earth or in meteorites in space, rendering it's usage as a geological chronometer on a Ma scale promising, but only limitedly possible so far due to the large uncertainty of the Mn-53 half-life value.
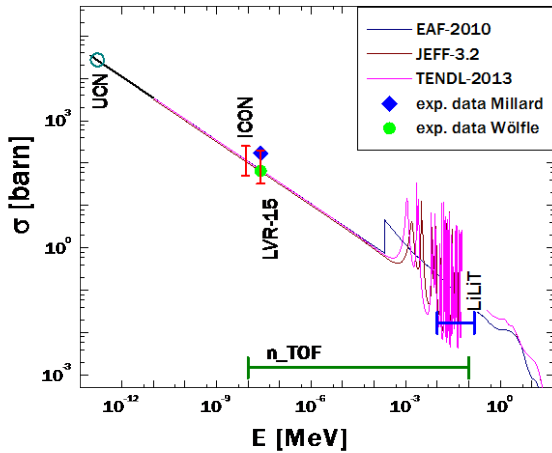
Fig. 1: Neutron capture cross-section of Mn-53 together with marked energy regions of the planned experiments. Experimental data and calculated excitation functions are referenced in the inset.

The neutron capture cross-section of Mn-53 will be measured at different neutron energies covering the spectrum up to the end of the resolved resonance range (RRR), s. Fig. 1. The thermal values of Millard [1] and Wölfle [2], the only existing experimental values up to now, will be re-measured by the activation method at the LVR-15 research reactor at CJV Řež in Czech Republic in first half 2018. Additionally, activation measurements with cold neutrons were performed in fall 2017 at the ICON beamline at PSI. Feasibility evaluation is running for the possibility of activation with ultra-cold neutrons (UCN) at the PSI's UCN source [3]. In 2018, the maxwellian-averaged cross-

section at stellar energies around kT = 30 keV will be measured at LiLiT facility and the RRR will be measured by the time-of-flight method in the Experimental Area 2 (EAR2) of the n_TOF facility at CERN.

A worldwide unique stock of ca. $2 \cdot 10^{19}$ atoms was extracted from irradiated steel and copper material at PSI during the ERAWAST initiative [4]. The copper originated material, roughly one third of the total stock, was used for the current activation measurements due to its more advantageous Mn isotope vector, especially due to the significantly lower Mn-54 content. Before the target preparation, the material was purified as metal chloride solution on DOWEX 1x8 anionic exchange resin to remove the remaining radiochemical impurities Ti-44 and Co-60 (40 kBq and 1 MBq respectively). Baseline separation of all three elements could be achieved by step-wise lowering of the eluent molarity (Fig. 2).
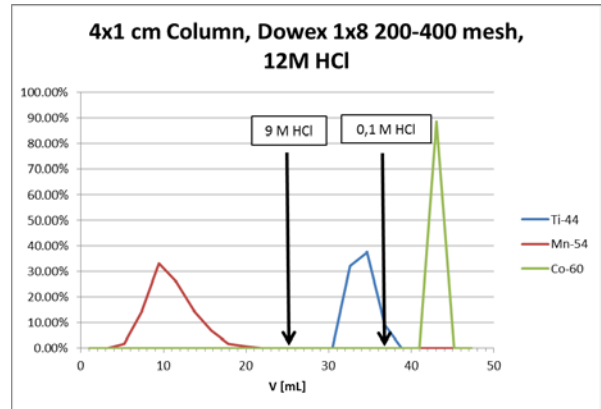
Fig. 2: Radiochromatogram of the Mn-Co-Ti separation on Dowex 1x8 with HCl.

For the activation experiments with cold and thermal neutrons, small amount of natural cobalt chloride was added to a fraction of the purified Mn-53 solution to act as an internal neutron fluence monitor. Three targets were prepared by evaporating known masses of the solution on a quartz wool filter discs (Ø = 0.7 cm), containing ca. $3 \cdot 10^{17}$ atoms Mn-53 per target in form of a chloride salt. To protect the targets from moisture and material loss, the filter discs were sealed by two layers of scotch tape from both sides. Fig. 3 shows one of the finished targets.

ICON is a cold neutron beamline of the PSI's SINQ neutron source with average neutron energy of 8.53 meV and a maximum flux of approx. $7.5 \cdot 10^8$ n/cm²/s/mA, mainly utilized for neutron imaging experiments. The usage of the beamline for activation experiments was approved in parasitic mode of operation only, meaning the activation was done

without any significant disturbance to other experiments running in parallel. An aluminum sample holder was designed and manufactured which lets the most of the beam profile pass unobstructed through the central rectangular opening (s. Fig 4). In the corners of this opening, up to 4 samples of ca. $1\times1cm^2$ can be placed. In our experiments, three positions were occupied with samples and one by a Cividec B6C neutron-sensitive diamond detector for online flux monitoring, with the count rate read out and recorded on PC via LabVIEW.

Fig. 3: Target for the ICON and LVR-15 activation prepared by evaporating Mn/CoCl$_2$ solution to dryness on quartz wool filter and sealing by scotch tape.
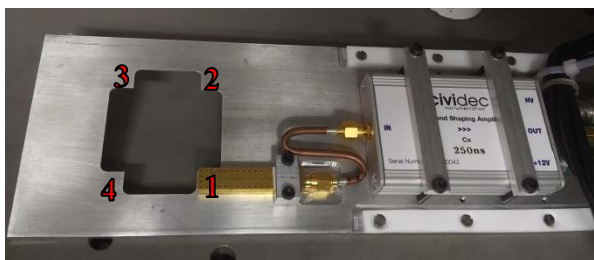
Fig. 4: The setup for activation at ICON with attached neutron detector and preamplifier. The opening enables passing of the majority of the beam. The samples are mounted at the corners of the opening, marked as positions 1-4.

The 2D beam profiles in dependence of different end apertures were determined qualitatively with irradiating neutron sensitive imaging plates (s. Fig. 5) and the impact of the whole setup on the imaging experiments was proved to be negligible. The neutron fluxes at the irradiation positions as a function of the aperture size were calculated by means of gold foil activation and show large differences between the four irradiation positions, especially at small aperture size (s. Tab. 1). Big flux differences between the right (1 and 2) and left (3 and 4) positions, especially with small aperture size, suggest that the beam is not precisely centered towards the geometrical midpoint of the irradiation setup opening, but slightly shifted in horizontal direction instead.
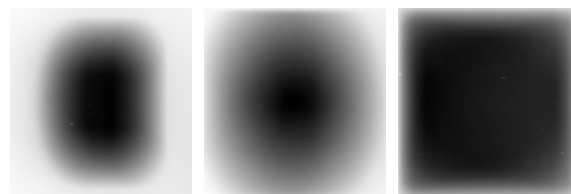
Fig. 5: 2D neutron beam profiles recorded at ICON beam port with 20 mm (left), 40 mm (center) and 80 mm (right) aperture.

Tab. 1: Thermal neutron flux equivalents at irradiation positions 1-4 in dependence of the aperture size.

Apperture	Position	Th. Equiv. Flux [n/cm^2/s]
20 mm	1	$1.33\cdot10^7$
	2	$1.09\cdot10^7$
	3	$8.54\cdot10^7$
	4	$1.01\cdot10^8$
40 mm	1	$1.59\cdot10^8$
	2	$1.52\cdot10^8$
	3	$4.70\cdot10^8$
	4	$5.12\cdot10^8$
80 mm	1	$9.53\cdot10^8$
	2	$8.77\cdot10^8$
	3	$9.36\cdot10^8$
	4	$9.47\cdot10^8$

After an irradiation period of ca. 10 days with the thermal flux equivalent of approx. 10^8 n/cm^2/s, the targets were removed from the beam. First investigations by gamma spectroscopy show well-detectable amounts of the activation product Mn-54 as well as the flux monitor Co-60.

The targets will be transferred to CJV Řež near Prague, Czech Republic in early 2018 and a second irradiation will be performed in the LVR-15 research reactor in order to estimate the maxwellian-averaged thermal capture cross-section and the reactor spectrum resonance integral above the Cd-cutoff.

Both an efficiency calibration of the gamma measurements and the characterization of the original solution in terms of accurate Mn-53 concentration are needed to obtain the final cross-section values. The latter will be performed via MC-ICP-MS at the AHL facility of PSI in 2018.

_____
[1] H. T. Millard Jr., Science **147**, 503 (1965).
[2] R. Wölfle et al., Radiochim. Acta **18**, 207 (1972).
[3] J. Ulrich et al., Ann. Rep. Lab. of Radiochem., Univ. Bern & PSI, p. 27 (2017).
[4] D. Schumann, J. Neuhausen, J. Phys. G. **35**, 014046 (2008).

NEUTRON CAPTURE CROSS-SECTION MEASUREMENTS WITH ULTRA-COLD NEUTRONS (UCN)

J. Ulrich, R. Dressler (PSI), B. Lauss (PSI/LTP)

Ultra-cold neutrons (UCNs) are neutrons with energies below about 300 neV which corresponds to a velocity $v = 7.6$ m/s. At such low energies, the neutron behaviour is best described by means of wave optics similar to visible light and, consequently, UCNs can be totally reflected on material boundaries if their kinetic energy with respect to the surface normal is lower than the surface neutron optical potential (50-250 neV for typical materials). Therefore, UCNs can be stored in 'neutron bottles' and used for various physics experiments, e.g. the measurement of the neutron electric dipole moment (nEDM) or the neutron lifetime.

Neutron fluxes delivered by UCN sources are several orders of magnitude lower than typical neutron fluxes of thermal or cold neutron sources. But the neutron capture cross-section rises with decreasing neutron energy according to the $1/v$ law, leading to an approximate 300-fold increase at UCN energies with respect to the thermal cross-section value. This compensates partially the low flux and makes UCNs interesting for capture cross-section measurements of various isotopes, and, in addition, allows the checking of the validity of the $1/v$ law at ultra low energies.

Previous UCN capture cross-section measurements were made mostly by means of foil transmission measurements [1]. Experiments performed at the PSI UCN source using a plastic collimator and measuring thin metal foil activation in 2016 yielded unsatisfying reproducibility and inconsistent results both between chemically identical samples and between different materials. These issues were attributed to hardly controllable surface effects like roughness, contamination or oxidization [2], which can usually be neglected during activation experiments with thermal neutrons.

In 2017, the activation of liquid samples was investigated, similar to experiments in [3]. Relative cross-section measurements were performed, i.e. the sample element and a second element as a flux monitor were both put into the same solution and subsequently activated. With this approach, most experimental differences in sample (e.g. sample self-absorption, solution matrix or filling level) and irradiation conditions (e.g. pulse intensity or period) cancel out.

The isotopes Au-197, Br-81, Na-23, La-139 and Sc-45 were chosen for the experimental studies because of advantageous chemical properties of the element, high activation rates in materials with natural isotopic composition and their activation products easily measurable by gamma spectrometry. Due to the high scattering cross-section of natural hydrogen, D_2O and deuterated acids were used for the dissolution. Na and

Br could be solved as crystalline NaBr in pure D_2O. La_2O_3 and Sc_2O_3 were dissolved in diluted and boiling concentrated DNO_3 respectively. Au was oxidized in a 6 : 1 (by volume) DBr and DNO_3 mixture working analogous to classical *aqua regia* but omitting Cl which would act as neutron poison during the irradiation.

A special cuvette was designed and constructed for the experiments (s. Fig. 1). This consists of a metal-reinforced cylindrical plastic body with entrance and exit window made of of 0.5 mm thick silicon wafer plates which pose a very small surface potential of 60 neV, i.e. transmit all but the slowest UCNs. The height of the inner volume is chosen only 2 mm considering the small penetration depth of UCNs, but the cross-sectional area was designed as big as possible ($\varnothing = 6.3$ cm) to maximize the beam interception. The cuvette is filled via a syringe with about 6 mL of the sample solution. The plastic body and the o-ring seals were manufactured from PEEK and Viton respectively to ensure resistance against the highly acidic sample solutions.

Fig. 1: Cuvette for activation of liquid targets with ultra-cold neutrons (outside diameter = 100 mm, total thickness = 13 mm).

After 1-3 days activation at the PSI UCN source, the induced activity was measured with a Canberra BEGe 2825 HPGe detector in a dedicated sample holder with minimal distance between sample and detector endcap. The measurement is especially sensitive to True Coincidence Summing (TCS) because of the close distance and flat shape of the activated sample. Thus, to optimally account for TCS, the same activation products (i.e. Au-198, Br-82, Na-24, La-140 and Sc-46) were produced by neutron activation in the NAA facility at SINQ. They were dissolved under similar conditions like the sample material (but using conventional, non-deuterated chemicals). The solutions were characterized with regard to their specific activity by preparing a point-like source with a known amount of the solution and measuring it in sufficiently large distance (17 cm) for which the detector was calibrated with a certified Eu-152 reference source. The efficiency for the sample

measurements was subsequently determined by filling the characterized solution into the cuvette and measuring it in the same geometry as the real samples. Typical experimental conditions were 24-72 h irradiation period, average thermal flux equivalent of about 2000 n/cm^2/s, 24-48 h gamma measurement time. This leads to deduced activities of 1-10 Bq of the corresponding activation product. The time stamps and relative intensities of the UCN pulses were recorded using a UCN detector mounted on a separate UCN beam line. This enables to correct for missed pulses, shutdowns and the continuous intensity decrease during operation of the UCN source [5].

Tab. 1: Summary of the neutron capture cross-section with ultra-cold neutrons obtained with the liquid target cuvette (preliminary analysis results). The deduced cross-sections were recalculated to the thermal value at 293 K (25.3 meV).

Target	Monitor	Sample	$\sigma_{n,\gamma}$ meas [barn]	$\sigma_{n,\gamma}$ lit.[4] [barn]	rel. diff [%]
La-139	Au-197	1	7.61(17)	9.04(4)	-15.8
		2	7.82(12)		-13.5
		3	8.84(11)		-2.2
		4	8.92(18)		-1.3
		5	8.24(22)		-8.8
Br-81	Na-23	1	2.62(4)	2.36(5)	+11.1
		2	2.67(6)		+13.0
		3	2.70(8)		+14.3
Sc-45	Au-197	1	28.4(5)	27.2(2)	+4.4
		2	25.9(5)		-4.7
		3	20.4(5)		-25.1

Table 1 summarizes the preliminary results. The measured cross-sections match the magnitude of their reference values but scatter within a band of –25 % and +15 %. This spread is significantly larger than the estimated uncertainties, typically in the order of ±2-3 %, indicating unsufficient knowledge about partial effects contributing to the overall uncertainty, which could not be satisfactorily identified yet. Quantification of these uncertainty components and their minimization is crucial for further precise analysis of UCN activation measurements.

The systematic deviation in one direction (undershooting for La-139 or overshooting for Br-81) of the calculated values in all individual measurements might indicate a systematic error, most probably due to the efficiency calibration of the gamma spectrometer. This will be checked in the second half of 2018 when production of short-lived radiotracers by neutron activation will be available at PSI again.

[1]   A. Steyerl, Phys. Lett. **29B**, 33 (1969).
[2]   J. Ulrich et al., Ann Rep. Lab. of Radiochem., Univ. Bern & PSI, p. 27 (2016).
[3]   J. Schroffenegger et al., Phys. Lett. B **752**, 212 (2016).
[4]   S. F. Mughabghab, Atlas of Neutron Resonances, 5. Ed., Elsevier (2006).
[5]   J. Ulrich et al., Ann Rep. Lab. of Radiochem., PSI, p. 29 (2017).

UCN ACTIVATION DATA ANALYSIS

J. Ulrich, R. Dressler (PSI), B. Lauss (PSI/LTP)

Relative neutron capture cross-section measurements were performed by the activation method with ultra-cold neutrons (UCNs) in 2017, using liquid targets (for more experimental details, see [1]). Since the evaluation of these activation data differs substantially from evaluation of activations at usual neutron sources, a short overview of the procedure is given below.

The usual formulation of the activation equation for a radioactive activation product with half-life $t_{1/2}$ and decay constant $\lambda = \frac{\ln 2}{t_{1/2}}$ is:

$$A = N\sigma\phi(1 - \exp(-\lambda t_A)) \exp(-\lambda t_C) (1 - \exp(-\lambda t_M))$$

where A denotes the activity of the activation product, N the number of atoms, σ the activation cross-section and ϕ the neutron flux. The three exponential terms correct for the decay of the activation product during the activation period t_A, the cool-down period t_C and the activity measurement period t_M, respectively.

The decay correction during the measurement was performed by GENIE2000 gamma spectrometry software, giving the decay-corrected activity A' to the the start of the activity measurement.

With $t_A \gg t_{1/2}$, the production and decay rates of the activation product reach equilibrium. Activation under such conditions is disadvantageous with regard to a later cross-section determination, since the dependency of the activity on the irradiation history is lost. Therefore, maximal activation times of twice the half-life of the activation product (corresponding to 75 % saturation) were used.

The number of target atoms is calculated from the weight of the target material m:

$$N = \frac{wm\theta N_A}{M}$$

with w being the mass fraction of the target element in the target compound, M the compound's molar mass, θ the abundance of the target isotope and N_A the Avogadro constant.

The neutron flux at the PSI UCN source's [2] beam lines is time-dependent both in short and long term. The UCNs are produced in discrete pulses when the 590 MeV/2.2 mA proton beam is diverted for up to 8 s to the spallation target of the UCN source. The produced fast neutrons are thermalized in a D_2O moderator, cooled-down in solid D_2 with a temperature of 5 K and extracted towards the beamlines. This results in a time profile of the neutron flux as in Fig. 1, with the highest intensity during the proton pulse. The pulse period T during the activation was typically 5 min. The energy of the UCNs is not well determined but has a low energy cut-off given by the Al beam

window and a high energy cut-off given by the surface potential of neutron guides and storage vessel.

On the scale of days, the UCN intensity continuously decreases due to surface degradation of solid D_2 as a consequence of the heat impact of 11 MJ per proton pulse on target. Sometimes no UCNs are provided because of missed pulses or shutdown periods as can be seen on Fig. 2.
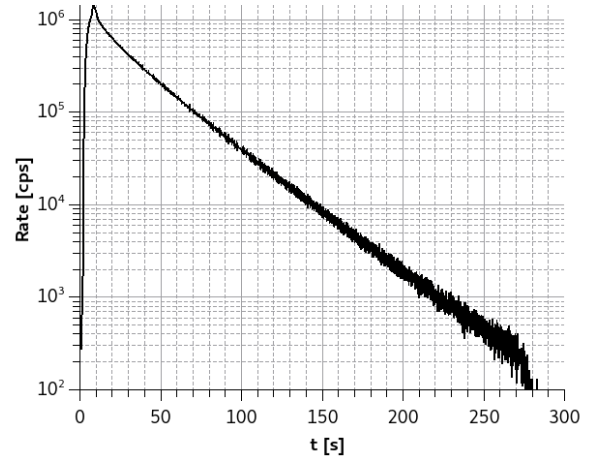
Fig. 1: Time profile of UCN delivery to a beam port after a proton pulse. Pulse period was 300 s.
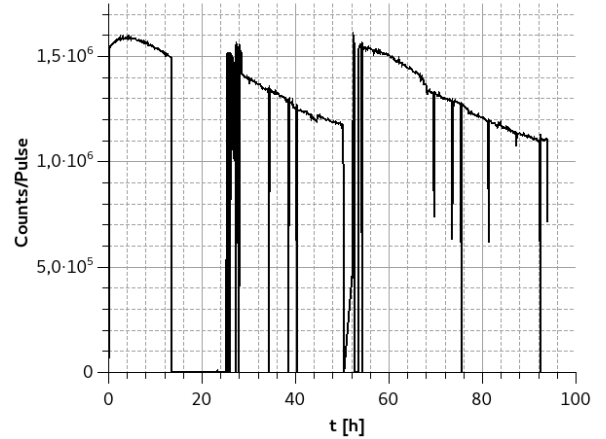
Fig. 2: Example irradiation history of a single UCN activation with multiple missed pulses, a large shutdown around 20 h, continuously dropping UCN intensity and an increase after a "conditioning procedure" which regains the solid D_2 performance, done at approx. 55 h (after ~5100 mC proton charge on target).

The absolute UCN flux value itself couldn't be measured during the irradiation, but a neutron sensitive detector was installed on a second beamline and used for online flux monitoring during the activation period.

The UCN flux ϕ in the activation target is direct proportional to the measured neutron count rate $\dot{Z}$ of the detector by the normalization factor k:

$$\phi = k\dot{Z}$$

The flux dependence within a pulse can be neglected during the data evaluation, because $t_{1/2} \gg T$. Nevertheless, the long-term decrease of the flux needs to be considered, since during some measurements differences by almost a factor of two between the count-rates at the beginning and at the end of the irradiation period were observed.

In the calculations an infinitesimally short activation at the trigger time of each pulse was assumed, with the fluence proportional to the accumulated neutron counts Z during the pulse. The decay-corrected activity produced during a single pulse is therefore:

$$A' = N\sigma kZ\lambda \exp(-\lambda \Delta t)$$

with Δt being the time between the time stamp of the pulse and the start of the activity measurement. The total produced activity can be expressed as the sum over all individual pulses i:

$$A' = N\sigma \lambda k \sum_i Z_i \exp(-\lambda \Delta t_i)$$

The ratio R between the sample (index S) and monitor (index M) cross-section can now be expressed as:

$$R = \frac{\sigma_S}{\sigma_M} = \frac{A'_S}{A'_M} \cdot \frac{N_M \lambda_M \sum_i Z_i \exp(-\lambda_M \Delta t_i)}{N_S \lambda_S \sum_i Z_i \exp(-\lambda_S \Delta t_i)}$$

The flux normalization factor k is identical for both isotopes and therefore cancels out in the equation. Both the sample and the neutron flux monitor material were completely dissolved and these individual solutions were unified before the activation. Therefore, knowledge of the exact absolute number of atoms in the cuvette during the activation is not needed. Instead, it is sufficient to calculate this ratio from the masses of the chemicals used for the preparation of the individual solutions.

The obtained preliminary values of R are summarized in Table 1. For calculation of the reference ratios, thermal cross-section values from [5] were used, since both the cross-section of the sample and the monitor should follow the $1/v$ law. The calculated ratios are roughly in agreement with the reference values, but show much broader scattering than expected from the formal uncertainty propagation, suggesting an underestimation of some uncertainty component or an additional, not yet considered uncertainty.

The half-lives and gamma-ray line intensities were preferably adopted from [3], if no evaluation was available for the given radionuclide, [4] was used. The given uncertainty of the half-life as well as the uncertainties of atomic and molar masses and the isotopic abundances were neglected. The count statistics of neutron detector was very good (at least ~100 000 counts/pulse), allowing discarding of the associated uncertainty, too. The weighing errors in the order of 0.05 mg could be neglected as well, because the typically used masses were ~50 mg for Au and >100 mg for other chemicals. The uncertainty of the activity was dominant for all measurements and full uncertainty propagation was performed within GENIE2000 under consideration of the uncertainties of the peak areas, emission intensities, half-lives and the activities of all radioactive sources used in the chain of the efficiency calibration of the measurements.

Tab. 1: Capture Cross-section ratios calculated from the UCN activation measurements (preliminary results). The literature ratios are calculated from the thermal capture cross-section values from [5].

Target	Monitor	Sample	R meas	R lit.[3]	rel. diff [%]
La-139	Au-197	1	0.0771 (17)	0.0916 (5)	-15.8
		2	0.0792 (12)		-13.5
		3	0.0896 (11)		-2.2
		4	0.0905 (18)		-1.2
		5	0.0836 (22)		-8.7
Br-81	Na-23	1	5.07(6)	4.56(1)	+11.2
		2	5.16(11)		+13.2
		3	5.22(16)		+14.5
Sc-45	Au-197	1	0.288(5)	0.276(2)	+4.3
		2	0.263(5)		-4.7
		3	0.207(5)		-25.0

[1] J. Ulrich et al., Ann Rep. Lab. of Radiochem., Univ. Bern & PSI, p. 27 (2017).
[2] B. Lauss, Phys. Proc. **51**, 98 (2014).
[3] BIPM Monographie 5 (Webversion) (http://www.nucleide.org/DDEP_WG/DDEPdata.htm), Status: 01/12/2017.
[4] NuDat 2.7 (http://www.nndc.bnl.gov), Status: 01/12/2017.
[4] S. F. Mughabghab, Atlas of Neutron Resonances, 5. Ed., Elsevier (2006).

NEUTRON ACTIVATION EXPERIMENTS ON ^{10}Be(n,γ) AT THE TRIGA REACTOR IN MAINZ

M. Weigand, D. Veltum, M. Volknandt, P. Erbacher, S. Fiebiger, M. Fix, K. Göbel, J. Glorius,
T. Heftrich, E. Hrivula, C. Langer, R. Reifarth, S. Schmidt, B. Thomas, C. Wolf (Goethe University),
K. Eberhardt, C. Geppert, N. Wiehl (Univ. Mainz,), S. Heinitz, D. Schumann (PSI),
A. Junghans (HZDR), F. Käppeler (KIT), A. Mengoni (CERN)

The main goal in nuclear astrophysics is the explanation of the origin and the abundances of the elements we observe in the solar system and in the universe. Various processes assigned to different astrophysical scenarios are involved. Their quantitative description requires vast reaction networks consisting of hundreds of different particles and thousands of reactions. Hence, for a successful reproduction of the observed abundances, there is a need for experimental data on the involved reaction rates [1].

Astrophysical aspects on the ^{10}Be(n,γ) reaction

The pattern of the solar abundances of nuclides features a conspicuous minimum in the region of the light elements Li, Be, and B. The main origin of these scarce elements are thought to be spallation reactions on C, N and O in the interstellar and circumstellar matter caused by cosmic gamma rays. It is referred to as interstellar nucleosynthesis [3, 4]. However, it is essential to know the involved neutron capture reaction cross sections in this mass area in order to quantify the contributions of stars to the observed abundances. One of those, which has not been measured so far, is the ^{10}Be(n,γ) cross section. So far, only data from Coulomb breakup ^{11}Be, the time-inverse reaction, are reported. This is an indirect method, which in principle allows the investigation of much shorter half-lives. The ^{10}Be(n,γ) reaction is one of the rare examples, where this approach can be tested [5-8]. **Fig.** depicts the area of the lightest elements in the chart of nuclei along with the reaction of interest (black arrow) and the decay of the product (red arrow).
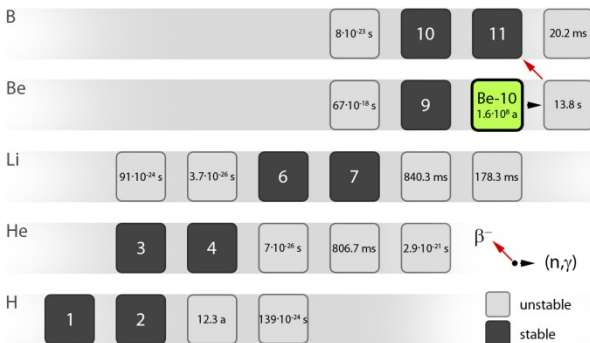
Fig. 1: Chart of the nuclides from hydrogen to boron. Stable isotopes are depicted as dark, unstable isotopes as light grey boxes. A neutron capture on ^{10}Be leads to ^{11}Be, which has a half-life of 13.8 s only and decays to ^{11}B.

In the scope of this article, neutron capture reactions on ^{10}Be have been studied by the means of the activation method [2] at the TRIGA reactor in Mainz, Germany.

The ^{10}Be sample

The BeO sample has been produced at PSI. Its weight was 8.93 mg corresponding to 6.6 10^{19} ^{10}Be atoms in the sample. Originally it was foam-like and after the first activation it was a white small-grained powder (see right).

The activation experiment

The activation was performed at the TRIGA reactor in Mainz. The reactor delivers up to 10^{13} neutrons/cm^2/s in the regular operation mode. However, the pulsed mode allows a thermal fluence of up to 10^{15} neutrons/cm^2/s for a time period of 30 ms. A pneumatic system allows the transfer of the sample into and out of the reactor within seconds.

The sample was irradiated in several cycles [9]. The neutron fluence has been determined using monitors with well-known cross sections. In this case, gold and scandium were used together with the sample in a sandwich configuration [10].

The numbers of produced ^{11}Be particles were identified using γ-ray spectroscopy using two LaBr$_3$ detectors in a head-to-head setup, Fig. 2.
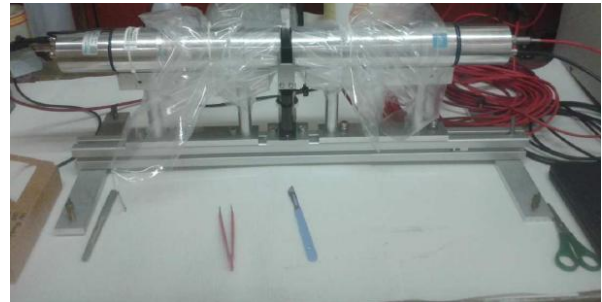
Fig. 2: Two LaBr$_3$ detectors were used to measure the ^{11}Be activity following the neutron irradiation of ^{10}Be.

A typical spectrum is shown in Fig. 3. Using the cadmium differential method, the thermal neutron capture cross section as well the resonance integral could be determined. Preliminary values are

$$\sigma_{th} = 1.25 \text{ mb and } I_{res} = 1.02 \text{ mb}$$

with an uncertainty of about 10%.
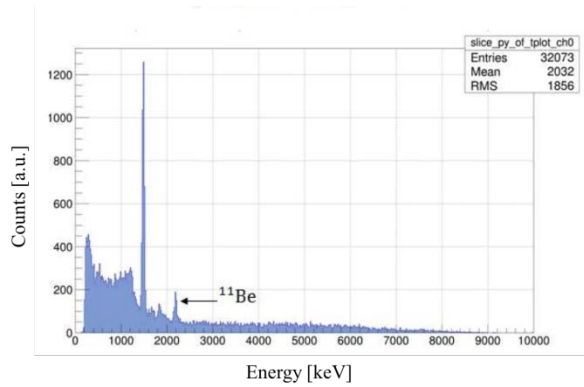
Fig. 3: A typical γ-ray spectrum of the produced [11]Be nuclei for one activation and one detector channel.

The final analysis of the cross sections as well as their astrophysical impact are currently under investigation [11].

_____

[1]   Burbidge, E.M., et al., Rev. Mod. Phys. **29**, 547 (1957).

[2]   Reifarth, R., C. Lederer, and F. Käppeler, J. Phys. G: Nucl. Part. Phys. **41**, 053101 (2014).

[3]   Thomas, D., et al., The Astrophysical Journal **406**, 569 (1993).

[4]   Coc, A., et al., The Astrophysical Journal,. **744**, (2012).

[5]   Reifarth, R., et al., Journal of Physics Conference Series (2016).

[6]   Altstadt, S.G., et al., Nuclear Data Sheets **120**, 197 (2014).

[7]   Fukuda, N., et al., Physical Review C **70** (2004).

[8]   Nakamura, T., et al., Physical Review C **79** (2009).

[9]   Reifarth, R., et al., Physical Review **77,** 015804 (2008).

[10] Heftrich, T., et al., Physical Review C **92**, 5806 (2015).

[11] Weigand, M., et al., Physical Review C **92** (2015).

ELASTIC SCATTERING ^{10}Be+^{4}He TO INVESTIGATE α-CHAIN STATES IN ^{14}C

A. Di Pietro[1], P. Figuera[1], S. Heinitz[2], M. Lattuada[1,3], C. Marchetta[1], S. Marletta[1], D. Torresi[1], D. Schumann[2]
1) INFN, 2) PSI, 3) DFA

Abstract – The elastic scattering excitation function ^{4}He(^{10}Be,α) was measured using a radioactive ^{10}Be beam at the TANDEM accelerator of Laboratori Nazionali del Sud (LNS) in Catania, Italy. The aim was to study α-cluster states in the compound nucleus ^{14}C in order to confirm the recently claimed existence of the α-chain state in that nucleus.

INTRODUCTION

In light nuclei some of their structural properties can be described by assuming a nuclear structure made of a few weakly interacting clusters. In n-rich nuclei, the α−α cluster structure as a core may persist but it is the exchange of neutrons between the α□particle cores, which bounds the system. The existence of a linear chain configuration in excited states of nuclei such as ^{12}C or ^{16}O, has been searched for by many scientist for a long time; however no evidence has been found so far.

Theoretical predictions of linear chain configuration in ^{14}C of α-particles bound together by neutrons that act as electrons in the covalent bonding, was made by Suhara and En'yo [1] with antisymmetrised molecular dynamics (AMD) calculation. Associated to this configuration, a prolate band, that has a linear shape, should exist at a few MeV above the ^{10}Be+α threshold. In order to look for this structure in ^{14}C, three experiments have been performed so far [2-4], where the ^{10}Be+^{4}He elastic scattering excitation function was measured. Controversial results on the possible presence of the inelastic scattering contribution in the detected α-particle spectrum have been reported in [3,4]. This could affect the observation reported in [4] of the rotational band associated to the linear chain configuration in ^{14}C.

In order to shed some light on this issue we decided to use the newly available ^{10}Be radioactive beam at LNS to re-measure the ^{10}Be+^{4}He elastic scattering excitation function with higher precision.

EXPERIMENT

The experiment was performed at LNS using a radioactive ^{10}Be beam produced in batch-mode. The ^{10}Be radioactive material (0.1 mg of ^{10}BeO) was prepared at PSI, and was inserted in the cathode of the TANDEM sputtering source. The beam was accelerated at 47 MeV by the TANDEM accelerator. The target consisted in the CT2000 scattering chamber (2 m diameter) filled with an isotopically pure ^{4}He gas at a pressure of ≈ 650 Torr. The chamber was separated from the high vacuum beam line by a ≈12 μm thick Kapton window. Elastically scattered α-particles were detected and discriminated from other reaction processes using both ΔE-E and Time of Flight

(ToF) techniques. The detection system consisted of one telescope made of a 18 μm thick Si detector, as ΔE and a 500 μm thick Si as residual energy detector. The telescope was mounted on a rotating arm. The arm was rotating with respect to the center of the circular chamber. Three angular settings were used: $θ_{lab}=0^{0}$ ($θ_{c.m.}=180^{0}$), 5^{0} and 10^{0} measured with respect to the center of the chamber.

A microchannel plate (MCP) detector was placed under vacuum, just upstream the entrance window, in order to give a signal whenever a ^{10}Be beam particle entered into the chamber. The MCP enables the counting of the beam particles, and at the same time, provides a fast signal for the ToF measurement. The beam intensity was kept $<1\times10^{7}$ pps due to the limitations required by the MCP.

Due to the extension of the target, the angle of the recoiling α-particles depends on $E_{c.m.}$ so it changes as the beam is slowed down in the ^{4}He gas; $E_{c.m.}$ and $θ_{c.m.}$ are reconstructed on an event-by-event basis from the energy and angle of the detected α-particles. The gas pressure was chosen to be sufficient to stop the beam before it reached the detector but not the recoiling α-particles. In figure 1 a sketch of the experimental set-up is shown.

The ToF measurement allowed to discriminate elastic from inelastic scattreing events and thus to confirm what was reported in [3] i.e. that the inelastic scattering contribution is not negligible as reported in [4] and it could change the conclusions drawn in [4] about the existence of the linear chain configuration in ^{14}C.
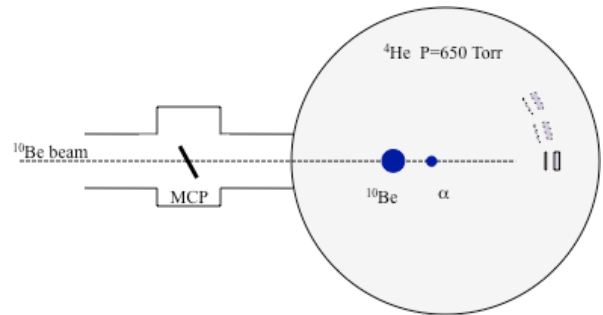
Fig. 1: Sketch of the experimental set-up.
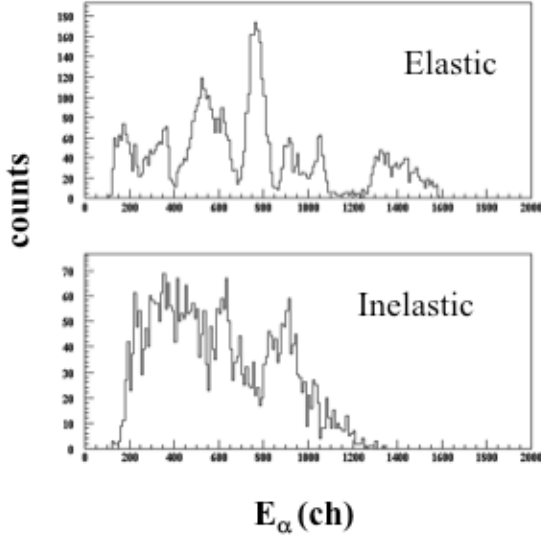
Fig. 2: Residual energy α-particle spectra at $\theta_{lab}=0^0$. Top: elastic scattering events. Bottom: inelastic scattering events.

RESULTS

Elastic scattering α-particle spectra were obtained by selecting the corresponding locus on the ToF-E plot. Similar plots were obtained for the inelastic scattering. In figure 2 are shown the residual energy spectra of α-particles of elastic (top) and inelastic scattering (bottom) events selected at $\theta_{lab}=0^0$. As one can see from the figure, the inelastic contribution is as large as the elastic one and shows some structures.

Although in [4] a similar technique was used, the authors claim that the contribution of inelastic scattering events is negligible. They also claim that the locus observed in [3] was not corresponding to true inelastic scattering events therefore the data of [3] were not "a credible source" for the discussion. Our results clearly contradict this conclusion, therefore the analysis performed in [4] has to be revised. It could be that, since the data of [4] are measured at lower beam energy, the inelastic scattering is reduced. However, a comparison of the inclusive excitation function measured in the present experiment with the one of [4] shows a perfect overlap thus confirming the inclusion of inelastic scattering in the case of the experiment reported in [4].

CONCLUSIONS

In this report, details of a first Resonant Elastic Scattering ^{4}He(^{10}Be, α) experiment performed at LNS have been discussed. The excitation function measured at $\theta_{c.m.}\approx180^0$ in the range 16-24 MeV shows the presence of many states in ^{14}C.

In the present experiment, contrary to the findings reported in [4] a large contribution of inelastic scattering events is observed. These processes contribute to a large fraction of the measured alpha production cross-sections. In the light of this result, the analysis that led to the determination of the α-linear-chain rotational band reported in [4], has to be revised.

[1] T. Suhara, Y. Kanada-En'yo, Phys. Rev. C **82**, 044301 (2010).
[2] M. Freer et al., Phys. Rev. C **90**, 054324 (2014).
[3] A. Fritsch et al., Phys. Rev. C **93**, 014321 (2016).
[4] H. Yamaguchi et al., Phys. Lett. B **766**, 11 (2017).

PREPARATION OF A TANTALUM OXIDE TARGET FOR TEST MEASUREMENTS OF THE ^{16}O(n,α) NUCLEAR CROSS SECTION

E.A. Maugeri (PSI), F. Mingrone (CERN), S. Urlass (CERN-TU Dresden)

According to the Nuclear Data High Priority Request List published by the Nuclear Energy Agency, (http://www.oecd-nea.org/dbdata/hprl/), values of the ^{16}O(n,α) reaction cross section in an energy range between the threshold (2.36 MeV) and 20 MeV are needed with high priority. These data are especially important for nuclear industry application. In fact, oxygen is one of the most common element present both in water (used as coolant and moderator in light water reactors and pressurized water reactors) and fuel oxide (UOX, MOX). Despite that, the value of its cross section is known with low accuracy, and discrepancies larger than 30% are present in both measured and evaluated data [1,2].

In addition, a precise measurement of the ^{16}O(n,α) cross sections close to the threshold will give very important information about the inverse reaction ^{13}C(α,n), which is the main source of neutrons for the s-process nucleosynthesis in AGB stars [3].

A project aimed to measure the ^{16}O(n,α) cross section up to 20 MeV was started at n_TOF-EAR1 (CERN, Switzerland) facility. Thanks to the powerful neutron source, consisting in a lead spallation target coupled with the 20 GeV/c pulsed neutron beam from the CERN Proton Synchrotron, the facility can achieve a neutron beam that spans over 11 orders of magnitude from tens of meV to several GeV.

Both gaseous and solid targets are going to be used since the use of complementary experimental method will help in reducing systematic uncertainties. The detection setup consists in a double Frisch-grid ionization chamber with common cathode.

This work reports on the production of a solid Ta_2O_5 target, prepared at PSI by anodic oxidation of a tantalum disk, used for preliminary tests. The target was prepared using the two electrodes cell depicted in Fig. 1.
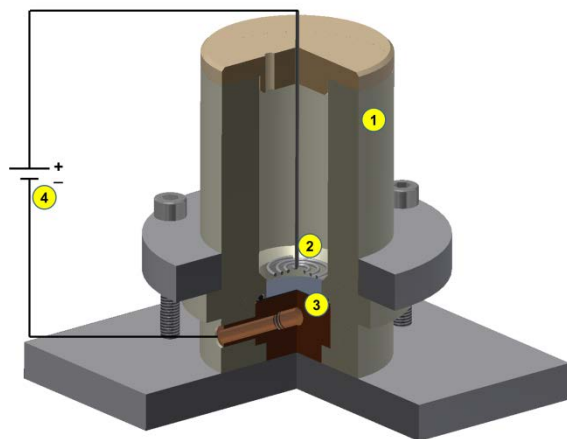
Fig. 1: Three dimensions schema of electrolytic cell.
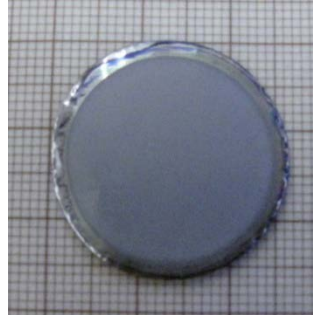
Fig. 2: Ta_2O_5 (central bluish-grey area) obtained by anodic oxidation of tantalum.

The body of the cell, 1 in Fig. 1, machined from polyvinylidene fluoride blocks, hosts a 20 mm platinum cathode, 2, facing a copper anode, 3. The electrodes were connected, via wires, to a DC-power supply (Sorensen® programmable DC power supply XHR 600-1.7), 4. A 0.025 mm thick tantalum disk (99.9%, Sigma-Aldrich) was placed on the top of the anode. The anodic oxidation was carried out in 10 ml of HNO_3 0.1 M, applying a potential of 210 V for 20 minutes.

Fig. 2 shows the resulting target characterized by a 20 mm diameter Ta_2O_5 film. The thickness of the oxide film was calculated as 401 nm, using the linear relationship between the thickness and the anodizing voltage reported in [4].

The target was glued on a 125 µm kapton foil shaped as to be inserted in the assembled detector, parallel to the electrodes. It was positioned at 5 mm to the cathode, so that only half of the detector was used (see Fig. 3). The chamber was filled with a 90% Ar + 10% CF_4 gas mixture and placed in beam with the Ta_2O_5 facing the neutron beam.
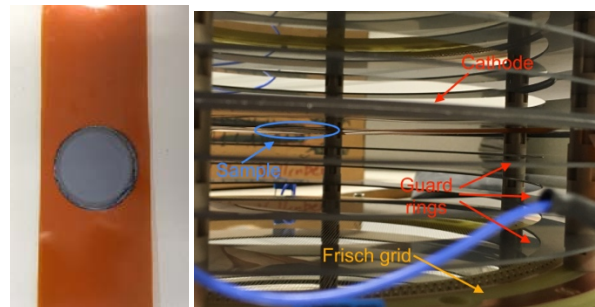
Fig. 3: Left: Ta_2O_5 glued on a 125µm kapton support. Right: picture of the assembled detector with the target inside, parallel to the detector.

The main goal of the test was to study the effect of the γ–ray burst, so-called γ-flash, in the detector. The γ-flash, in fact, deposits an amount of energy both in the detector and in the electronics that blinds the system

for a certain period. With the optimised setup used, the goal was to reduce this time to few microseconds so to have a clean access to the energy region of interest. In Fig. 4 an example of a detected event is shown. In this case, a 3 cm thick Pb filter was put in beam so to further decrease the effect of the γ-flash. Different preamplifiers were tested. It is possible to seen from the picture that for most of the preamplifiers the energy region from threshold up to 7 MeV was easily accessible. At higher energy range (up to 20 MeV) further offline analysis are needed for a proper evaluation. Two coincident signals can be identified in the cathode and anode output, one assigned to the (n,α) reaction on ^{16}O, the other, since below the reaction threshold, due to some background reaction.
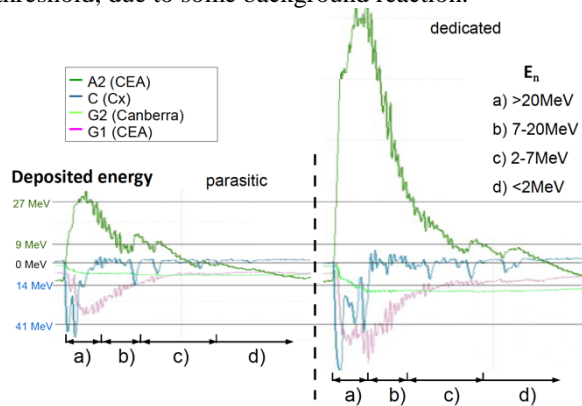
Fig. 4: Example of the output coming from different detector electrodes, each coupled to a different preamplifier.

A more detailed analysis to characterise the performance of the detector is ongoing, but the outcome of the already analysed test showed a positive hint on the feasibility of the measurements. Furthermore, a study is ongoing to identify the optimal characteristics of the target, starting from the outcome of the test. The final setup, including both the requirements for the electronics and the experimental system, will be decided in a few months, and the measurement will be performed at the end of 2018.

Acknowledgement

[1] S. Kunieda et al., Nucl. Data Sheets **118**, 250 (2014).
[2] M.B. Chadwick et al., Nucl. Data Sheets **118**, 1 (2014).
[3] M. Busso et al., Annu. Rev. Astron. Astrophys. **37**, 239 (1999).
[4] C.C. Sheng et al., Chin. Phys. B **21**, 088101 (2012).

ELECTROCHEMICAL DEPOSITION OF BERYLLIUM

E.A. Maugeri (PSI), J. Gartmeier (Univ. Bern & PSI), D.P. Herrmann (PSI)

A precise measurement of the ^{7}Be(n,α)^{4}He nuclear cross section at the energy range of interest for the Big-Bang nucleosynthesis, 10-100 keV, could solve the long lasting "Cosmological Lithium problem".

This measurement was recently performed at the new experimental area n_TOF-EAR2 (CERN, Switzerland) facility, where two targets of some micrograms of ^{7}Be, produced at PSI [1], were irradiated with 0.01 eV to 10 keV neutrons [2]. The upper neutron energy limit was imposed by the recovery time of the used silicon detectors (placed inside the neutron beam) after the γ-flash from the spallation target [3]. This energy range covered only to some extent the Big-Bang nucleosynthesis energy range. Therefore, further investigations must cover energies up to 100 keV. A prospective experiment could be performed at new designed (still under construction) high-flux neutron sources such as FRANZ (Stern Gerlach Zentrum, Germany) and SARAF (Soreq, Israel). In these cases neutrons, in the keV energy region, will be produced by the ^{7}Li(p,n)^{7}Be reaction using solid or liquid lithium targets. The advantages of these facilities, with respect to n_TOF-EAR2, are the higher neutron flux and the weaker γ-flash, which allow for using smaller amounts of radioactive ^{7}Be and avoid problems related to the detector recovery time, respectively.

The preparation of the target is one of the main issues related to this measurement. In a previous work, ^{7}Be targets were prepared by deposition of droplets and by molecular plating [1]. In the case of droplets deposition the obtained target was neither uniform nor homogenous, while the molecular plated targets were relative thick due to the deposition of Be in molecular form and due to the co-precipitation of different organic compounds.

This work explores the possibility of electrodeposition of metallic beryllium onto conductive backings from ionic liquids (ILs) media. This method could allow to obtain a more uniform and homogeneous beryllium layer, thin enough to be used as target for the measurements of the ^{7}Be(n,α)^{4}He cross section.

Therefore, a new three electrodes electrodeposition cell, based on the system designed in [4], was developed. The cell shown in Fig.1 consists of a central frame made in PVDF (1) with an opening 1 cm thick and 1 cm large. The working electrode (WE) (2) and the counter electrode (CE) (3) are made of titanium blocks, which can be screwed into the central frame. The sealing was improved placing Viton O-rings (not shown in Fig. 1) and two PVDF rings (4) between the central frame and both electrodes. The cell provides an internal empty volume of 3.14 cm^3. The cell has two openings in the top of the central frame. One is used to introduce reagents, while the second one is used to insert the reference electrode

(RE) (5). The electrodes are connected to a potentiostat/galvanostat, which, when operated in potentiostatic mode, allows to control the potential of the CE relative to the WE, in order to keep the potential difference between the RE and the WE stable at the required level. At the same time, the resulting current between the WE and the CE is measured and recorded.
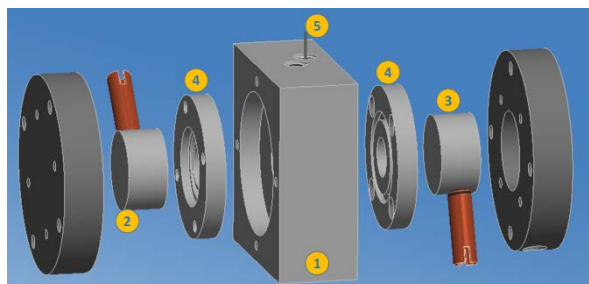
Fig. 1: Three electrodes electrodeposition cell.

The chosen IL should have a stability window larger than Be, i.e. the solvent must not be reduced before Be ions. Otherwise, the IL should completely solubilize Be ions, resulting in a homogeneous solution. N-nbutyl-N-methylpiperidinium [BMPi] bis((trifluoro-methyl)sulfonyl)imide [TFSI] was chosen among several other tested ILs, since it was possible to dissolve microgram amount of Be (enough for the planed experiment) and because it has low reduction potential.

This last feature is shown in the cyclic voltammogram (CV) of [BMPi] [TFSI], Fig. 2 black curve, obtained applying a scan rate of 20 mV s^{-1}. The electrochemical window of [BMPi] [TFSI] is between 0.3 V and -2.8 V with respect to the ferrocene/ferrocenium (Fc/Fc$^+$) redox potential. [BMPi] [TFSI] clearly decomposes at lower potentials. Two other series of cyclic voltammetry investigations were performed on two different Be compounds, Be(NO$_3$)$_2$ and BeSO$_4$, dissolved in [BMPi] [TFSI]. These investigations were carried out to identify the best conditions for reducing and depositing Be.

Fig. 2 shows also two examples of CVs, obtained imposing a scan rate of 1 mV s^{-1}, for Be(NO$_3$)$_2$ (blue curve) and BeSO$_4$ (red curve), respectively. Both curves show a peak at -1.76 V, attributed to the reduction of Be^{2+} to its metallic form. These results indicate that it is possible to reduce Be^{2+} in [BMPi] [TFSI], without reducing the solvent.

In the light of these results, an electrodeposition of Be on graphite (placed on the top of the WE) using [BMPi] [TFSI] as solvent, was attempted. Be(NO$_3$)$_2$ was used as starting material. A potential of -1.8 V was applied for 12 hours.
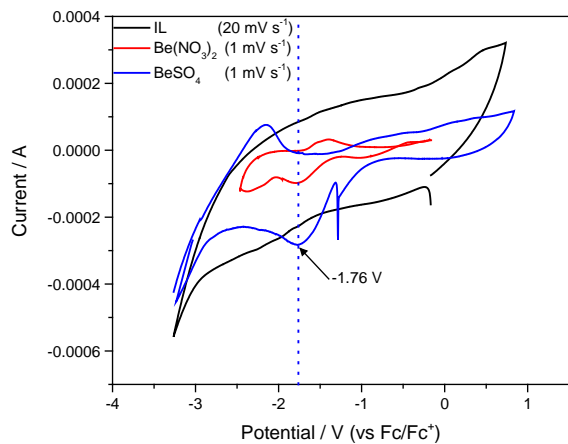
Fig. 2: CVs of pure [BMPi][TFSI], black curve, Be(NO₃)₂ and BeSO₄ in [BMPi][TFSI], red curve and blue curve, respectively.

Fig. 3: Picture of Be (dark ring) electrodeposited on graphite after applying a potential of -1.8 V for 12 hours.

A photograph of the resulting deposited layer is presented in Fig. 3. The Be electrodeposition results in a non-homogeneous layer characterized by a rim shape. Investigations to better understand this result and to improve the homogeneity and uniformity of the deposited layer are ongoing. In particular, the geometry of the used cell could have not provided a good contact between the WE and the backing. Other electrodeposition conditions such as deposition time, applied voltage, concentration of Be, starting chemical form of Be, e.g. BeSO₄, are considered for further optimization of the process.

Acknowledgement

[1]   E.A. Maugeri et al., JINST **12**, P02016 (2017).
[2]   M. Barbagallo et al., Phys. Rev. Lett. **117,** 152701 (2016).
[3]   C. Weiß et al., Nucl. Instrum. Methods Phys. Res., Sect. A **799**, 90 (2015).
[4]   A. Vascon, PhD Thesis, Fachbereich Chemie, Pharmazie und Geowissenschaften, Johannes Gutenberg-Universität, 2013.

ON THE EMMISION PROBABILITY OF THE 66.7 keV GAMMA TRANSITION IN THE DECAY OF ^{171}Tm

S. Heinitz, I. Kajan, R. Dressler (PSI), P. Reichel, N. Kivel (PSI/AHL)

INTRODUCTION

The radioactive isotope ^{171}Tm, $t_{1/2}$ = 1.92(1) a, is a β-emitter with a low Q-value of 96.4(10) keV [1]. It may be produced by neutron activation of ^{170}Er and is primarily measured by liquid scintillation counting. However, it also exhibits a weak γ-transition at 66.7 keV, which can be used to deduce its activity using HPGe detectors. The emission probability ε of this γ-line, however, has never been measured directly. The only tabulated value $\varepsilon_{66.7}$ = 0.14% (given with no uncertainty) dates back to 1964 [2]. Within this work, the γ-emission probability was calculated based on assumed probabilities of K and L shell electron transitions during the ^{171}Tm decay.

We have experimentally determined the gamma emission probability of the 66.7 keV line in the decay of ^{171}Tm using γ-spectrometry and inductively coupled mass spectrometry (ICP-MS). Using a set of two reference sources, namely ^{60}Co as primary standard and ^{44}Ti/^{44}Sc in secular equilibrium as secondary standards, we were able to deduce the absolute detection efficiency at 66.7 keV of the used γ-spectrometry setup with high precision.

EXPERIMENTAL

Radioisotopically pure ^{171}Tm was taken from leftovers of an earlier experiment performed in 2014, where 140 GBq of ^{171}Tm were produced and separated from 250 mg of 98.1% enriched ^{170}Er [3]. The specific activity of the sample was approx. 200 MBq/mL as of August 2017. An aliquote of 20 µL of this solution was diluted with 1 mL of distilled water. From this dilution, three different ^{171}Tm sources were prepared by evaporating one droplet (20 µL) on circular Teflon supports. A Mettler-Toledo AT261 DeltaRange (d = 0.01 mg) balance was used to gravimetrically trace the dilution and source preparation step. In addition a source was prepared from a stock ^{44}Ti/^{44}Sc solution by evaporating 20 µL of solution on a Teflon support. All sources were sealed using a 50 µm thick Kapton tape.

The sources were measured at a distance of 140(1) mm in front of a Canberra BE2825 planar HPGe detector with 0.066 % total efficiency at 1173 keV for at least 24 h to achieve not less than 10^4 counts in the regions of interest leading to counting uncertainty in the range of 0.3%. As primary reference a ^{60}Co source with an activity of 1831(7) Bq (certified on 01.07.2011 at 00:00 CET by Physikalisch-Technische-Bundesanstalt (PTB), Braunschweig, Germany) was used. The primary standard was measured five consecutive times, while the ^{44}Ti/^{44}Sc and each ^{171}Tm source were measured three times. The energy calibration of the

detector was performed by a mixed nuclide standard provided by the Czech metrology institute, Brno, Czech republic, containing ^{241}Am, ^{109}Cd, ^{139}Ce, ^{57}Co, ^{113}Sn, ^{85}Sr, ^{137}Cs, ^{60}Co and ^{88}Y with accurately known activities.

Additionally, the total weight contribution of the 171 isobar, i.e. the abundance of ^{171}Tm in the used solution was measured 8 times by HR-ICP-MS using an Element 2, Thermo-Fischer Scientific, Bremen, Germany, operated in low resolution mode and wet plasma conditions.

All uncertainties are calculated according to the "guide to the expression of uncertainty in measurement" GUM [4] and are given with a coverage factor k = 1, i.e. confidence level of about 68%, and given in brackets in units of last significant digit.

RESULTS

The measured γ-spectra of the ^{60}Co reference source, the ^{44}Ti/^{44}Sc and ^{171}Tm samples are given in Figure 1.
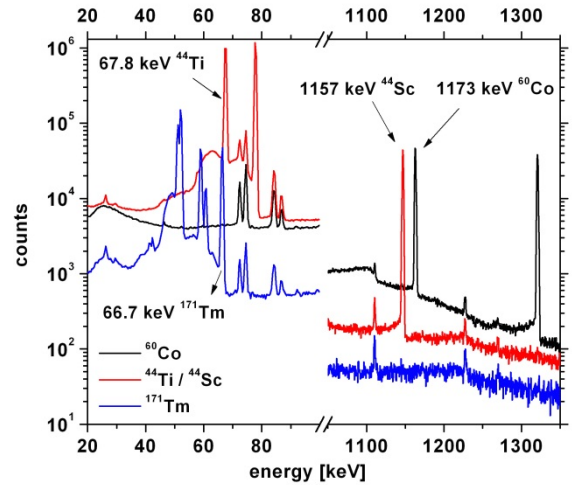
Fig. 1: Superimposed γ-spectra of ^{60}Co, ^{44}Ti/^{44}Sc and ^{171}Tm samples.

The activity of the ^{44}Ti/^{44}Sc source was determined to be 1288(7) Bq on 22.09.2017. We deduced the activity of ^{44}Sc by measuring the absolute count rate of its 1157 keV γ-line with ε_{1157} = 99.875(3)% [5], where the absolute efficiency was calculated from the slope between both ^{60}Co lines (ε_{1173} = 99.85(3)% and ε_{1332} = 99.9826(6)% [6]). The ^{44}Ti/^{44}Sc stock solution was prepared some years ago, therefore, both isotopes are in radioactive equilibrium. Subsequently, we determined the absolute efficiency of the γ-detector at the 67.8 keV ($\varepsilon_{67.8}$ = 93.0(15)% [5]) ^{44}Ti γ-line according to the deduced activity of ^{44}Sc and the 67.8 keV γ-count rate. True coincidence summing effects for the measured geometry at 140 mm distance

were calculated utilizing EFFTRAN code [7] and were taken into account for all measured nuclides. Due to the close proximity to the 66.7 keV γ-line of ^{171}Tm, no correction for attenuation effects in air, Aluminium or Teflon was needed.

Finally, the concentration of ^{171}Tm/^{171}Yb was measured by ICP-MS to be 260.3(73) ng/g in the prepared solution. Using the known amounts of evaporated solution to prepare the ^{171}Tm sources, the last Tm/Yb separation date 01.11.2014 and the ^{171}Tm half-life, we compute the 66.7 keV emission probability to be

$$\varepsilon_{66.7} = 0.159(6)\%$$

This value is in slight disagreement with the value determined over 50 years ago, when no commercial High Purity Germanium detectors were available.

_____

[1]   Baglin, C.M., Nuclear Data Sheets **96**, 399 (2002).
[2]   Hansen, G, Risø Report **92**, (1964).
[3]   Heinitz, S. et al., Rad. Act. **105**, 801 (2017).
[4]   Joint Committee for Guides in Metrology, **100** (2008).
[5]   Chen, J. et al., Nuclear Data Sheets **112**, 2357 (2011).
[6]   Browne, E. et al., Nuclear Data Sheets **114**, 1849 (2013).
[7]   Vidmar, T., Nucl. Inst. Met. A **550**, 603 (2005).

MEASUREMENT OF THE NEUTRON CAPTURE CROSS SECTION OF ^{171}Tm

C. Guerrero, J. Lerendegui-Marco (Univ. Sevilla), C. Domingo-Pardo (IFIC), M. Paul,
M. Tessler (Hebrew University), R. Dressler (PSI), N. Kivel (PSI/AHL), S. Heinitz, E.A. Maugeri, D. Schumann
(PSI) and the n_TOF Collaboration and The SARAF Team

The neutron capture cross sections of several unstable isotopes acting as branching points in the s-process are crucial for stellar nucleosynthesis studies. However, measuring them is a challenge due to the difficulties in producing sufficient sample material as well as to the background associated to the activity of the isotopes involved. The unstable isotope ^{171}Tm ($t_{1/2}$=1.92 years) is part of the branching at A~170 and has never been measured in the full energy range of astrophysical importance, which we have done in this work.

The high quality of the ^{171}Tm target has been key in the success of the experiments presented herein. In the context of a larger project involving the production of ^{79}Se, ^{147}Pm, ^{163}Ho and ^{204}Tl targets as well, a pellet of 240 mg ^{170}Er$_2$O$_3$ enriched to 98.1% was irradiated for 55 days at the ILL high flux reactor, where neutron capture reactions in ^{170}Er produced sizable quantities of ^{171}Er that decayed into ^{171}Tm. Following chemical separation, purification and determination of the isotope composition at PSI, a total of 1.23(3)x10^{19} atoms of ^{171}Tm were deposited in circular areas (22 mm in diameter) onto two 5 µm thick Al foils and then placed face-to-face into a 60 mm diameter plastic ring that served as the target holder (see Ref. [1] for details).

Two complementary experiments have been carried out at the CERN n_TOF [2] and the SNRC LiLiT [3] facilities by time-of-flight and activation, respectively. The result, the first of its kind, consists of a set of 28 new resonances (Fig. 1) and a MACS value at 30 keV of 207±4$_{stat}$±25$_{syst}$ mb calculated form four decay lines of ^{172}Tm after activation (Fig.2). This value is significantly smaller than all previous predictions and 50% lower than the preliminary result of the only other experiment attempted to date. Our result affects the nucleosynthesis at the A~170 branching, namely, the ^{171}Yb abundance increases by 25% in the material lost by Asymptotic Giant Branch stars, providing a better agreement with the available pre-solar SiC grain measurements. The full details of the experiment and the analysis reported herein are given in Ref. [4].
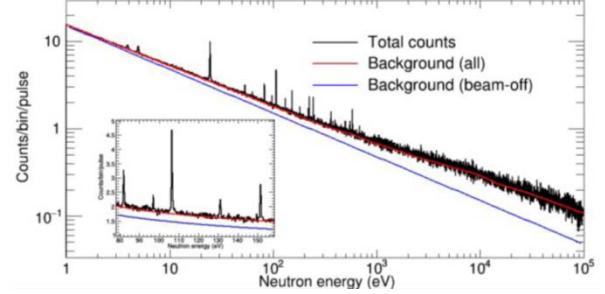
Fig. 1: Neutron energy distribution of the ^{171}Tm and background measurements at the CERN n_TOF facility, with ^{171}Tm resonances showing up above the background level.
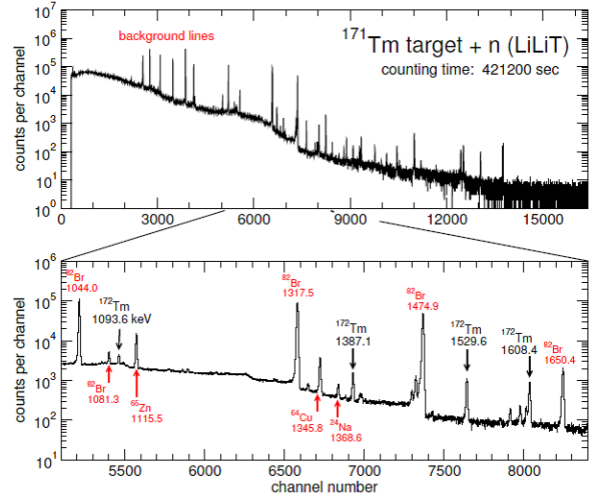
Fig. 2: Decay spectrum after activation of the ^{171}Tm target at LiLiT: four decay lines from ^{172}Tm have been used to extract the MACS values.

[1] S. Heinitz et al., Radiochim. Acta **105**, 801 (2016).

[2] C. Guerrero et al., Eur. Phys. J. A **49**, 27 (2013).

[3] S. Halfon et al., Rev. Sci. Instrum. **85**, 056105 (2014).

[4] C. Guerrero et al., "Neutron capture on the s-process branching point ^{171}Tm via time-of-flight and activation", submitted to Phys. Rev. Lett (December 8, 2017).

PRODUCTION CROSS SECTIONS OF LONG-LIVED LANTHANIDES IN PROTON-IRRADIATED HEAVY METAL TARGETS: LEAD & TANTALUM

Z. Talip, R. Dressler, D. Schumann (PSI), J. C. David (Irfu CEA & University Paris-Saclay),
E. Strub (Univ. of Cologne)

Cross section data for the production of long lived radionuclides are crucial for the management of decommissioning and disposal of waste accelerator driven systems (ADS) and spallation neutron facilities (SNF). In order to shed light on the contribution of long-lived α-emitting lanthanides (^{154}Dy, ^{148}Gd and ^{146}Sm) to the overall radiotoxicity of the targets, reliable cross section data of these radionuclides are needed.

Chemical separation of α-emitting lanthanides from proton irradiated Pb and Ta targets were previously reported [1, 2]. In this study, experimental cross section results are compared with the theoretical calculations obtained by a combination of the INCL++ code (Liège intra-nuclear cascade) [3, 4] and the ABLA07 code (de-excitation phase) [5].

Production Cross Sections

Cumulative cross sections of ^{nat}Pb(p,x)^{148}Gd, ^{nat}Pb(p,x)^{154}Dy and ^{nat}Ta(p,x)^{148}Gd, ^{nat}Ta(p,x)^{148}Gd were deduced by using α-spectrometry results with equation 1;

$$\sigma = \frac{\lambda\, C\, e^{\lambda t_w}}{N_t\, \phi\left(1-e^{-\lambda t_i}\right)\left(1-e^{-\lambda t_c}\right)\varepsilon\, I\, Y} \quad (1)$$

where λ is the radionuclide decay constant, C is the number of observed counts, t_w is the time between irradiation and counting, t_i is the irradiation time, t_c is the counting time, N_t is the number of target atoms, ϕ is the proton flux density, ε is the detector efficiency, I is the branching ratio and Y is the total chemical yield.

^{148}Gd

Gd samples were measured at different sample detector distances (SDDs), depending on the activity of the samples. Figure 1 shows the recorded α-spectrum of a Gd deposited sample for 220 MeV proton-irradiated Ta in comparison with Monte-Carlo simulations. The α-spectra of 220 MeV proton-irradiated Ta before and after Gd separation were simulated using the Advanced Alpha-spectroscopy SImulation program (AASI) [6, 7]. As it was shown, it was not possible to detect ^{148}Gd in the samples irradiated with proton energies less than 560 MeV before a chemical separation. However, after separation ^{148}Gd could be quantified in all the samples.
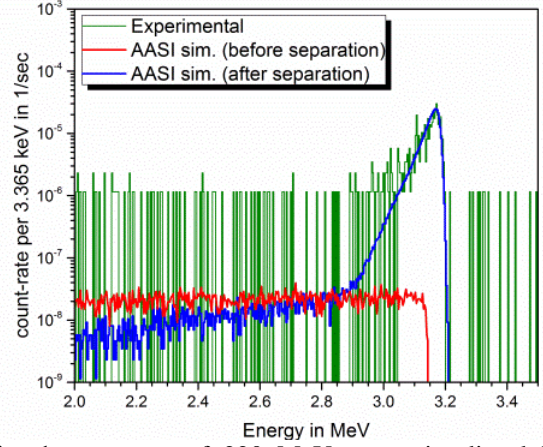
Fig. 1: α-spectra of 220 MeV proton-irradiated Ta target after separation (green) (SDD: 2.64 mm, counting time: 10 days), corresponding AASI simulation (blue) and AASI simulation for the Ta target before separation (red).

Figure 2a and b show the comparison of the experimental ^{148}Gd cross sections with the theoretical calculations for Pb and Ta targets, respectively. The experimental results are in very good agreement with theoretical calculations throughout the complete energy range.
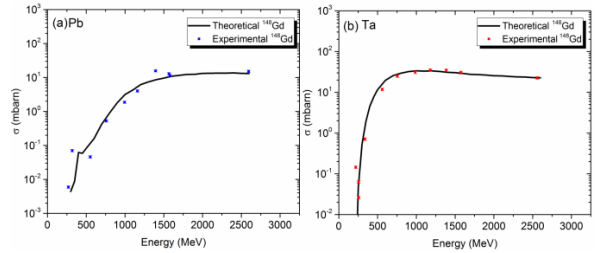
Fig. 2 : Comparison of the experimental and calculated excitation function of the production of ^{148}Gd in Pb (a) and in Ta (b).

Experimental production cross section data of ^{148}Gd in proton-irradiated Pb targets are presented for the first time. Experimental production cross sections data of ^{148}Gd in Ta for proton energies higher than 450 MeV had previous been reported by Kelley *et al.* [8] and Titarenko *et al.* [9] but without chemical separation. Figure 3 shows the comparison of the Ta results of this study with the literature data. It was observed that the theoretical results are closer to Kelleys and our experimental findings while the results of Titarenko deviate considerably in the intermediated energy range from 750 MeV to 1250 MeV.
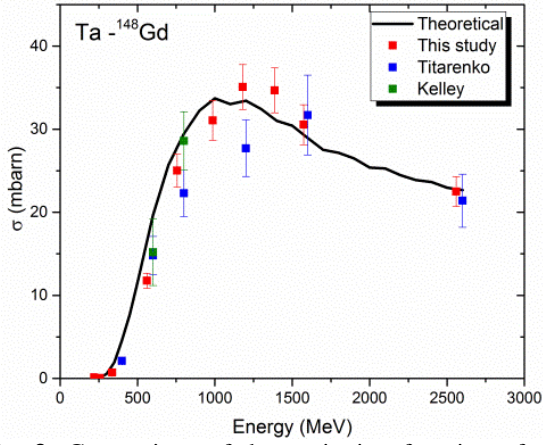
Fig. 3: Comparison of the excitation function of the production of ^{148}Gd in Ta (proton energy > 450 MeV) with theoretical results and literature data.

^{154}Dy

Production cross sections for ^{154}Dy in Pb and Ta are reported for the first time. Similar results have been observed for the production cross section of ^{154}Dy in Pb and Ta targets (Figure 4). It was observed that the cross sections are underestimated by a factor of ~3.
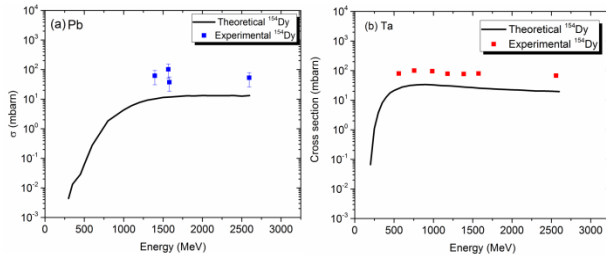
Fig. 4: Comparison of the experimental and calculated excitation functions of the production of ^{154}Dy in Pb (a) and in Ta (b).

It has to be pointed out that the ^{154}Dy cross section results include high uncertainties due to its accepted half-life value. More accurate half-life measurements are needed to increase the accuracy of the ^{154}Dy cross section results. Therefore, cross section results (σ) of ^{148}Gd and ^{154}Dy should be re-calculated with new adapted half-life values ($T_{1/2}^{*}$) according to the following equation.

$$\sigma* = \sigma \, \frac{T_{1/2}^{*}}{T_{1/2}} \qquad (2)$$

^{146}Sm and ^{150}Gd

In this study, Sm samples were measured with the smallest possible SDD (2.64 mm) and ~ 31 % efficiency. However, even after 45 days measurement, no ^{146}Sm peak (E_α= 2.455 MeV, η=100%) was visible. The minimum detectable activity for a CANBERRA 450 mm^2 α- PIPS detector is 0.42 mBq (for 31 % efficiency, background counts: 6cts/day, counting time: 15 hr) [10]. Figure 5 shows that the expected ^{146}Sm activities (based on INCL++ and ABLA07 calculations) for all the samples are several

magnitudes lower than the detection limit of the α-spectrometry.
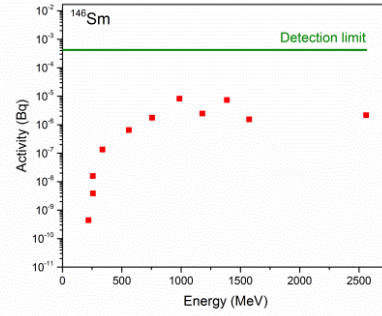
Fig. 5: Theoretical ^{146}Sm activities in proton-irradiated Ta targets (green line shows the detection limit of the 450 mm^2 α-PIPS detector).

Also a ^{150}Gd peak (2.726 MeV) was not visible in any of the samples. Theoretical calculations show that there is a four order of magnitude ratio between the expected highest activities for ^{148}Gd and ^{150}Gd in proton-irradiated Ta targets (^{148}Gd: 13 Bq and ^{150}Gd: 4 10^{-4} Bq). As it was mentioned before, the detection limit of the α- PIPS detector is 4.2 10^{-4} Bq. In addition, there is a five order of magnitude difference between the accepted half-life values of ^{148}Gd and ^{150}Gd, which makes it difficult to measure the activity of ^{150}Gd in these samples.

According to the theoretical calculations, cross section of spallation nuclides should increase with increasing target mass number. In agreement with the theoretical calculations, higher cross section results were obtained for Ta targets.

Comparisons of the experimental results with theoretical calculations show a satisfactory agreement for ^{148}Gd. However, the theoretical cross sections for ^{154}Dy are underestimated [11, 12], which could partly be due to the uncertainty of its accepted half-life value.

[1]   Z. Talip, Ann Rep. Lab. of Radiochem (2015).
[2]   Z. Talip, Ann Rep. Lab. of Radiochem (2016).
[3]   D. Mancusi et al., Phys. Rev. C **90**, 054602 (2014).
[4]   A. Boudard et al., Phys. Rev. C **87**, 014606 (2013).
[5]   A. Kelic et al., Trieste, Italy, 2008.
[6]   E. Maugeri et al., J. Instrum. **12**, 02016 (2017).
[7]   T. Siiskonen, Nucl. Instrum. Methods Phys. Res. Sect. A **550**, 425 (2005).
[8]   K. Kelley, Nucl. Phys. A **760**, 225 (2005).
[9]   Y. Titarenko et al., Phys. At. Nucl. **74**, 573 (2011).
[10] Canberra Appl. Note, C39168, **99**, 1 (2011).
[11] Z. Talip et al., Anal. Chem **89**, 6861 (2017).
[12] Z. Talip et al., Anal. Chem **89** (24) 13541 (2017).

PRODUCTION CROSS SECTIONS OF ^{36}Cl IN PROTON-IRRADIATED TANTALUM

Z. Talip, R. Dressler, D. Schuman (PSI), C. Vockenhuber (ETHZ),
J. C. David (Irfu, CEA & University Paris-Saclay), E. Strub (Univ. of Cologne)

The production cross section of the long-lived β-emitter ^{36}Cl ($T_{1/2}$= 3.01 × 10^5 y) in proton irradiated heavy metals, which are used as a target material for spallation neutron sources, are of special interest due to its long half-life, volatility and high mobility in the geosphere.

Previously, the excitation functions of the production of ^{36}Cl in the target materials Pb, Bi, and lead-bismuth-eutectic samples had been reported [1, 2]. However, there is no experimental data available for the excitation functions of the production of ^{36}Cl in Ta by proton irradiation. In this study, experimental results are compared with the theoretical calculations obtained by a combination of the INCL++ code (Liège intra-nuclear cascade) and the ABLA07 code (de-excitation phase).

Separation of Cl from proton irradiated Ta targets was reported in a previous report [3]. After separation, the ^{36}Cl/Cl ratio measurements were performed at ETH Zurich (Laboratory of Ion Beam Physics) at the 6 MV EN TANDEM Accelerator Mass Spectrometry (AMS) facility [4].

Uncertainties due to the AMS measurements were between 2-17%. Blank results showed that cross contaminations during sample preparation should be taken into consideration. Therefore, blank corrections were performed for all the samples. Only the data which have values significantly higher than blanks were used for the cross section calculations.

Production Cross Sections

Cumulative cross sections of ^{36}Cl were calculated with the following equation (^{36}Cl/^{35}Cl ratios were converted to ^{36}Cl/Cl ratios by applying the conversion factor 0.7577);

$$\sigma = \frac{R_c \; R_s \; N}{R_r \; N_t \; \phi \; t_i} \qquad (1)$$

where R_c is the nominal isotopic ratio in reference standard (the nominal ^{36}Cl/Cl ratio of the internal standard is 17.36 ± 0.35 × 10^{-12} (K382/4N) [4], R_r is the measured isotopic ratio in reference standard, R_s is the measured isotopic ratio in the sample, λ is the radionuclide decay constant, N is number of carrier atoms, t_w is the time between irradiation and counting, t_i is the irradiation time, N_t is the number of target atoms, ϕ is the proton flux density.
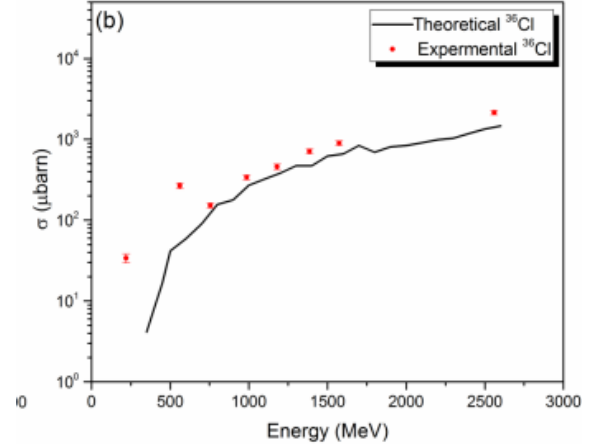
Fig. 1: Experimental and theoretical cross section results for ^{36}Cl in proton-irradiated Ta.

Figure 1 shows the comparison of the experimental and theoretical cross section results. Experimental cross section results are higher for the low energy (<750 MeV) proton-irradiated samples compared with the theoretical predictions. Interestingly, similar results had been observed for ^{36}Cl in proton-irradiated Bi and Pb targets [1]. At low incident proton energies, only the nuclides near the mass of the target are produced and at energies around 500 MeV, fission and spallation processes occur. Moreover, the cross section for multi-fragmentation increases by an order of magnitude, when the incident proton energies are between 1.0 GeV and 10 GeV [5]. It is expected that the origin of the ^{36}Cl formation is also a fragmentation process. Therefore, it is difficult to explain the observed high cross section results of ^{36}Cl for the low energy proton-irradiated Ta samples. However, there is a good agreement between the experimental and theoretical results for the high energy (>750 MeV) proton-irradiated samples.

_____
[1] D. Schumann et al., Nucl. Data Sheets **119**, 288 (2014).
[2] B. Hammer-Rotzler et al., Radiochim. Acta **103**, 745 (2015).
[3] Z. Talip et al., Ann Rep. Lab. of Radiochemistry (2016).
[4] M. Christl et al., Nucl. Inst. Met. Phys. Res. Sec. B, **294**, 29 (2013).
[5] J. W. Negele and E. Vogt, Advances in Nuclear Physics, New York, 2001.

SEPARATION OF LONG-LIVED RADIONUCLIDES FROM PROTON-IRRADIATED TUNGSTEN TARGETS

Z. Talip, B. Schacherl, A. Vögele, D. Schumann (PSI), E. Strub (Univ. of Cologne)

INTRODUCTION

The European Spallation Source (ESS), which is going to be the world's most powerful neutron source, is being built in Sweden [1]. 4-tonne helium cooled pure W is the proposed material for the ESS spallation target due to its high atomic number to maximize the neutron production. The target will be a 2.5-meter diameter rotating wheel with an assembly of roughly 7000 W bricks [1]. The radionuclide inventory and production cross section data are essential for the safety of this facility. Especially, accumulation of long-lived radionuclides will have to be taken into consideration, with respect to the final disposal of the irradiated W target material.

The production cross sections of ^{148}Gd in W targets irradiated with protons at different energies has previously been studied by Kelley *et al* [2] and Titarenko *et al* [3]. They performed α-spectrometry measurements without any prior chemical separation of Gd. However, in our previous studies [4, 5], it was shown that a radiochemical separation is necessary;

- to be able to measure the cross sections of the longer lived ($T_{1/2}$: $3\ 10^6$ years) α-emitter ^{154}Dy,
- to be able to detect ^{148}Gd in the samples irradiated with proton energies less than 560 MeV,
- to decrease the uncertainty of the ^{148}Gd cross section measurements due to the reduction of self-absorption in the prepared α-samples.

Therefore, in this study, radiochemical separation procedures were developed to separate long-lived alpha emitters (^{154}Dy, ^{148}Gd, and ^{146}Sm) from p-irradiated W targets.

EXPERIMENTAL

Proton irradiations of W targets were performed with the stacked foil technique between 1993-1996 at the SATURNE II synchrotron of the Laboratorie National Saturne (LNS) at Saclay [6]. Monitoring of the proton fluence was done with the ^{27}Al(p,3p3n)^{22}Na reaction. The irradiation details of the samples are given in Table 1.

Tungsten samples were dissolved in concentrated HF and HNO$_3$. The chemical yields for the separation of W and lanthanides (Ln) were followed by adding the γ-emitter ^{187}W ($T_{1/2}$: 23.72 h) and ^{166m}Ho ($T_{1/2}$: 1200 y) tracers, respectively. Similar to the previous study, iodine and chlorine (with 3 mg iodine as stable carrier in form of NaI, Woodward Corporation, U.S.A. and 5 mg chlorine in form of NaCl, Riedel de-Haen) were distilled into an aqueous hydrazine solution (1:1, total 10 mL) and then, precipitated as AgCl and AgI [5]. After the distillation, the remaining solution in the reaction vessel was transferred into a centrifuge tube

by adding 7 M HNO$_3$. First, it was centrifuged to separate H$_2$WO$_4$. Then, 1 mL La (1 mg La standard for ICP) and 1 mL conc. HF were added to precipitate LnF$_3$. It was observed that W was not completely separated. Therefore, before dissolving the LnF$_3$, 2 mL 6 M NH$_3$ was added to dissolve remaining H$_2$WO$_4$ in the samples. Then, the LnF$_3$ precipitate was dissolved in 7 M HNO$_3$/ 0.5 M H$_3$BO$_3$. The pH was adjusted to ~ 1 and the solution was loaded onto an Aminex cation exchanger (HPX87H Bio-Rad, NH4$^+$ form, particle size 7-11 μm) to perform lanthanide separation. Further separation of the purified lanthanides was achieved with TRISKEM Ln Resin.

Tab. 1: Description of the p-irradiated W samples.

Sample	Proton energy (MeV)	Fluence (cm^{-2})	Irradiation time (s)	Target (mg)
WWSR241	2560	1 10^{15}	63600	161
WWSC193	1572	3 10^{14}	60180	165
WWSM251	1386	1.3 10^{15}	70980	165
WWSD193	1177	3.7 10^{14}	74040	154
WWSN251	986	1.4 10^{15}	60480	162
WWSE212	755	2.9 10^{14}	86940	315
WWSF212	560	3.1 10^{14}	91260	306
WWSG212	335	2.4 10^{14}	121200	320
WWSH212	254	1 10^{14}	76200	324
WWSK212	256	4.4 10^{14}	67320	322
WWSP181	220	1 10^{14}	55800	164

RESULTS & CONCLUSION

Lanthanides separation from W

Figure 1 shows an example of γ-spectra before and after Lns separation. The LaF$_3$ precipitate was completely separated from W and an average 91% Ln separation yield was obtained. (Table 2).

Fractional lanthanides separation

In the previous studies, DOWEX cation exchanger - α-hydroxyisobutryric acid (α-HIB) separation system was used to separate lanthanides from proton irradiated Pb and Ta targets [4,5]. In this study, Aminex cation exchanger was used to decrease the decontamination factor for the individual fractions [8, 9]. Initially, α-HIB concentrations were optimized to obtain the best separation (Figure 2). The better resolution was observed with Aminex resin compared to the DOWEX cation exchanger [5].
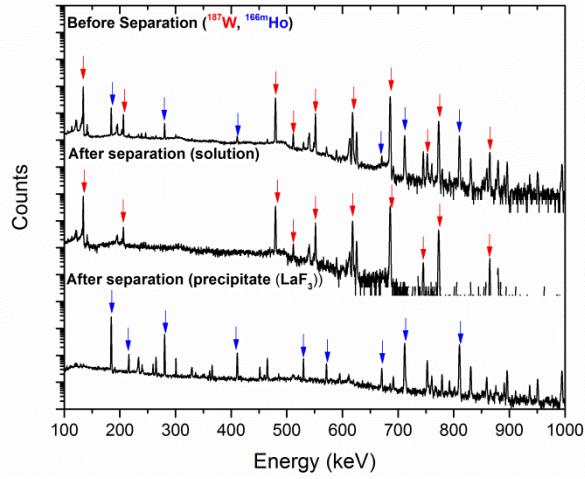
Fig. 1: An example of the γ-spectra of the W sample before and after Lns separation (blue and red arrows present gamma lines of [187]W and [166m]Ho, respectively).
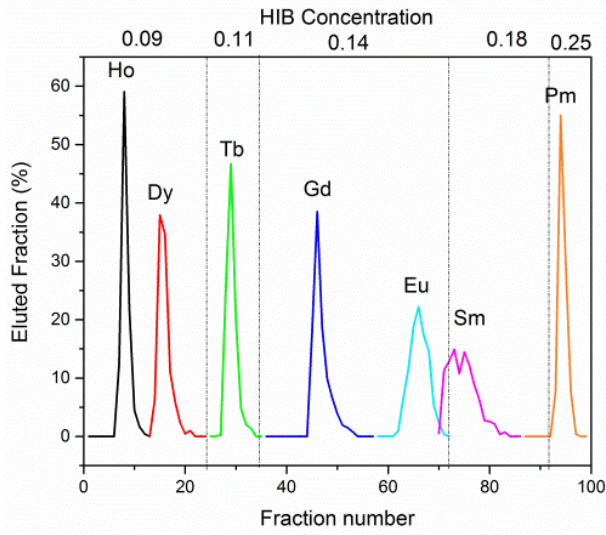
Fig. 2: An example of the separation profile of lanthanides in the Aminex cation exchanger and α-HIB separation system with gradient elution technique.

Sample preparation for α-spectrometry

The molecular-plating technique was used to prepare thin layers of the individual Ln fractions of [154]Dy and [148]Gd in W. Preparation and characterization of the homogeneous Lns samples were described in [10].

Gamma-spectrometry was used to determine the separation yields of the samples after each step (distillation, ion exchange (on both AMINEX resin and TRISKEM Ln resin), and molecular plating) (Table 2). To be able to perform yield calculations with γ-spectrometry, after each separation step, the samples were measured using the same geometry, distance to detector and volume.

Tab. 2: Chemical yields of Gd and Dy from p-irradiated W samples after distillation, Aminex and Ln resin, molecular plating and total.

Sample	Distillation	Aminex + Ln Resin		Molecular Plating		Total	
		Dy	Gd	Dy	Gd	Dy	Gd
WWSR241	88	95	99	99	91	83	79
WWSC193	89	94	94	99	88	86	74
WWSM251	97	96	96	94	77	90	72
WWSD193	97	99	96	96	66	92	61
WWSN251	93	100	99	98	65	91	60
WWSE212	74	99	98	98	83	72	60
WWSF212	90	100	96	96	89	86	77
WWSG212	95	100	92	99	87	94	76
WWSH212	92	100	89	99	36	91	30
WWSK212	93	95	96	92	84	81	75
WWSP181	95	94	100	67	95	60	90

The measurements (α-spectrometry and accelerator mass spectrometry) to obtain the cross-sections and corresponding excitation functions are currently ongoing.

ACKNOWLEDGEMENT

[1] https://europeanspallationsource.se/spallation.
[2] K. C. Kelley et al., Nucl. Phys. A **760**, 225 (2005).
[3] Y. E. Titarenko et al., Phys. At. Nucl. **74**, 573 (2011).
[4] Z. Talip et al., Anal. Chem. **89**, 6861 (2017).
[5] Z. Talip et al., Anal. Chem. **89**, 13541 (2017).
[6] M. Gloris, PhD thesis, Hannover University, 1998.
[8] G. Höhlein et al., Radiochem. Acta **11**, 3 (1969).
[9] E. Dadachova et al., Anal. Chem. **66**, 4272 (1994).
[10] Z. Talip et al., Ann Rep. Lab. of Radiochem., (2016).

CHARACTERIZATION OF ALPHA SOURCES PREPARED BY MOLECULAR PLATING TECHNIQUE

Z. Talip, E.A. Maugeri, R. Dressler, D.P. Herrmann, D. Schumann (PSI), P. Vontobel (PSI/NIAG),
E. Muller (PSI/LBR)

The quality of α-spectrometry can be improved by sample preparation techniques. In this study, the molecular plating technique was used to prepare alpha emitting lanthanide (^{148}Gd and ^{154}Dy) samples for α-spectrometry.

There are three important parameters to be considered:
- high deposition yields, to decrease the uncertainty due to low counting statistic;
- thin samples, to avoid self-absorption and low-energy tailing;
- homogeneous activity distribution, to avoid differences in counting efficiency.

The preparation of ^{148}Gd and ^{154}Dy samples from proton-irradiated Pb targets by molecular plating technique was reported in [1]. In this study, the characterization of these samples was performed by γ-spectroscopy, scanning electron microspectroscopy coupled with focused ion beam (SEM-FIB) and radioimaging. In addition, the effects of differently shaped Pt anodes and different stirring modes on the homogeneity of the molecular plated samples were investigated.

Deposition yields: The count rate of the tracer (^{153}Gd) in the initial solution and in the electrolyte solution (after molecular plating) were measured (after evaporation of the solvents to dryness in 20 mL glass vials) with γ spectrometry to determine the deposition yields. The spectra were analyzed with Canberra's Genie2000® software package.The results reported in the previous reports show the reproducibility of the applied procedure. In average 90% Gd and 94% Dy deposition yields were obtained [1].

Thickness: The obtained molecular plated samples were coated with a 30 nm gold layer, using the UNIVEX 450 (Leybold vacuum) thermal evaporation system (operational vacuum 10^{-4} to 10^{-6} mbar). This avoided contamination of the α-detectors by sputtering, due to the small sample to detector distances (SDD). This layer is sufficiently thick to stop recoil nuclei but significantly smaller than the stopping range of α- particles [1]. The coated area was chosen bigger than the deposited area to cover the entire surface of the samples (Fig. 1).
SEM-FIB technique was implemented to determine the thickness of the deposited layer.
A carbon layer (200-600 nm) was deposited by focused ion beam deposition on a chosen area of the sample before thickness measurement, to avoid alteration of the surface due to the Ga-ion beam. Then, a wedge angle was prepared by FIB milling

perpendicular to the sample. The same procedure was applied to non-deposited (Fig. 2a) and to a Gd deposited carbon backing (Fig. 2b). Comparison of the two images shows the thickness of the deposited layer to be ~2.5 µm.
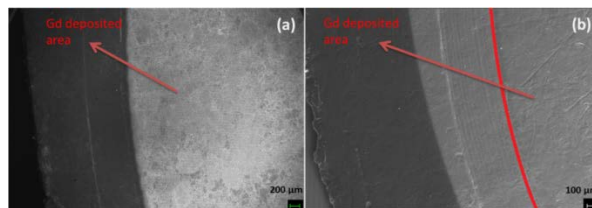
Fig. 1: SEM image of the edge of the Gd deposited carbon layer before (deposited area: 3.14 cm^2) (a) and after gold coating (b) (gold coated area: 3.80 cm^2).
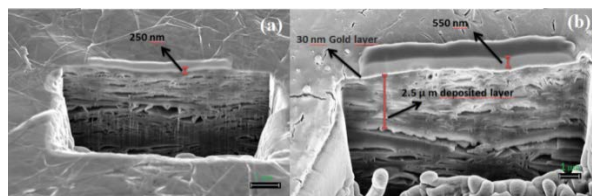
Fig. 2: Comparison of the SEM image of the carbon foil before (a) and after Gd deposition (b) with wedge angle prepared by FIB-milling perpendicular to the sample, showing the thickness of Gd deposited layer.

Homogeneity: The homogeneity of the samples was investigated by autoradiography, After molecular plating, a Typhoon FLA 7000 IP laser scanner, equipped with BAS-IP MS 2040 E super resolution imaging plate was used to obtain autoradiographs of the Gd and Dy deposited samples. The samples were placed over the film for one hour and the data were analyzed with the ImageJ software.

Molecular plated samples without stirring: non-homogeneous α-source
15 samples were prepared without stirring of the electrolyte solution during the molecular plating. Figures 3a and b show an example of radioimaging (RI) where the 3D autoradiograph and the activity distribution for a Gd deposited sample, respectively, are presented. All the samples were analyzed and the results showed that the α-particles were distributed over the whole surface of the deposited layer. However similar ring-shaped activity distribution was observed for all the obtained samples, giving rise to non-homogeneous sources.
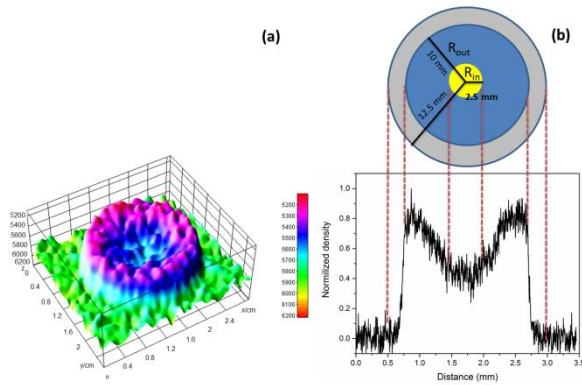
Fig. 3: After molecular plating (with spiral anode), RI 3D graph (a) and [153]Gd activity distribution (b).

- *Evaluation of the uncertainty of the efficiency for the non-homogeneous sources*

The efficiency of the α-detector depends on sample and detector geometry, but unlike the γ-spectrometry systems, it does not vary with energy of the α particles. Therefore, an [241]Am source was used for the efficiency calibration of the detectors. Counting at a defined solid angle (Ω) is the most accurate method for activity measurements with α-spectrometry. The obtained non-homogeneous source (Fig. 3a) was considered to be a combination of concentric rings with constant solid angle [2, 3]. The solid angles were calculated with a combination of two circular sources with radius of R_{in} (2.5 mm) and R_{out} (10 mm), respectively (Figure 3b). The loss of α-particles due to self-absorption into the sample or into the detector are considered negligible. Therefore, the detector efficiency (ε) equals to the geometric efficiency (ε_G).

$$\varepsilon = \varepsilon_G = \frac{\Omega}{4\Pi}$$

Efficiencies of circular sources, ε_{in} and ε_{out} were obtained experimentally with certified [241]Am standard sources (20 mm and 5 mm diameter) from PTB (Physikalisch-Technische Bundesanstalt, Braunschweig/Germany) for the used SDD (2.64, 10.64 mm) appling the following equation:

$$\varepsilon_{ring} = \frac{R_{out}^2 \varepsilon_{out} - R_{in}^2 \varepsilon_{in}}{R_{out}^2 - R_{in}^2}$$

where: R_{out}= 10 mm, ε_{out}= 0.31227, R_{in}: 2.5 mm and ε_{in}= 0.36444 for 2.64 mm SDD; while ε_{out}= 0.13949 and ε_{in}= 0.17618 for 10.64 mm SDD, respectively. The background level of the autoradiograph is calculated from the outer circle, which has a radius of 12.5 mm (Figure 3b). After normalization to the area of each region, the background is subtracted from the integrated counts. An average of the counts for the measured 15 samples was taken and the relative amount of activity in ring–shaped (0.97) and circular shaped sources (0.03), were used as a weighting factor to calculate the total efficiency of the samples.

$$\varepsilon = \varepsilon_{ring}\, weight_{ring} + \varepsilon_{circle}\, weight_{circle}$$

As a consequence, inhomogeneity of the samples causes an uncertainty of less than one percent for the efficiency [4].

- *Molecular plated samples with stirring:*

To improve the homogeneity of the sample, the anode shape was varied and stirring was applied.

The lower Gd deposition in the centre (Fig. 3) could be caused by the used spiral shaped anode, which could have induced a lower current density in the centre resulting in a lower deposition yield of Gd in this region [5]. The effect of the anode geometry was studied using a Solid platinum disc anode with 2 cm diameter. No improvement in the homogeneity of the obtained sample was observed, indicating that the geometry of the anode has no or very little effects on the homogeneity of the deposited layer.

To investigate the stirring effect, the solution was stirred during plating by means of ultrasonic stirrer (Fisher Scientific™ Model 120 Sonic Dismembrator with 3.1 mm diameter probe). To prevent overheating, it was operated at 30% power pulse (4-1s) mode. Maximum temperature of the solution was measured as 38 °C. Fig. 5 shows the 3D autoradiograph and the activity distribution for a Gd deposited sample obtained by stirring the solution.
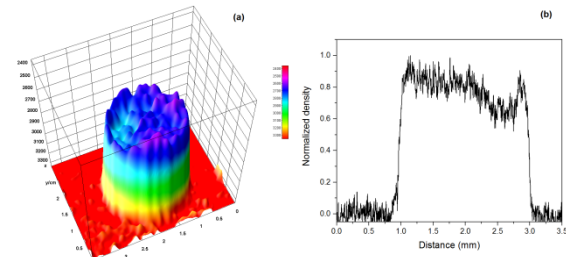
Fig. 4 : After molecular plating (with spiral anode and ultrasonic stirrer), RI 3D graph (a) and l [153]Gd activity distribution (b).

The homogeneity of the sample is remarkably improved by stirring the solution.

[1] Z. Talip, Ann Rep. Lab. of Radiochemistry (2016).
[2] S. Pomme et al., Acta Chim. Slov. **55**, 111, (2008).
[3] S. Pommé, Metrologia **52**, 146 (2015).
[4] Z. Talip et al., Anal Chem. **89**, 6861 (2017).
[5] Monzo, E., Genetti, V., Knight, K. Optimization of Uranium Molecular Deposition for Alpha-Counting Sources; Lawrence Livermore National Laboratory: Livermore, CA, 2016.

WASTE TREATMENT AND ISOTOPE RECLAMATION (WIR) PART I: THE TASK

M. Lin (Univ. Bern & PSI), I. Kajan, D. Schumann (PSI)

Currently, 700 g of spent nuclear fuel, dissolved in 30 L of 8-10 M HNO_3 are stored in the intermediate storage of the PSI Hotlaboratory. These solutions stem from analytical studies of samples from the Swiss nuclear power plants over a time span of several decades. For their disposal, these solutions need to be preconditioned so that they fulfil the requirements concerning solidification and follow-up chemical and physical stability of the waste package. Moreover, they contain scientifically interesting radionuclides which can hardly be produced by other means and represent valuable material for a certain number of experimental studies, for instance for nuclear astrophysics research. An at least partial radiochemical separation is necessary both for the conditioning task and the isolation of wanted isotopes.

In the frame of the project WIR (*W*aste treatment and *I*sotope *R*eclamation) we deal with these challenging tasks by developing dedicated and stepwise treatment procedures. The following sub-tasks have been identified:

- Separation of radio-elements inducing high dose rate
- Separation of α-emitters
- Systematic studies of of the chemical behaviour of radionuclides of interest in these separation systems
- Establishment of a general treatment procedure
-

The conditioning facility

For the final conditioning, the FIXBOX3, available in the PSI Hotlab, shall be used (Figure 1).

Fig. 1 : Photo of FIXBOX3

Consisting of two shielded α-boxes, which are connected with steel cables, it is used to solidify all highly radioactive liquid waste in to concrete blocks, which could be send to a possible final disposal side. To produce those concrete blocks, special

requirements for the activity and fissile inventory as well as for acid and salt concentration of the used waste solutions have to be fulfilled to meet the requirements for the final disposal. The first α-box (concentrating box) is used to concentrate low-level radioactive waste solutions by distillation in vacuum (distillation reactor). The preconditioned waste solutions are directly conditioned with cement in a mixer situated in the seconded α-box (hardening box) were the slurry is filled in a steel cylinder. After hardening the so produced concrete blocks are transferred into intermediate storage at the hotlab until a waste container for final storage could be filled.

- Procedure steps in the FIXBOX-3:
- concentrate of dilute waste solutions in the distillation reactor
- preparation of FIXBOX-3 preconditioned waste solutions
- analysis of preconditioned waste solutions mixing with cement
- hardening process
- intermediate storage of the hardened concrete blocks
-

The developed separation procedure

The main components present in the spent nuclear fuel solutions are long-lived fission products (e.g. [137]Cs and lanthanides), U, Pu and minor actinides. The Cs and to a certain extent also Eu isotopes are the main γ-dose producer. Therefore, at least Cs shall be separated first for easier handling. Elaborated procedures like evaporation, dilution etc. shall be avoided to keep the process as simple as possible. In Figure 2, the general treatment plan is shown.
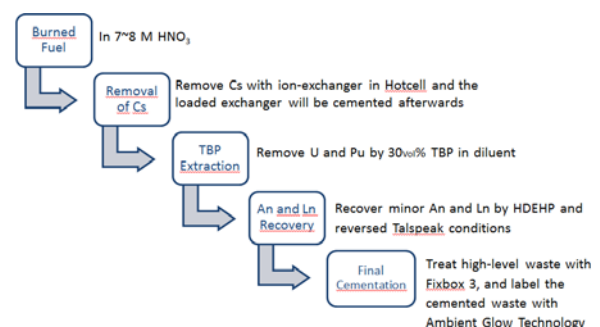
Fig. 2: Flow scheme of the waste conditioning.

It is favourable to remove Cs by ion exchange during the initial step using adsorbents standing the high nitric acid concentrations and still showing high absorption coefficients. In order to achieve this, several ion-exchanger were tested. High selectivity, fast kinetics and inertness of ion exchanger matrix towards acidity

and radiolysis is desired. For details of the results see WIR – Part II of this report.

After the Cs removal, extraction of U and Pu from the solutions will be performed by either solvent extraction or ion exchange methods (for results see WIR – Part III of this report).

Outlook

To utilize the gathered knowledge a pilot scale separation facility has to be built up where all the procedures will be tested with diluted samples of the waste solution. Based on decontamination factors obtained from these test experiments, the system can be optimized and installed within the hot-cell in AHL for hot tests and consequent final chemical treatment of fuel waste solutions. Methods for a partial separation and purification of scientifically interesting isotopes will be developed and implemented into the waste stream, where possible. These isotopes can be made available for half-life re-measurements as well as possible target preparations for n-TOF CERN. We start with ^{93}Mo as an example.

WASTE TREATMENT AND ISOTOPE RECLAMATION (WIR)
PART II: Cs REMOVAL BY ION EXCHANGE

M. Lin (Univ. Bern & PSI), I. Kajan, D. Schumann (PSI), A. Türler (Univ. Bern)

One of the main dose rate producers in spent nuclear fuel solution are the fission products ^{137}Cs and ^{134}Cs. According to the general separation scheme, shown in part I of this report, three ion-exchangers, Cs-treat® (hexacyanoferrate granules), AMP (ammonium molybdophosphate) and CLEVASOL®, were selected and tested concerning their capability to selectively remove Cs from high-acidic solution in the first separation step. Although Cs-treat® was successfully applied in Fukushima Daiichi NNP to remove Cs [1], it failed in our case due to its poor acidity stability. Thus only AMP and CLEVASOL were further investigated in terms of distribution coefficient and selectivity.

AMP has been described having Keggin structure and being able to form insoluble salts with large alkali metal ions in acidic solution [2-4] by partially exchanging ammonium [5-6]. In addition, some researchers have proved its stability against radiation [7] which makes it prospective for the usage to remove radioactive Cs from solution.

CLEVASOL is a novel ion-exchanger invented by Adphine company. Pre-tests have shown its high selectivity and adsorption capacity to Cs and radiation stability [8], which indicates its potential application in our case.

Experimental

Tracer amounts of Cs and other elements (Eu, Zr, U, Pu, Pd, Ag and Sr) dissolved in 10 ml HNO$_3$ of different concentrations, were contacted with 40-50 mg of ion exchanger in 20 ml plastic vials which were shaked in a water bath for 24 hours with 200 rpm at room temperature. Afterwards 1 ml of centrifuged and filtered solution was taken and measured by Inductively-Coupled Plasma-Mass-Spectrometry (ICP-MS) and γ-spectrometry (Eu and Cs in the experiment of AMP were measured by this technique).

The distribution coefficients of elements were calculated using the following equation :

$$K_d = \frac{C_{blank} - C_{sample}}{C_{sample}} \times \frac{V(ml)}{M(g)}$$

C_{blank} : Concentration of the element before contacting with ion-exchanger.

C_{sample} : Concentration of the element after contacting with ion-exchanger.

V : Volume of the solution (ml).

M : Mass of the ion-exchanger (g).

Results and discussion

Both AMP and CLEVASOL show good adsorption properties toward Cs and Eu in diluted HNO$_3$ as shown in figure 1. However, at higher HNO$_3$ concentrations, the distribution coefficients for both Eu and Cs drop drastically in the case of CLEVASOL, whereas Cs shows still high absorption on AMP.

The absorption properties of other important elements on AMP and CLEAVASOL, in particular U and Pu, are shown in figures 2 and 3.
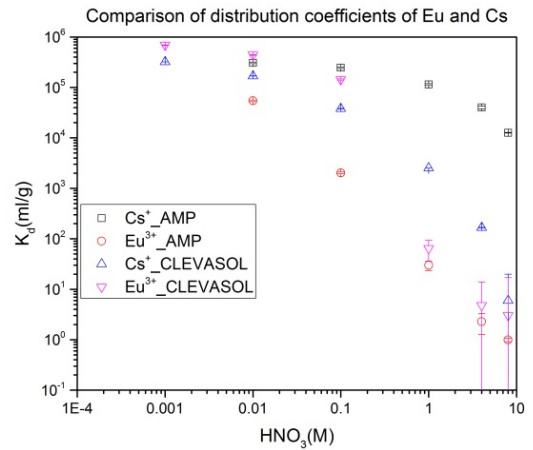
Fig. 1: Distribution coefficients of Eu and Cs on AMP and CLEVASOL.
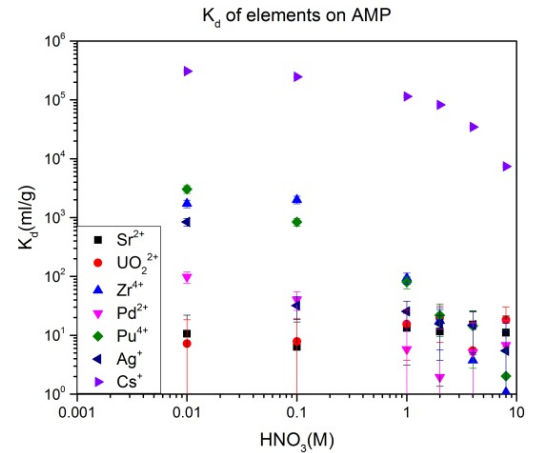
Fig. 2: Distribution coefficients of different elements on AMP.

With exception of Cs, all studied elements show rather modest or low absorption on AMP at higher HNO$_3$ concentrations.

Apart from Cs, CLEVASOL also adsorbs high amounts of other cations (Sr, U, Zr, Pd, Pu and Ag) in diluted HNO$_3$. The adsorption of Pd and Ag remains extremely high even in 4 and 8 M HNO$_3$ where Cs and other cations are only weakly adsorbed.
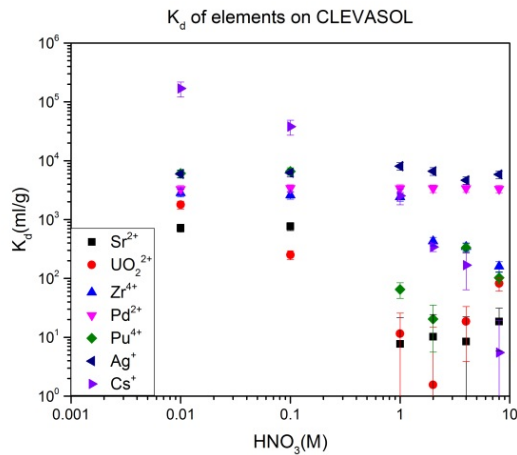
Fig. 3: Distribution coefficients of different elements on CLEVASOL.

Conclusions

AMP shows high selectivity for Cs in highly acidic nitric solutions and is, therefore, best suited for the envisaged task to lower the dose rate in the first step of treatment. The big advantage of the method is, that the initial solution (spent nuclear fuel in 8 M HNO_3) can be purified from Cs without any additional procedures than contacting it with AMP. Since AMP itself comprises a very fine powder, a feasibility study with a composit called AMP-PAN (a combination of AMP with Polyacrylnitrile polymer) is currently explored.

CLEVASOL favorably adsorbs Pd and Ag in a wide range of HNO_3 concentration, which indicates its potential usage to selectively remove these elements from high acidic spent nuclear fuel solutions.

_____

[1] Esko Tusa, ENC2014, European Nuclear Conference, Marseille, France, 11-14 May (2014).

[2] J. Van R. Smit, Nature (1958).

[3] R. W. C. Broadbank et al., J. Inorg. Nucl. Chem **23**, 311 (1961).

[4] J. Krtil, J. Inorg. Nucl. Chem **19**, 298 (1961).

[5] C. J. Coetzee et al., J. Inorg. Nucl. Chem **31**, 1711 (1970).

[6] C. J. Coetzee et al., J. Inorg. Nucl. Chem **33**, 1501 (1971).

[7] K. L. N. Rao et al., Radiat. Phys. Chem **49**, 85 (1997).

[8] Z. Dvorakova, PhD thesis, Tech. Univ. Munchen (2007).

WASTE TREATMENT AND ISOTOPE RECLAMATION (WIR)
PART III: EXTRACTION OF URANIUM AND PLUTONIUM

M. Lin (Univ. Bern & PSI), I. Kajan, D. Schumann (PSI)

The second step in the separation scheme for conditioning of spent nuclear fuel waste described in Part I is the removal of the matrix elements U and Pu. For this we apply the well-known and proven PUREX process in a slightly modified way using a battery of commercially available Mixer-Settler apparatus (MS). The method is based on liquid-liquid extraction using tributylphosphate (TBP) forming strong complexes with tetra and hexavalent actinides in suitable organic diluent directly from the nitric acid as aqueous phase. In Figure 1 the procedure is shown as a flow scheme. Kerosene and dodecane are two of the most used in the PUREX process [1-4]. In our experiments, 30 Vol% TBP in both diluents were tested to evaluate the distribution ratio of U and Pu.
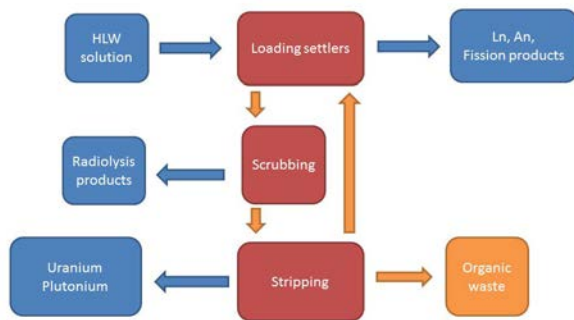
Fig. 1: Schematics of the solvent extraction facility for extraction of actinides and lanthanides from nuclear fuel solutions. Organic fraction is marked in orange, aqueous phases in blue.

Experimental

1 ml of organic phase was mixed with 1 ml of aqueous phase in glass vials. The organic phase contained 30Vol% TBP in diluent (kerosene or dodecane), and the aqueous phase contained tracer amounts of U and fission products in HNO_3 (4, 6 and 8 M respectively). 0.5 ml of the aqueous phase were taken for ICP-MS measurement prior to the experiment. The vials were then shaken with a shaking machine for 1 hour with 1000 rpm. Then, 0.5 ml of the aqueous solution were taken from each vial and individually measured by ICP-MS.

To study the influence of HNO_3 on the extraction system, in an additional series of experiments the TBP phase was pre-saturated with the same volume of HNO_3 solution having similar concentration to the radioactive solution (4, 6 and 8 M respectively). These samples were marked as STBP.

Pu extraction studies were performed in a similar way. After one hour shaking 100 μl of each phase were taken and respectively mixed with 15 ml of

scintillation cocktail in a 20 ml plastic vial for Liquid-Scintillation-Counting (LSC).

The distribution ratios of solutes was calculated by the equations as following :

$$D = \frac{c_{initial} - c_{aq}}{c_{aq}} \text{ in ICP-MS measurement}$$
$$D = \frac{c_{org}}{c_{aq}} \text{ in LSC measurement}$$

$c_{initial}$: Concentration of element in aqueous phase before shaking.

c_{aq} : Concentration of element in aqueous phase after shaking.

c_{org} : Concentration of element in organic phase after shaking.

Results and discussion
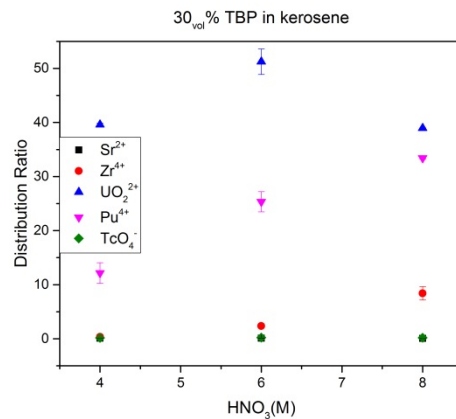
Fig. 2: Distribution ratios of U, Pu and fission products using 30_{Vol}% TBP in kerosene as extractant.
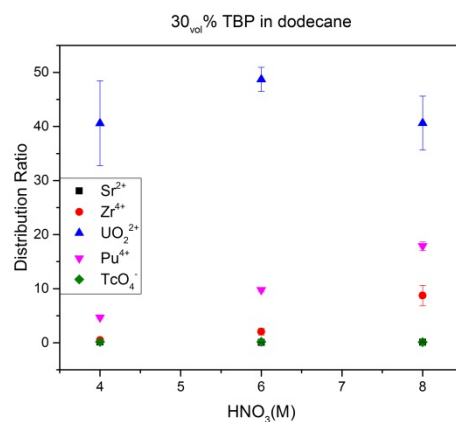
Fig. 3: Distribution ratios of U, Pu and fission products using 30_{Vol}% TBP in dodecane as extractant.

Fig. 4: Distribution ratios of U, Pu and fission products as 30_{Vol}% STBP in kerosene.
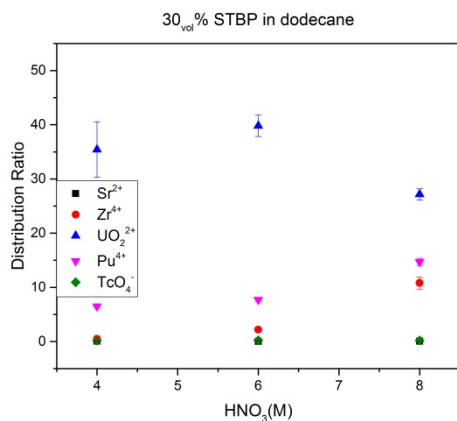
Fig. 5: Distribution ratios of U, Pu and fission products as 30_{Vol}% STBP in dodecane.

In the Figs 2-5 the extraction behaviour of U and Pu as well as Zr and Tc as examples for fission products is shown. Considering the envisaged goal – a selective separation of U and Pu from an 8 M HNO_3 solution with as few as possible separation steps – 30% TBP in kerosene is clearly the system of choise. Both U and Pu show still comparably high distribution ratios and and a clear separation from the fission products is achieved (Fig.2). If an isolation of U from Pu is envisaged, then dodecane can be used instead of kerosene (Fig.3). In both cases, the distribution ratios drop down if the organic phase is preequilibrated with HNO_3, due to its competing properties (Figs 4 and 5). Optimum conditions for the removal of U and Pu can be established using saturated 30%PTB in kerosene (Fig.4). U is completely separated from the aqueous solution and Pu to about 80%. To improve the Pu removal, the extraction has then to be repeated.

_____

[1] R. S. Herbst et al., Advanced Separation Techniques for Nuclear Fuel Reprocessing and Radioactive Waste Treatment, Chapter **6**, 142 (2011).

[2] G. Uchiyama et al., Progress in Nuclear Energy **37**, 151 (2000).

[3] Y. Marcus et al., J. Inorg. Nucl. Chem **38**, 1069 (1976).

[4] M. R. Chowdhury et al., Hydrometallurgy **34**, 319 (1994).

EXTENDING RADIOANALYTICAL CAPABILITIES AT LRC

J. Ulrich, R. Dressler, A. Vögele (PSI)

Multiple radiation detection techniques are used on daily basis at Laboratory of Radiochemistry (LRC), both as a convenient way of following radiolabeled chemical species through various chemical processes and for precise characterization of radioactive targets and materials, often containing exotic radionuclides.

Advice and support from experts within the laboratory is often needed to assure correct selection of suitable measurement and sample preparation methods to obtain optimal results for the answer sought. The challenges are particularly high due to high complexity and always changing, non-routine nature of the measurement tasks given by working in research.

With over 7500 measurements per year, the most commonly used radiation detection method in LRC is gamma-ray spectrometry which can be used for qualitative and quantitative analysis of most radionuclides. An inventory of seventeen stationary and portable HPGe detectors is available, eleven of them in permanent operation. In dependence of the measured sample, suitable crystal geometry (coaxial, planar, well) for optimized measurement performance For the best possible accuracy of measurement results, the calibration sources need to be as similar to the real sample in terms of container, matrix and positioning as possible. This is especially important for close-up geometries which are often needed due to the low activities of the samples.

For this reason, custom-made calibration sources are prepared from certified radionuclide solutions obtained from metrology institutes (czech CMI, german PTB) or commercial suppliers parties (Eckert & Ziegler). Short-lived radioisotopes can be produced at SINQ and after dissolving the start material, the solutions are characterized by comparison with certified calibration sources. The requested source geometries range from point-like sources over different plastic and glass vessels with specific matrix according to versatile needs to mercury or lead filled steel vessels. For the best results, the same radionuclides and containers are used like for the real samples. If these isotopes are unavailable, multi gamma-line emitters like Eu-152 can be utilized for distances larger than ca. 15 cm. For close-up geometries, well detectors or marinelli beakers, true coincidence summing (TCS) becomes non-negligible and special multinuclide mix solutions suitable for TCS-free calibration must be used which are available at LRC.

In case of preliminary studies or if less precision is satisfactory, numerical methods can be used. Two Canberra Broad Energy HPGe detectors with an ISOCS characterization and the corresponding efficiency calculation software are used in the laboratory, enabling modelling of common geometries with low to medium complexity but arbitrary structural and matrix material. In addition, a detailed technical drawing of one of the BEGe detectors is available which enables the modelling of very complex geometries with high precision using specialist-grade Monte Carlo codes like MCNP and GEANT4. These are both utilized for various simulation tasks besides efficiency calibration within the laboratory as well. Fig. 1 shows the used detector model and calculated full energy peak (FEP) efficiency curve.
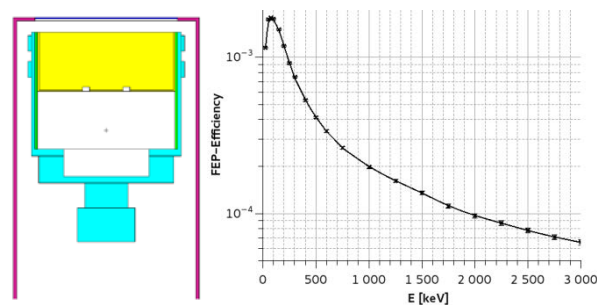
Fig. 1: Cut through MCNP model of a Canberra BEGe-Type detector including exact dimensions on germanium crystal, the endcap and the crystal holder (left), MCNP-calculated FEP efficiency curve for a point-like source in aluminum sample holder in 33 cm distance (right).

The demands for tailor-made calibration standards and utilization of nuclear simulation will probably stay high in next year. As a contamination-prone variant to enclosing liquid radionuclide solutions in the vessels, preparation of sealed sources, with the radionuclide solution dispensed in a solidified polymer matrix should be investigated. Introduction of a Quality Assurance (QA) to monitor the long-tem performance of the gamma detectors would be advantageous in environment with high amount of relatively fast changing personnel (Ph.D.s and PostDocs).

Liquid Scintillation Counting (LSC) is the method of choice for low-energy or no-gamma emitting radionuclides. It exhibits very high detection efficiency (up to nearly 100 %) for charged particle emitters (alpha, beta or EC emitter). With a proper calibration, time-resolved LSC (TR-LSC) can separate alpha-particles from electrons by pulse shape analysis. LSC is used as well for low resolution alpha spectroscopy with the advantage of simple to no sample preparation in comparison to classical alpha spectroscopy. Two Packard TriCarb devices are used in LRC, one of them with sample cooler and alpha-beta discrimination capability. In addition, two PERALS detectors are available at LRC which are

optimized for alpha spectrometry. The yearly LSC sample count is around 1500.

LSC-based radionuclide standardization techniques CIEMAT/NIST and TDCR [1] (with the Hidex 300SL detector of the ASI department) were adopted for usage at LRC in 2017, using GEANT4 and in-house software to calculate the corresponding detection efficiency curves.

Both methods were tested for absolute activity determination with model nuclides and could be successfully applied for creating and checking calibrations of various medically interesting radionuclides (e.g. Tb-161, Er-165) used at the Center of Radiopharmaceutical Sciences, PSI. The overall LSC expertise will grow further because of the envisioned active usage of LSC in multiple research projects in 2018, especially exploiting the alpha/beta separation capabilities. The same applies to the competence in the CIEMAT/NIST standardization method due to more and thorough tests and software improvements. Fig. 2 presents the calculated efficiency for Tb-161 and Er-165 as function of TDCR (triple-to-double coincidence ratio).
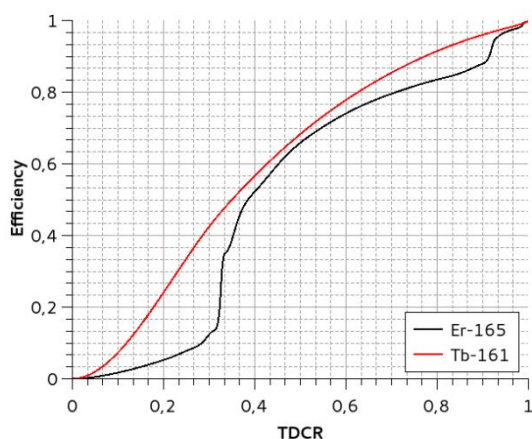

Fig. 2: Calculated efficiency vs. TDCR curves for Tb-161 and Er-165. Tb-161 is beta emitter with some contribution of low-energy gamma-rays and Er-165 is electron capture decaying radionuclide with multiple energy groups of Auger electrons and X-rays.

Alpha spectroscopy, performed with solid state detectors, is regularly used for qualitative or quantitatve analysis of alpha emitting radionuclides. Special care must be taken to the sample preparation because the quality of the obtained spectra in terms of resolution is dominated by self-absorption processes in the deposited sample material. In case of highly diluted solution a simple reduction to dryness of an aliquote is sufficient. In our laboratory molecular plating is the common used method to prepare high-quality alpha samples. Fig. 3 shows an example of alpha spectroscopy sample prepared by molecular plating and the resulting, measured alpha spectrum.

There are up to 24 alpha counting devices available either as 2π- or 4π-standalone devices or as an Integrated Alpha Spectrometer (Alpha Analyst Mirion Technologies Canberra). All of these devices are equipped with Passivated Implanted Planar Silicon detectors (PIPS) of various sizes. In total up to 2000 alpha samples are measured per year.
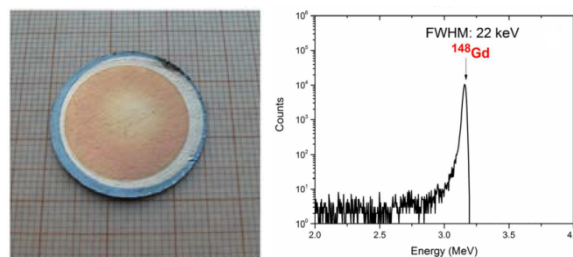
Fig. 3: Gd-148 sample for alpha spectroscopy, prepared by molecular plating (left) and the alpha spectrum measured with this sample, showing achieved peak width (right) [2].

Alpha spectroscopy is not only used for radio-analytical investigations, but also to characterize sample and deposition thicknesses by measuring the energy loss of emitted alpha-particles passing through matter layers [3]. For the analysis of these measurements the Advanced Alpha-spectroscopy SImulation program (AASI) [4,5] is used which simulates the transport of alpha particles through material by Monte Carlo method.

In addition to the standard nuclear measurement electronics homemade detection systems using silicon- or diamond-based sensors were developed to investigate chemical properties of super heavy elements [6-9].

_____

[1] R. Broda et al., Metrologia **44**, S36 (2007).
[2] Z. Talip et al., Anal. Chem. **89**, 13541 (2017).
[3] E.A. Maugeri et al., J. Instr. **12**, (2017).
[4] T. Siiskonen, R. Pöllänen, Nucl. Instrum. Methods **A 550**, 425 (2005).
[5] T. Siiskonen, R. Pöllänen, Nucl. Instr. Meth. **A 558**, 437 (2006).
[6] R. Eichler et al., Nature **447**, 72 (2007).
[7] R. Eichler et al., Angew. Chem. **47**, 3262 (2008).
[8] P. Steinegger et al., J. Phys. Chem. **C 120**, 7122, (2016).
[9] P. Steinegger et al., Nucl. Instr. Methods **A 850**, 61 (2016).

PRODUCTION AND SEPARATION OF ^{165}Er – A MEDICALLY INTERESTING AUGER EMITTER

N. Gracheva (ETHZ & PSI/CRS), S. Heinitz (PSI), R. Schibli (ETHZ & PSI/CRS), N.P. van der Meulen (PSI)

In the last decade, great interest has been shown with regard to the application of Auger emitters for cancer treatment. Compared to energetic electrons, Auger electrons have higher linear energy transfer (LET): ~0.2 keV/µm for high-energy and ~26 keV/µm for low-energy electrons, respectively [1]. This means that Auger emitters deposit energy locally over a short range (nm-µm scale) and, when located in the cell nucleus, shows extreme radiotoxicity resulting in DNA breakage [2]. An interesting Auger-electron emitter is ^{165}Er, which has a half-life of 10.3 h and decays by electron capture and emission of Auger electrons, without accompanying gamma irradiation. This is a favorable trait, in order to prevent exposure of patients with high doses, making the radionuclide attractive for targeted radionuclide therapy [3]. Several production routes to obtain ^{165}Er were proposed in literature, including ^{165}Ho(p,n)^{165}Er, ^{166}Er(p,2n)^{165}Tm→^{165}Er, ^{164}Er(d,n)^{165}Tm → ^{165}Er: reactions and reaction cross-sections were calculated by ALICE/91, ALICE/ASH and TALYS-1.2 codes [4]. However, no experimental data have been published yet with regards to the production and purification of ^{165}Er. Based on the reaction cross-sections and availability of target material, ^{165}Ho(p,n)^{165}Er and ^{166}Er(p,2n)^{165}Tm→^{165}Er production routes were chosen for the comparison within the scope of the project. We primarily focused on the ^{165}Ho(p,n)^{165}Er reaction, as holmium is monoisotopic with only one stable isotope ^{165}Ho, meaning availability and low price of the target material. Another attractive side of this production route is the optimal proton beam energy range (7-16 MeV) which allows the use of commercial medical cyclotrons.

Irradiation: ^{165}Ho targets were prepared by placing 200 mg ^{165}Ho$_2$O$_3$ into a target pellet of 0.3 mm thickness and 13 mm in diameter. The irradiation was performed with around 9, 11 and 13 MeV protons at 20 µA beam current for 8 hours. **Purification:** After irradiation, the target material was dissolved in 2 mL 2M HNO$_3$. ^{165}Er separation from the target material was performed by means of cation exchange chromatography with the use of α-hydroxy-isobutyric acid (HIBA) as eluent. Concentration of ^{165}Er was performed using LN3 extraction resin, followed by elution of the final product in 1 mL 0.05M HCl. **Radiolabelling**: The isolated from the target material ^{165}Er was radiolabeled with PSMA-617.

The irradiaton of targets using the ^{165}Ho(p,n)^{165}Er production route resulted in a low ^{165}Er yield (Table 1). While higher proton-beam energies would improve the product yield, cross-contamination with stable ^{164}Er via the ^{165}Ho(p,2n)^{164}Er nuclear reaction may occur, based on theoretical calculations [4]. This disadvantage indicates the necessity of pursuing the ^{166}Er(p,2n)^{165}Tm→^{165}Er reaction towards large-scale ^{165}Er production.

Tab. 1: Characteristics of ^{165}Ho(p,n)^{165}Er production route

Mass of the ^{165}Ho$_2$O$_3$ target material, mg	Proton beam energy, MeV	^{165}Er activity at EOB, MBq
200	13	660
200	11	200
200	9	75

When determining a method of isolating ^{165}Er from the target material, the results showed that sufficient separation of Er from the neighboring lanthanides could be achieved (Fig.1). The separation yield to date is 70-80% and the separation process takes 10 hours.
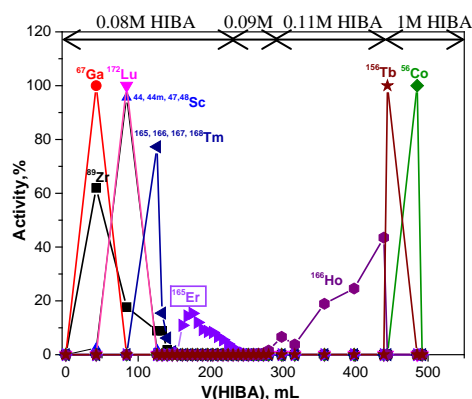
Fig. 1: Elution profile of Er separation from the target material and formed impurities

The formation of $^{165-168}$Tm isotopes indicates the content of stable Er isotopes in the target material and more likely in the final product (^{165}ErCl$_3$). By Cherenkov decay counting measurement of the final ^{165}ErCl$_3$ product, ^{171}Er was also detected. Labeling of PSMA-617 with the obtained ^{165}Er was performed. At 1 MBq/nmol labeling efficiency was only 6.9%, indicating the potential presence of other Er isotopes in the final product. As a result, we investigate a purification method for the initial ^{165}Ho$_2$O$_3$ target material. Thus, interferences from stable Er isotopes could be avoided the final product.

[1]   A. Kassis et al., Int J Radiat Biol **80,** 789 (2004).
[2]   R. Howell, Int J Radiat Biol **84,** 959 (2008).
[3]   D. Rao et al., Med Phys **4**, 177 (1977).
[4]   M. Sadeghi et al., J Mod Phys **1**, 217 (2010).

CaO TARGET DEVELOPMENT FOR ^{44}Sc PRODUCTION

R. Hasler, C. Vermeulen (PSI/CRS), N.P. van der Meulen (PSI)

INTRODUCTION

The production of ^{44}Sc radionuclides, used for Positron Emission Tomography (PET), is primarily conducted via the (p,n) nuclear reaction using ^{44}CaCO$_3$ as target material. Originally, the targets were prepared by placing 10 mg of enriched ^{44}CaCO$_3$ on top of 160 mg graphite powder (used as carrier matrix), loaded into a die and applying an axial pressure of 10 t. Resulting pellets have a diameter of 16 mm and a thickness between 0.4-0.5 mm. Such pellets were then encapsulated in an aluminum target capsule suitable for the target holder system of the IP2 irradiation facility at PSI (Fig. 1). [1]

Fig. 1: Pelletized target for ^{44}Sc production as prepared with graphite powder (*left*) and after encapsulation in the aluminum target capsule (*right*).

The use of this methodology makes it difficult to control the position, diameter and depth of the enriched target material, however. Such inhomogeneity translates in a heterogeneous irradiation which, consequently, causes large variations in the production yield of ^{44}Sc. Furthermore, the presence of graphite powder renders the separation process more difficult, as it can clog catheter lines in the chemical separation system.

EXPERIMENTAL

To overcome these issues, a target made of pure ^{44}Ca-target material, *sans* the graphite carrier matrix, was developed. In this case, 30 mg of ^{44}Ca-target material was consolidated into a disk-shaped pellet 6 mm in diameter and 0.5 mm thick. Resulting pellets were then encapsulated in aluminum target capsules (Fig. 2). This target design presents a simpler, more homogeneous, robust, and reliable system providing a reproducible and standardized method for the target preparation.

Fig. 2: Representative picture of a 6 mm pellet target made of 30 mg CaO as prepared (*left*) and after encapsulation in the aluminum target capsule (*right*).

RESULTS AND DISCUSSION

The first targets prepared using this procedure consisted of natural CaCO$_3$. Under the applied irradiation conditions (~11 MeV, 50 µA), however, release of CO$_2$ occurred and led to distortion of the target capsule. To avoid the CO$_2$ production during irradiation, CaCO$_3$ was annealed at 900 °C to ensure its thermal decomposition. X-ray diffraction (XRD) analysis of the obtained powder shows a complete conversion of CaCO$_3$ (Calcite, rhombohedral crystal structure, S.G.: *R-3c*) to CaO (cubic crystal structure, S.G.: *Fm3m*) (Fig. 3).
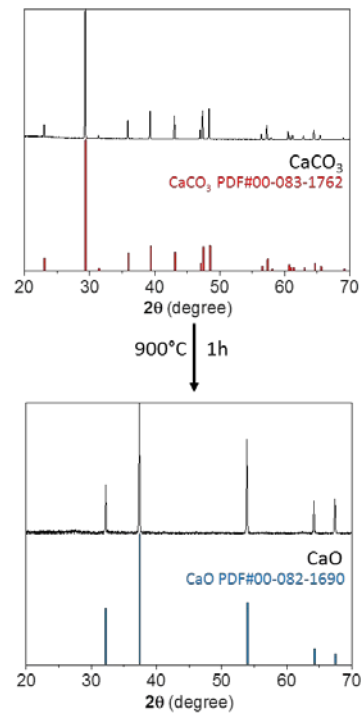
Fig. 3: X-ray diffraction patterns obtained from as purchased CaCO$_3$ (*above*) and CaO, obtained after thermal decomposition (*below*).

The 6 mm CaO targets were tested under various irradiation conditions, with promising and reproducible results. The irradiated targets could be dissolved and separated using the same conditions as currently used for the routine production of ^{44}Sc at PSI. This facilitates the implementation of the new target into the work flow of the currently-used method for ^{44}Sc production here at PSI.

[1] N. P. van der Meulen et al., Nucl. Med. Biol. 42 (2015).

IRRADIATION TESTS ON QUIREMSPHERES TO PRODUCE ^{166}Ho FOR RADIATION THERAPY

A. Vögele, N.P. van der Meulen, R. Eichler (PSI), M. Synowiecki (RTM, Nijmegen)
J.F.W. Nijsen (Quirem Medical BV, Radboudumc Nijmegen, The Netherlands)

INTRODUCTION

A relatively new technology for cancer therapy involves the use of ^{166}Ho (β^--radiation emitter, $T_{1/2}$ = 26.8 h) packed in poly(L-lactic acid) microspheres ^{166}Ho-MS) for the treatment of patients suffering from liver cancer – known as Selective Internal Radiation Therapy – a therapy actively pursued in the Netherlands [1]. The concept involves neutron irradiation of microspheres containing a certain percentage of Ho to produce the desired ^{166}Ho. The γ-emission from ^{166}Ho also allows the patient to be imaged using Single Photon Emission Computed Tomography (SPECT). The use of the micropheres in a patient also has the advantage of being used in Magnetic Resonance Imaging, as the microspheres are also highly paramagnetic.

As the therapy is gaining popularity, the demand for ^{166}Ho-MS is expected to grow. The current manufacturing method of using nuclear research reactors is relatively expensive and a network of reactors is needed to meet the production capacity. As a result, alternate means of producing the radionuclide is being investigated.

EXPERIMENTAL

Two containers containing ^{166}Ho-MS "Quirem-Spheres" were encapsulated (Fig. 1) and irradiated at PNA using the neutron spallation source at PSI (SINQ-NIS), the first for a period of 36 min (to a calculated yield of 10 GBq ^{166}Ho) and the second for 70 min (to a calculated yield of 20 GBq ^{166}Ho). The second container also contained temperature labels to determine the temperature of the spheres during the irradiation process. The irradiation parameters are summarized in Table 1.

Fig. 1: ^{166}Ho-MS prepared for irradiation.

Tab. 1: Irradiation parameters form PNA-logging

N	time	p-beam mA	n_{therm}-integral	T_{max} °C Transport pipe	T_{ave} °C Transport pipe
1	36 min	1	5.38E16	83 °C	68 °C
2	70 min	1	1.08E17	83 °C	68 °C

RESULTS AND DISCUSSION

Two test irradiations were performed in PNA using holmium microspheres, with the aim of obtaining 10 GBq (at 5.38e16 thermal n^0/cm^2) and 20 GBq (1.08e17 thermal n^0/cm^2) ^{166}Ho, respectively. While it was determined that the microscopic quality of the spheres were very good and the quality control thereof were within specifications, the yield of the radionuclide of both samples was determined to be 20% lower than calculated.
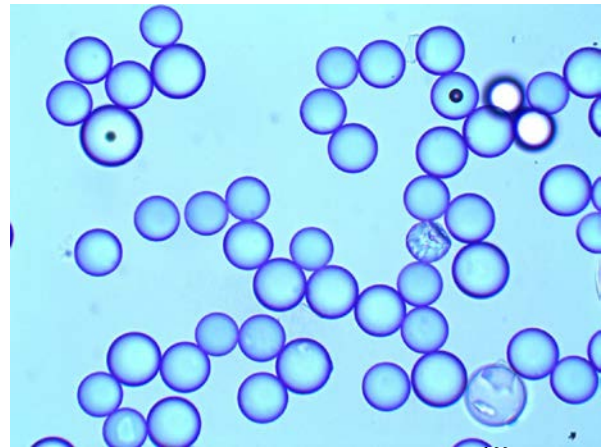
Fig. 2: 400x magnification of the irradiated ^{166}Ho-MS.

It was determined that the temperature of the spheres reached between 71 and 77 °C during the irradiation process, where the ideal temperature is regarded to be 50 to 55 °C. As a result, the macroscopic quality of the spheres did not meet the predetermined quality specifications. It is thought that the aggregates in the product may have two causes, namely, too high γ-heating and/or too high temperature in the material. Often the damage of the material is a combination of these two variables. Therefore, the activation environment must be further optimized and investigated.

[1] M.L.J. Smits et al., J Nucl Med. 54:2093 (2013).

LIST OF PUBLICATIONS

N. V. Aksenov, P. Steinegger, F. Sh. Abdullin, Y. V. Albin, G. A. Bozhikov, V. I. Chepigin, R. Eichler, V. Ya. Lebedev, A. Sh. Madumarov, O. N. Malyshev, O. V. Petrushkin, A. N. Polyakov, Y. A. Popov, A. V. Sabel'nikov, R. N. Sagaidak, I. V. Shirokovsky, M. V. Shumeiko, G. Ya. Starodub, Y. S. Tsyganov, V. K. Utyonkov, A. A. Voinov, G. K. Vostokin, A. V. Yeremin, S. N. Dmitriev
On the volatility of nihonium (Nh, Z = 113)
Eur. Phys. J. A **53**, 158 (2017), DOI: 10.1140/epja/i2017-12348-8

J. Balibrea-Correa, E. Mendoza, D. Cano-Ott, M. Krtička, S. Altstadt, J. Andrzejewski, L. Audouin, V. Bécares, M. Barbagallo, F. Bečvář, F. Belloni, E. Berthoumieux, J. Billowes, V. Boccone, D. Bosnar, M. Brugger, F. Calviño, M. Calviani, C. Carrapiço, F. Cerutti, E. Chiaveri, M. Chin, N. Colonna, G. Cortés, M.A. Cortés-Giraldo, M. Diakaki, C. Domingo-Pardo, R. Dressler, I. Durán, C. Eleftheriadis, A. Ferrari, K. Fraval, V. Furman, K. Göbel, C. Guerrero, M.B. Gómez-Hornillos, S. Ganesan, A.R. García, G. Giubrone, I.F. Gonçalves, E. González, A. Goverdovski, E. Griesmayer, F. Gunsing, T. Heftrich, S. Heinitz, A. Hernández-Prieto, J. Heyse, D.G. Jenkins, E. Jericha, F. Käppeler, Y. Kadi, D. Karadimos, T. Katabuchi, V. Ketlerov, V. Khryachkov, N. Kivel, P. Koehler, M. Kokkoris, J. Kroll, C. Lampoudis, C. Langer, E. Leal-Cidoncha, C. Lederer, H. Leeb, L.S. Leong, J. Lerendegui-Marco, M. Licata, R. Losito, A. Mallick, A. Manousos, J. Marganiec, T. Martínez, C. Massimi, P. Mastinu, M. Mastromarco, A. Mengoni, P.M. Milazzo, F. Mingrone, M. Mirea, W. Mondelaers, C. Paradela, A. Pavlik, J. Perkowski, A.J.M. Plompen, J. Praena, J.M. Quesada, T. Rauscher, R. Reifarth, A. Riego-Perez, M. Robles, C. Rubbia, J.A. Ryan, M. Sabaté-Gilarte, R. Sarmento, A. Saxena, P. Schillebeeckx, S. Schmidt, D. Schumann, P. Sedyshev, G. Tagliente, J.L. Tain, A. Tarifeño-Saldivia, D. Tarrío, L. Tassan-Got, A. Tsinganis, S. Valenta, G. Vannini, V. Variale, P. Vaz, A. Ventura, M.J. Vermeulen, V. Vlachoudis, R. Vlastou, A. Wallner, T. Ware, M. Weigand, C. Weiss, T. Wright, P. Žugec and the n_TOF Collaboration
Measurement of the neutron capture cross section of the fissile isotope U-235 with the CERN n_TOF total absorption calorimeter and a fission tagging based on micromegas detectors
EPJ Web of Conferences **146**, 11021 (2017), DOI: 10.1051/epjconf/201714611021

M. Barbagallo, N. Colonna, O. Aberle, J. Andrzejewski, L. Audouin, V. Bécares, M. Bacak, J. Balibrea, S. Barros, F. Bečvář, C. Beinrucker, E. Berthoumieux, J. Billowes, D. Bosnar, M. Brugger, M. Caamaño, F. Calviño, M. Calviani, D. Cano-Ott, R. Cardella, A. Casanovas, D.M. Castelluccio, F. Cerutti, Y.H. Chen, E. Chiaveri, G. Cortés, M.A. Cortés-Giraldo, L. Cosentino, L.A. Damone, M. Diakaki, C. Domingo-Pardo, R. Dressler, E. Dupont, I. Durán, B. Fernández-Domínguez, A. Ferrari, P. Ferreira, P. Finocchiaro, V. Furman, K. Göbel, A.R. García, A. Gawlik, T. Glodariu, I.F. Gonçalves, E. González, A. Goverdovski, E. Griesmayer, C. Guerrero, F. Gunsing, H. Harada, T. Heftrich, S. Heinitz, J. Heyse, D.G. Jenkins, E. Jericha, F. Käppeler, Y. Kadi, T. Katabuchi, P. Kavrigin, V. Ketlerov, V. Khryachkov, A. Kimura, N. Kivel, M. Kokkoris, M. Krtička, E. Leal-Cidoncha, C. Lederer, H. Leeb, J. Lerendegui-Marco, S. Lo Meo, S.J. Lonsdale, R. Losito, D. Macina, J. Marganiec, T. Martínez, C. Massimi, P. Mastinu, M. Mastromarco, F. Matteucci, E.A. Maugeri et al.
$^7Be(n,\alpha)$ and $^7Be(n,p)$ cross-section measurement for the cosmological lithium problem at the n_TOF facility at CERN
EPJ Web of Conferences **146**, 01012 (2017), DOI: 10.1051/epjconf/201714601012

R. Baum, A. Singh, M. Benesova, C. Vermeulen, S. Gnesin, U. Koester, K. Johnston, D. Mueller, S. Senftleben, H. Kulkarni, A. Türler, R. Schibli, J. Prior, N. van der Meulen, C. Müller
Clinical evaluation of the radiolanthanide terbium-152: First-in-human PET/CT with ^{152}Tb-DOTATOC
Dalton Trans. **46**, 14638 (2017), DOI: 10.1039/c7dt01936j

T. S. Carzaniga, M. Auger, S. Braccini, M. Bunka, A. Ereditato, K. P. Nesteruk, P. Scampoli, A. Türler, N. P. van der Meulen
Measurement of ^{43}Sc and ^{44}Sc production cross-section with an 18 MeV medical PET cyclotron
Appl. Radiat. Isot. **129**, 96 (2017), DOI: 10.1016/j.apradiso.2017.08.013

Y.H. Chen, L. Tassan-Got, L. Audouin, C. Le Naour, I. Durán, E. Casarejos, O. Aberle, J. Andrzejewski, V. Bécares, M. Bacak, J. Balibrea, M. Barbagallo, S. Barros, F. Bečvář, C. Beinrucker, E. Berthoumieux, J. Billowes, D. Bosnar, M. Brugger, M. Caamaño, F. Calviño, M. Calviani, D. Cano-Ott, R. Cardella, A. Casanovas, D.M. Castelluccio, F. Cerutti, E. Chiaveri, N. Colonna, G. Cortés, M.A. Cortés-Giraldo, L. Cosentino, L.A. Damone, M. Diakaki, C. Domingo-Pardo, R. Dressler, E. Dupont, B. Fernández-Domínguez, A. Ferrari, P. Ferreira, P. Finocchiaro, V. Furman, K. Göbel, M.B. Gómez-Hornillos, A.R. García, A. Gawlik, T. Glodariu, I.F. Gonçalves, E. González, A. Goverdovski, E. Griesmayer, C. Guerrero, F. Gunsing, H. Harada, T. Heftrich, S. Heinitz, J. Heyse, D.G. Jenkins, E. Jericha, F. Käppeler, Y. Kadi, T. Katabuchi, P. Kavrigin, V. Ketlerov, V. Khryachkov, A. Kimura, N. Kivel, M. Kokkoris, M. Krtička, E. Leal-Cidoncha, C. Lederer, H. Leeb, J. Lerendegui-Marco, S. Lo Meo, S.J. Lonsdale, R. Losito, D. Macina, J. Marganiec, T. Martínez, C. Massimi et al.
Characterization of the n_TOF EAR-2 neutron beam
EPJ Web of Conferences **146**, 03020 (2017), DOI: 10.1051/epjconf/201714603020

E. Chiaveri, O. Aberle, J. Andrzejewski, L. Audouin, M. Bacak, J. Balibrea, M. Barbagallo, F. Bečvář, E. Berthoumieux, J. Billowes, D. Bosnar, A. Brown, M. Caamaño, F. Calviño, M. Calviani, D. Cano-Ott, R. Cardella, A. Casanovas, F. Cerutti, Y.H. Chen, N. Colonna, G. Cortés, M.A. Cortés-Giraldo, L. Cosentino, L.A. Damone, M. Diakaki, C. Domingo-Pardo, R. Dressler, E. Dupont, I. Durán, B. Fernández-Domínguez, A. Ferrari, P. Ferreira, P. Finocchiaro, K. Göbel, A.R. García, A. Gawlik, S. Gilardoni, T. Glodariu, I.F. Gonçalves, E. González, E. Griesmayer, C. Guerrero, F. Gunsing, H. Harada, S. Heinitz, J. Heyse, D.G. Jenkins, E. Jericha, F. Käppeler, Y. Kadi, A. Kalamara, P. Kavrigin, A. Kimura, N. Kivel, M. Kokkoris, M. Krtička, D. Kurtulgil, E. Leal-Cidoncha, C. Lederer, H. Leeb, J. Lerendegui-Marco, S. Lo Meo, S.J. Lonsdale, D. Macina, J. Marganiec, T. Martínez, A. Masi, C. Massimi, P. Mastinu, M. Mastromarco, E.A. Maugeri, A. Mazzone, E. Mendoza, A. Mengoni, P.M. Milazzo, F. Mingrone, A. Musumarra, A. Negret, R. Nolte et al.
The n_TOF facility: Neutron beams for challenging future measurements at CERN
EPJ Web of Conferences **146**, 03001 (2017), DOI: 10.1051/epjconf/201714603001

N. M. Chiera, N. V. Aksenov, Y. V. Albin, G. A. Bozhikov, V. I. Chepigin, S. N. Dmitriev, R. Dressler, R. Eichler, V. Ya. Lebedev, A. Madumarov, O. N. Malyshev, D. Piguet, Y. A. Popov, A. V. Sabelnikov, P. Steinegger, A. I. Svirikhin, A. Türler, K. Vostokin, A. Vögele, A. V. Yeremin
Interaction of elemental mercury with selenium surfaces: model experiments for investigations of superheavy elements copernicium and flerovium
J. Radioanal. Nucl. Chem. **311**, 99 (2017), DOI:10.1007/s10967-016-5018-8

S. G. Dolley, G. F. Steyn, T. J. van Rooyen, F. Szelecsényi, Z. Kovács, C. Vermeulen, N. P. van der Meulen
Concurrent spectrometry of annihilation radiation and characteristic gamma-rays for activity assessment of selected positron emitters
Appl. Radiat. Isot. **129**, 76 (2017), DOI: 10.1016/j.apradiso.2017.07.057

K. A. Domnanich, C. Müller, M. Benešová, R. Dressler, S. Haller, U. Köster, B. Ponsard, R. Schibli, A. Türler, N. P. van der Meulen
^{47}Sc as useful β⁻-emitter for the radiotheragnostic paradigm: a comparative study of feasible production routes
EJNMMI Radiopharmacy and Chemistry **2**, 5 (2017), DOI: 10.1186/S41181-017-0024-X

K. A. Domnanich, R. Eichler, C. Müller, S. Jordi, V. Yakusheva, S. Braccini, M. Behe, R. Schibli, A. Türler, N. P. van der Meulen
Production and separation of ^{43}Sc for radiopharmaceutical purposes
EJNMMI Radiopharmacy and Chemistry **2**, 14 (2017), DOI: 10.1186/s41181-017-0033-9

E. Dupont, N. Otuka, O. Cabellos, O. Aberle, G. Aerts, S. Altstadt, H. Alvarez, F. Alvarez-Velarde, S. Andriamonje, J. Andrzejewski, L. Audouin, M. Bacak, G. Badurek, J. Balibrea, M. Barbagallo, S. Barros, P. Baumann, V. Bécares, F. Bečvář, C. Beinrucker, F. Belloni, B. Berthier, E. Berthoumieux, J. Billowes, V. Boccone, D. Bosnar, A. Brown, M. Brugger, M. Caamaño, M. Calviani, F. Calviño, D. Cano-Ott, R. Capote, R. Cardella, C. Carrapiço, A. Casanovas, D.M. Castelluccio, P. Cennini, F. Cerutti, Y.H. Chen, E. Chiaveri, M. Chin, N. Colonna, G. Cortés, M.A. Cortés-Giraldo, L. Cosentino, A. Couture, J. Cox, L.A. Damone, S. David, K. Deo, M. Diakaki, I. Dillmann, C. Domingo-Pardo, R. Dressler, W. Dridi, I. Duran, C. Eleftheriadis, M. Embid-Segura, B. Fernández-Domínguez, L. Ferrant, A. Ferrari, P. Ferreira, P. Finocchiaro, K. Fraval, R.J.W. Frost, R. Fujii, W. Furman, S. Ganesan, A.R. Garcia, A. Gawlik, I. Gheorghe, S. Gilardoni, G. Giubrone, T. Glodariu, K. Göbel, M.B. Gomez-Hornillos, I.F. Goncalves, E. Gonzalez-Romero, A. Goverdovski et al.
Dissemination of data measured at the CERN n_TOF facility
EPJ Web of Conferences **146**, 07002 (2017), DOI: 10.1051/epjconf/201714607002

R. Eichler
Superheavy Element Chemistry—New Experimental Results Challenge Theoretical Understanding
New Horizons in Fundamental Physics, FIAS Interdisciplinary Science Series, S. Schramm and M. Schäfer (eds.), Springer International Publishing Switzerland 2017, DOI: 10.1007/978-3-319-44165-8_4

A. Giachero, B.K. Alpert, D.T. Becker, D.A. Bennett, M. Biasotti, C. Brofferio, V. Ceriale, G. Ceruti, D. Corsini, P.K. Day, M. De Gerone, R. Dressler, M. Faverzani, E. Ferri, J.W. Fowler, E. Fumagalli, G. Gallucci, J.D. Gard, F. Gatti, J.P. Hays-Wehle, S. Heinitz, G.C. Hilton, U. Köster, M. Lusignoli, J.A.B. Mates, S. Nisi, A. Nucciotti, A. Orlando, L. Parodi, G. Pessina, G. Pizzigoni, A. Puiu, S. Ragazzi, C.D. Reintsema, M. Ribeiro Gomes, D. R. Schmidt, D. Schumann, F. Siccardi, M. Sisti, D.S. Swetz, F. Terranova, J.N. Ullom, L.R. Vale
Measuring the electron neutrino mass with improved sensitivity: the HOLMES experiment
J. Instr. **12**, C02046 (2017), DOI: 10.1088/1748-0221/12/02/C02046

C. Guerrero, C. Domingo-Pardo, J. Lerendegui-Marco, A. Casanovas, M. A. Cortes-Giraldo, R. Dressler, S. Halfon, S. Heinitz, N. Kivel, U. Köster, M. Paul, J. M. Quesada-Molina, D. Schumann, A. Tarifeño-Saldivia, M. Tessler, L. Weissman
Neutron Capture Cross Sections of the s-Process Branching Points [147] Pm, [171] Tm, and [204] Tl
JPS Conference Proceedings **14**, 010903 (2017), DOI: 10.7566/JPSCP.14.010903

C. Guerrero, J. Lerendegui-Marco, C. Domingo-Pardo, A. Casanovas, R. Dressler, S. Halfon, S. Heinitz, N. Kivel, U. Köster, M. Paul, J.M. Quesada-Molina, D. Schumann, A. Tarifeño-Saldivia, M. Tessler, L. Weissman, O. Aberle, J. Andrzejewski, L. Audouin, M. Bacak, J. Balibrea, M. Barbagallo, F. Becvar, E. Berthoumieux, J. Billowes, D. Bosnar, A. Brown, M. Caamaño, F. Calviño, M. Calviani, D. Cano-Ott, R. Cardella, F. Cerutti, Y.H. Chen, E. Chiaveri, N. Colonna, G. Cortés, M.A. Cortés-Giraldo, L. Cosentino, L.A. Damone, M. Diakaki, E. Dupont, I. Durán, B. Fernández-Domínguez, A. Ferrari, P. Ferreira, P. Finocchiaro, K. Göbel, A.R. García, A. Gawlik, S. Gilardoni, T. Glodariu, I.F. Gonçalves, E. González, E. Griesmayer, F. Gunsing, H. Harada, J. Heyse, D.G. Jenkins, E. Jericha, F. Käppeler, Y. Kadi, A. Kalamara, P. Kavrigin, A. Kimura, N. Kivel, M. Kokkoris, M. Krticka, D. Kurtulgil, E. Leal-Cidoncha, C. Lederer, H. Leeb, S. Lo Meo, S.J. Lonsdale, D. Macina, J. Marganiec, T. Martínez, A. Masi, C. Massimi, P. Mastinu, M. Mastromarco, E.A. Maugeri et al.
Time-of-flight and activation experiments on [147]Pm and [171]Tm for astrophysics
EPJ Web of Conferences **146**, 01007 (2017), DOI: 10.1051/epjconf/201714601007

F. Gunsing, O. Aberle, J. Andrzejewski, L. Audouin, V. Bécares, M. Bacak, J. Balibrea-Correa, M. Barbagallo, S. Barros, F. Bečvář, C. Beinrucker, F. Belloni, E. Berthoumieux, J. Billowes, D. Bosnar, A. Brown, M. Brugger, M. Caamaño, F. Calviño, M. Calviani, D. Cano-Ott, R. Cardella, A. Casanovas, D.M. Castelluccio, F. Cerutti, Y.H. Chen, E. Chiaveri, N. Colonna, M.A. Cortés-Giraldo, G. Cortés, L. Cosentino, L.A. Damone, K. Deo, M. Diakaki, C. Domingo-Pardo, R. Dressler, E. Dupont, I. Durán, B. Fernández-Domínguez, A. Ferrari, P. Ferreira, P. Finocchiaro, R.J.W. Frost, V. Furman, S. Ganesan, A.R. García, A. Gawlik, I. Gheorghe, S. Gilardoni, T. Glodariu, I.F. Gonçalves, E. González, A. Goverdovski, E. Griesmayer, C. Guerrero, K. Göbel, H. Harada, T. Heftrich, S. Heinitz, A. Hernández-Prieto, J. Heyse, D.G. Jenkins, E. Jericha, F. Käppeler, Y. Kadi, A. Kalamara, T. Katabuchi, P. Kavrigin, V. Ketlerov, V. Khryachkov, A. Kimura, N. Kivel, M. Kokkoris, M. Krtička, D. Kurtulgil, E. Leal-Cidoncha, C. Lederer, H. Leeb, J. Lerendegui, M. Licata et al.
The measurement programme at the neutron time-of-flight facility n_TOF at CERN
EPJ Web of Conferences **146**, 11002 (2017), DOI: 10.1051/epjconf/201714611002

S. Heinitz, D. Kiselev, N. Kivel, D. Schumann
Separation of weighable amounts of [10]Be from proton irradiated graphite
Appl. Rad. And Isot. **130**, 260 (2017), DOI: 10.1016/j.apradiso.2017.10.012

S. Heinitz, E. A. Maugeri, D. Schumann, R. Dressler, N. Kivel, C. Guerrero, U. Köster, M. Tessler, M. Paul, S. Halfon
Production, separation and target preparation of [171]Tm and Pm[147] for neutron cross section measurements
Radiochim. Acta **105**, 801 (2017), DOI: 10.1515/ract-2016-2728

H. Honarvar, C. Müller, S. Cohrs, S. Haller, K. Westerlund, A. Eriksson Karlström, N. P. van der Meulen, R. Schibli, V. Tolmachev
Evaluation of the first [44]Sc-labeled Affibody molecule for imaging of HER2-expressing tumors
Nuclear Medicine and Biology **45**, 15 (2017), DOI: 10.1016/j.nucmedbio.2016.10.004

E. Leal-Cidoncha, I. Durán, C. Paradela, L. Tassan-Got, L. Audouin, L.C. Leal, C. Le Naour, G. Noguere, D. Tarrío, L.S. Leong, S. Altstadt, J. Andrzejewski, M. Barbagallo, V. Bécares, F. Bečář, F. Belloni, E. Berthoumieux, J. Billowes, V. Boccone, D. Bosnar, M. Brugger, M. Calviani, F. Calviño, D. Cano-Ott, C. Carrapiço, F. Cerutti, E. Chiaveri, M. Chin, N. Colonna, G. Cortés, M.A. Cortés-Giraldo, M. Diakaki, C. Domingo-Pardo, R. Dressler, C. Eleftheriadis, A. Ferrari, K. Fraval, S. Ganesan, A.R. García, G. Giubrone, M.B. Gómez-Hornillos, I.F. Gonçalves, E. González-Romero, E. Griesmayer, C. Guerrero, F. Gunsing, P. Gurusamy, A. Hernández-Prieto, D.G. Jenkins, E. Jericha, Y. Kadi, F. Käppeler, D. Karadimos, N. Kivel, M. Kokkoris, M. Krtička, J. Kroll, C. Lampoudis, C. Langer, C. Lederer, H. Leeb, R. Losito, A. Mallick, A. Manousos, J. Marganiec, T. Martínez, C. Massimi, P.F. Mastinu, M. Mastromarco, M. Meaze, E. Mendoza, A. Mengoni, P.M. Milazzo, F. Mingrone, M. Mirea, W. Mondelaers, A. Pavlik, J. Perkowski, A. Plompen, J. Praena et al.
High accuracy ^{234}U (n,f) cross section in the resonance energy region

J. Lerendegui-Marco, M.A. Cortés-Giraldo, C. Guerrero, J.M. Quesada, S. Lo Meo, C. Massimi, M. Barbagallo, N. Colonna, D. Mancussi, F. Mingrone, M. Sabaté-Gilarte, G. Vannini, V. Vlachoudis, O. Aberle, J. Andrzejewski, L. Audouin, M. Bacak, J. Balibrea, F. Bečář, E. Berthoumieux, J. Billowes, D. Bosnar, A. Brown, M. Caamaño, F. Calviño, M. Calviani, D. Cano-Ott, R. Cardella, A. Casanovas, F. Cerutti, Y.H. Chen, E. Chiaveri, G. Cortés, L. Cosentino, L.A. Damone, M. Diakaki, C. Domingo-Pardo, R. Dressler, E. Dupont, I. Durán, B. Fernández-Domínguez A. Ferrari, P. Ferreira, P. Finocchiaro, K. Göbel, M.B. Gómez-Hornillos, A.R. García, A. Gawlik, S. Gilardoni, T. Glodariu, I.F. Gonçalves, E. González, E. Griesmayer, F. Gunsing, H. Harada, S. Heinitz, J. Heyse, D.G. Jenkins, E. Jericha, F. Käppeler, Y. Kadi, A. Kalamara, P. Kavrigin, A. Kimura, N. Kivel, M. Kokkoris, M. Krtička, D. Kurtulgil, E. Leal-Cidoncha, C. Lederer, H. Leeb, S.J. Lonsdale, D. Macina, J. Marganiec, T. Martínez, A. Masi, P. Mastinu, M. Mastromarco, E.A. Maugeri, A. Mazzone et al.
Monte carlo simulations of the n_TOF lead spallation target with the Geant4 toolkit: A benchmark study

J. Lerendegui-Marco, C. Guerrero, M.A. Cortés-Giraldo, J.M. Quesada, E. Mendoza, D. Cano-Ott, K. Eberhardt, A. Junghans, O. Aberle, J. Andrzejewski, L. Audouin, M. Bacak, J. Balibrea, M. Barbagallo, F. Bečář, E. Berthoumieux, J. Billowes, D. Bosnar, A. Brown, M. Caamaño, F. Calviño, M. Calviani, R. Cardella, A. Casanovas, F. Cerutti, Y.H. Chen, E. Chiaveri, N. Colonna, G. Cortés, L. Cosentino, L.A. Damone, M. Diakaki, C. Domingo-Pardo, R. Dressler, E. Dupont, I. Durán, B. Fernández-Domínguez, A. Ferrari, P. Ferreira, P. Finocchiaro, K. Göbel, M.B. Gómez-Hornillos, A.R. García, A. Gawlik, S. Gilardoni, T. Glodariu, I.F. Gonçalves, E. González, E. Griesmayer, F. Gunsing, H. Harada, S. Heinitz, J. Heyse, D.G. Jenkins, E. Jericha, F. Käppeler, Y. Kadi, A. Kalamara, P. Kavrigin, A. Kimura, N. Kivel, M. Kokkoris, M. Krtička, D. Kurtulgil, E. Leal-Cidoncha, C. Lederer, H. Leeb, S. Lo Meo, S.J. Lonsdale, D. Macina, J. Marganiec, T. Martínez, A. Masi, C. Massimi, P. Mastinu, M. Mastromarco, E.A. Maugeri, A. Mazzone, A. Mengoni, P.M. Milazzo et al.
New measurement of the $^{242}Pu(n,\gamma)$ cross section at n_TOF-EAR1 for MOX fuels: Preliminary results in the RRR

C. Massimia, S. Altstadt, J. Andrzejewski, L. Audouin, M. Barbagallo, V. Bécares, F. Bečvá, F. Belloni, E. Berthoumieux, J. Billowes, S. Bisterzo, D. Bosnar, M. Brugger, M. Calviani, F. Calviño, D. Cano-Ott, C. Carrapiço, D.M. Castelluccio, F. Cerutti, E. Chiaveri, L. Cosentino, M. Chin, G. Clai, N. Colonna, G. Cortés, M.A. Cortés-Giraldo, S. Cristallo, M. Diakaki, C. Domingo-Pardo, I. Duran, R. Dressler, C. Eleftheriadis, A. Ferrari, P. Finocchiaro, K. Fraval, S. Ganesan, A.R. García, G. Giubrone, I.F. Gonçalves, E. González-Romero, E. Griesmayer, C. Guerrero, F. Gunsing, A. Hernández-Prieto, D.G. Jenkins, E. Jericha, Y. Kadi, F. Käppeler, D. Karadimos, N. Kivel et al.
Neutron spectroscopy of ^{26}Mg states: Constraining the stellar neutron source $^{22}Ne(\alpha,n)^{25}Mg$

M. Mastromarco, M. Barbagallo, M.J. Vermeulen, N. Colonna, S. Altstadt, J. Andrzejewski, L. Audouin, V. Bécares, F. Bečář, F. Belloni, E. Berthoumieux, J. Billowes, D. Bosnar, M. Brugger, F. Calviño, M. Calviani, D. Cano-Ott, C. Carrapiço, F. Cerutti, E. Chiaveri, M. Chin, G. Cortés, M.A. Cortés-Giraldo, M. Diakaki, C. Domingo-Pardo, I. Durán, N. Dzysiuk, C. Eleftheriadis, A. Ferrari, K. Fraval, V. Furman, M.B. Gómez-Hornillos, S. Ganesan, A.R. García, G. Giubrone, I.F. Gonçalves, E. González, A. Goverdovski, E. Griesmayer, C. Guerrero, F. Gunsing, P. Gurusamy, T. Heftrich, S. Heinitz, A. Hernández-Prieto, J. Heyse, D.G. Jenkins, E. Jericha, F. Käppeler, Y. Kadi, D. Karadimos, T. Katabuchi, V. Ketlerov, V. Khryachkov, P. Koehler, M. Kokkoris, J. Kroll, M. Krtička, C. Lampoudis, C. Langer, E. Leal-Cidoncha, C. Lederer, H. Leeb, L.S. Leong, J. Lerendegui-Marco, M. Licata, R. Losito, A. Manousos, J. Marganiec, T. Martínez, C. Massimi, P. Mastinu, E. Mendoza, A. Mengoni, P.M. Milazzo, F. Mingrone, M. Mirea, W. Mondelaers, C. Paradela, A. Pavlik et al.
The ^{236}U neutron capture cross-section measured at the n_TOF CERN facility

E.A. Maugeri, S. Heinitz, R. Dressler, M. Barbagallo, N. Kivel, D. Schumann, M. Ayranov, A. Musumarra, M. Gai, N. Colonna, M. Paul, S. Halfon, L. Cosentino, P. Finocchiaro, A. Pappalardo
Preparation of ^{7}Be targets for nuclear astrophysics research
J. Instr. **12**, P02016 (2017), DOI: 10.1088/1748-0221/12/02/P02016

E.A. Maugeri, J. Neuhausen, B. Prieto, A. Aerts, T. Mendona, T. Stora, R. Eichler
Adsorption of volatile polonium species on metals in various gas atmospheres: Part III Adsorption of volatile polonium on stainless steel 316L
Radiochim. Acta **106**, 125 (2017), DOI: 10.1515/ract-2017-2807

E. Mendoza, D. Cano-Ott, S. Altstadt, S. Andriamonje, J. Andrzejewski, L. Audouin, J. Balibrea, V. Bécares, M. Barbagallo, F. Bečvář, F. Belloni, B. Berthier, E. Berthoumieux, J. Billowes, V. Boccone, D. Bosnar, M. Brugger, F. Calviño, M. Calviani, C. Carrapiço, F. Cerutti, E. Chiaveri, M. Chin, N. Colonna, G. Cortés, M.A. Cortés-Giraldo, M. Diakaki, I. Dillmann, C. Domingo-Pardo, I. Durán, N. Dzysiuk, C. Eleftheriadis, M. Fernández-Ordóñez, A. Ferrari, K. Fraval, V. Furman, M.B. Gómez-Hornillos, S. Ganesan, A.R. García, G. Giubrone, I.F. Gonçalves, E. González, A. Goverdovski, F. Gramegna, E. Griesmayer, C. Guerrero, F. Gunsing, P. Gurusamy, T. Heftrich, S. Heinitz, A. Hernández-Prieto, J. Heyse, D.G. Jenkins, E. Jericha, F. Käppeler, Y. Kadi, D. Karadimos, T. Katabuchi, V. Ketlerov, V. Khryachkov, P. Koehler, M. Kokkoris, J. Kroll, M. Krtička, C. Lampoudis, C. Langer, E. Leal-Cidoncha, C. Lederer, H. Leeb, L.S. Leong, J. Lerendegui-Marco, M. Licata, R. Losito, A. Manousos, J. Marganiec, T. Martínez, C. Massimi, P. Mastinu, M. Mastromarco, A. Mengoni et al.
Measurement of the ^{241}Am neutron capture cross section at the n_TOF facility at CERN
EPJ Web of Conferences **146**, 11022 (2017), DOI: 10.1051/epjconf/201714611022

F. Mingrone, S. Altstadt, J. Andrzejewski, L. Audouin, V. Bécares, M. Barbagallo, F. Bečvář, F. Belloni, E. Berthoumieux, J. Billowes, V. Boccone, D. Bosnar, M. Brugger, F. Calviño, M. Calviani, D. Cano-Ott, C. Carrapiço, F. Cerutti, E. Chiaveri, M. Chin, N. Colonna, G. Cortés, M.A. Cortés-Giraldo, M. Diakaki, C. Domingo-Pardo, R. Dressler, I. Durán, C. Eleftheriadis, A. Ferrari, K. Fraval, V. Furman, K. Göbel, M.B. Gómez-Hornillos, S. Ganesan, A.R. García, G. Giubrone, I.F. Gonçalves, E. González, A. Goverdovski, E. Griesmayer, C. Guerrero, F. Gunsing, T. Heftrich, A. Hernández-Prieto, J. Heyse, D.G. Jenkins, E. Jericha, F. Käppeler, Y. Kadi, D. Karadimos, T. Katabuchi, V. Ketlerov, V. Khryachkov, N. Kivel, P. Koehler, M. Kokkoris, J. Kroll, M. Krtička, C. Lampoudis, C. Langer, E. Leal-Cidoncha, C. Lederer, H. Leeb, L.S. Leong, J. Lerendegui-Marco, R. Losito, A. Mallick, A. Manousos, J. Marganiec, T. Martínez, C. Massimi, P. Mastinu, M. Mastromarco, E. Mendoza, A. Mengoni, P.M. Milazzo, M. Mirea, W. Mondelaers, C. Paradela, A. Pavlik et al.
High precision measurement of the radiative capture cross section of ^{238}U at the n_TOF CERN facility
EPJ Web of Conferences **146**, 11028 (2017), DOI: 10.1051/epjconf/201714611028

F. Mingrone, C. Massimi, G. Vannini, N. Colonna, F. Gunsing, P. Zugec, S. Altstadt, J. Andrzejewski, L. Audouin, M. Barbagallo, V. Becares, F. Becvar, F. Belloni, E. Berthoumieux, J. Billowes, D. Bosnar, M. Brugger, M. Calviani, F. Calvino, D. Cano-Ott, C. Carrapico, F. Cerutti, E. Chiaveri, M. Chin, G. Cortes, M. A. Cortes-Giraldo, M. Diakaki, C. Domingo-Pardo, I. Duran, R. Dressler, C. Eleftheriadis, A. Ferrari, K. Fraval, S. Ganesan, A. R. Garcıa, G. Giubrone, I. F. Goncalves, E. Gonzalez-Romero, E. Griesmayer, C. Guerrero, A. Hernandez-Prieto, D. G. Jenkins, E. Jericha, Y. Kadi, F. Kappeler, D. Karadimos, N. Kivel, P. Koehler, M. Kokkoris, M. Krticka et al.
Neutron capture cross section measurement of ^{238}U at the CERN n_TOF facility in the energy region from 1 eV to 700 keV
Phys. Rev. C **95**, 034604 (2017), DOI: 10.1103/PhysRevC.95.034604

C. Müller, N. P. van der Meulen, M. Benesová, R. Schibli
Therapeutic Radiometals Beyond ^{177}Lu and ^{90}Y: Production and Application of Promising α-Particle, β-Particle, and Auger Electron Emitters
J. Nucl. Med. **58**, 91 (2017), DOI: 10.2967/jnumed.116.186825

K. M. Ostdiek, T. S. Anderson, W. K. Bauder, M. R. Bowers, A. M. Clark, P. Collon, W. Lu, A. D. Nelson, D. Robertson, M. Skulski, R. Dressler, D. Schumann, J. P. Greene, W. Kutschera, M. Paul
Activity measurement of Fe-60 through the decay of Co-60m and confirmation of its half-life
Phys Rev. C **95**, 055809 (2017), DOI: 10.1103/PhysRevC.95.055809

M. Sabaté-Gilarte, M. Barbagallo, N. Colonna, F. Gunsing, P. Žugec, V. Vlachoudis, Y. H. Chen, A. Stamatopoulos, J. Lerendegui-Marco, M. A. Cortés-Giraldo, A. Villacorta, C. Guerrero, L. Damone, L. Audouin, E. Berthoumieux, L. Cosentino, M. Diakaki, P. Finocchiaro, A. Musumarra, T. Papaevangelou, M. Piscopo, L. Tassan-Got, O. Aberle, J. Andrzejewski, V. Bécares, M. Bacak, R. Baccomi, J. Balibrea, S. Barros, F. Bečvář, C. Beinrucker, F. Belloni, J. Billowes, D. Bosnar, M. Brugger, M. Caamaño, F. Calviño, M. Calviani, D. Cano-Ott, R. Cardella, A. Casanovas, D. M. Castelluccio, F. Cerutti, E. Chiaveri, G. Cortés, K. Deo, C. Domingo-Pardo, R. Dressler, E. Dupont, I. Durán et al.
High-accuracy determination of the neutron flux in the new experimental area n_TOF-EAR2 at CERN
Eur. Phys. J. A **53**, 210 (2017), DOI: 10.1140/epja/i2017-12392-4

P. Steinegger, R. Dressler, R. Eichler, D. Piguet, S. Streuli, A. Türler
Diamond detectors for high-temperature transactinide chemistry experiments
Nucl. Instr. & Meth. Phys. Res. A **850**, 61 (2017), DOI: 10.1016/j.nima.2016.12.014

M. Sabaté-Gilarte, J. Praena, I. Porras, J.M. Quesada, O. Aberle, J. Andrzejewski, L. Audouin, V. Bécares, M. Bacak, J. Balibrea-Correa, M. Barbagallo, S. Barros, F. Bečvář, C. Beinrucker, E. Berthoumieux, J. Billowes, D. Bosnar, M. Brugger, M. Camaño, F. Calviño, M. Calviani, D. Cano-Ott, R. Cardella, A. Casanovas, D.M. Castelluccio, F. Cerutti, Y.H. Chen, E. Chiaveri, N. Colonna, G. Cortés, M.A. Cortés-Giraldo, L. Cosentino, L.A. Damone, M. Diakaki, C. Domingo-Pardo, R. Dressler, E. Dupont, I. Durán, B. Fernández-Domínguez, A. Ferrari, P. Ferreira, P. Finocchiaro, V. Furman, K. Gödel, A. García-Rios, A. Gawlik, T. Glodariu, I.F. Gonçalves, E. González, A. Goverdovski, E. Griesmayer, C. Guerrero, F. Gunsing, H. Harada, T. Heftrich, S. Heinitz, J. Heyse, D.G. Jenkins, E. Jericha, F. Käppeler, Y. Kadi, T. Katabuchi, P. Kavrigin, V. Ketlerov, V. Khryachkov, A. Kimura, N. Kivel, M. Kokkoris, M. Krtička, E. Leal-Cidoncha, C. Lederer, H. Leeb, J. Lerendegui-Marco, S. Lo Meo, S.J. Lonsdale, R. Losito, D. Macina, J. Marganiec, T. Martínez, C. Massimi et al.
The $^{33}S(n,\alpha)^{30}Si$ cross section measurement at n_TOF-EAR2 (CERN): From 0.01 eV to the resonance region
EPJ Web of Conferences **146**, 08004 (2017), DOI: 10.1051/epjconf/201714608004

D. Schumann, R. Dressler, E.A. Maugeri, S. Heinitz
Isotope production and target preparation for nuclear astrophysics data
EPJ Web of Conferences **146**, 03005 (2017), DOI: 10.1051/epjconf/201714603005

A. Singh, N. P. van der Meulen, C. Müller, I. Klette, H. R. Kulkarni, A. Türler, R. Schibli, R. P. Baum
First-in-Human PET/CT Imaging of Metastatic Neuroendocrine Neoplasms with Cyclotron-Produced ^{44}Sc-DOTATOC: A Proof-of-Concept Study
Cancer Biotherapy and Radiopharmaceuticals **32**, 124 (2017), DOI: 10.1089/cbr.2016.2173

A. Stamatopoulos, A. Tsinganis, N. Colonna, R. Vlastou, M. Kokkoris, P. Schillebeeckx, A. Plompen, J. Heyse, P. Žugec, M. Barbagallo, M. Calviani, E. Berthoumieux, E. Chiaveri, O. Aberle, J. Andrzejewski, L. Audouin, V. Bécares, M. Bacak, J. Balibrea, S. Barros, F. Bečvář, C. Beinrucker, F. Belloni, J. Billowes, V. Boccone, D. Bosnar, M. Brugger, M. Caamaño, F. Calviño, D. Cano-Ott, F. Cerutti, G. Cortés, M.A. Cortés-Giraldo, L. Cosentino, L.A. Damone, K. Deo, M. Diakaki, C. Domingo-Pardo, R. Dressler, E. Dupont, I. Durán, B. Fernández-Domínguez, A. Ferrari, P. Ferreira, P. Finocchiaro, R.J.W. Frost, V. Furman, K. Göbel, M.B. Gómez-Hornillos, A.R. García, I. Gheorghe, T. Glodariu, I.F. Gonçalves, E. González, A. Goverdovski, E. Griesmayer, C. Guerrero, F. Gunsing, H. Harada, T. Heftrich, S. Heinitz, A. Hernández-Prieto, D.G. Jenkins, E. Jericha, F. Käppeler, Y. Kadi, T. Katabuchi, P. Kavrigin, V. Ketlerov, V. Khryachkov, A. Kimura, N. Kivel, M. Krtička, E. Leal-Cidoncha, C. Lederer, H. Leeb, J. Lerendegui-Marco, M. Licata, S. Lo Meo, R. Losito et al.
Measurement of the $^{240}Pu(n, f)$ cross-section at the CERN n_TOF facility: First results from experimental area II (EAR-2)
EPJ Web of Conferences **146**, 04030 (2017), DOI: 10.1051/epjconf/201714604030

G. F. Steyn, S. G. Dolley, F. Szelecsényi, Z. Kovács, N. P. van der Meulen, C. Vermeulen
In-flight annihilation correction for 511 keV photon spectrometry.
EPJ Web of Conferences **146**, 08010 (2017), DOI: 10.1051/epjconf/201714608010

Z. Talip, R. Dressler, J. C. David, C. Vockenhuber, E. Müller, A. Vögele, E. Strub, P. Vontobel, D. Schumann
Radiochemical Determination of Long-lived Radionuclides in Proton- Irradiated Heavy Metal Targets: Part I-Tantalum
Anal. Chem. **89**, 13541 (2017), DOI: 10.1021/acs.analchem.7b03952

Z. Talip, S. Peuget, M. Magnin, L. Berardo, C. Valot, R. Vauchy, C. Jegou
Raman micro-spectroscopic studies of un-irradiated homogeneous (U0.76 Pu0.24)O2+x, the effects of Pu content, non-stoichiometry, self-radiation damage and secondary phases
J. Raman Spectrosc. **48**, 765 (2017), DOI: 10.1002/jrs.5092

Z. Talip, S. Pfister, R. Dressler, J.C. David, A. Vögele, P. Vontobel, R. Michel, D. Schumann
Analysis of the ^{148}Gd and ^{154}Dy Content in Proton-Irradiated Lead Targets
Anal. Chem. **89**, 6861 (2017), DOI: 10.1021/acs.analchem.7b01353

C. A. Umbricht, M. Benešová, R. Schmid, A. Türler, R. Schibli, N. P. van der Meulen, C. Müller
^{44}Sc-PSMA-617 for RadioTheragnostics in Tandem with ^{177}Lu-PSMA-617 - Preclinical Investigations in Comparison with ^{68}Ga-Based PSMA Ligands
EJNMMI Research **7**, 9 (2017).

T. Wright, C. Guerrero, J. Billowes, D. Cano-Ott, E. Mendoza, S. Altstadt, J. Andrzejewski, L. Audouin, V. Bécares,
M. Barbagallo, F. Bečvář, F. Belloni, E. Berthoumieux, D. Bosnar, M. Brugger, F. Calviño, M. Calviani, C. Carrapiço,
F. Cerutti, E. Chiaveri, M. Chin, N. Colonna, G. Cortés, M. A. Cortés-Giraldo, M. Diakaki, M. Dietz, C. Domingo-Pardo,
I. Durán, N. Dzysiuk, C. Eleftheriadis, Ferrari, K. Fraval, V. Furman, M. B. Gómez-Hornillos, S. Ganesan, A. R. García,
G. Giubrone, I. F. Gonçalves, E. González-Romero, A. Goverdovski, E. Griesmayer, F. Gunsing, P. Gurusamy, T. Heftrich,
A. Hernández-Prieto, D. G. Jenkins, E. Jericha, F. Käppeler, Y. Kadi, D. Karadimos, T. Katabuchi, V. Ketlerov,
V. Khryachkov, P. Koehler, M. Kokkoris, J. Kroll, M. Krtička, C. Lampoudis, C. Langer, E. Leal-Cidoncha, C. Lederer,
H. Leeb, L. S. Leong, J. Lerendegui-Marco, R. Losito, A. Manousos, J. Marganiec, T. Martínez, C. Massimi, P. Mastinu,
A. Mengoni, P. M. Milazzo, F. Mingrone, M. Mirea, C. Paradela, A. Pavlik, J. Perkowski, J. Praena, J. M. Quesada,
T. Rauscher, R. Reifarth, A. Riego-Perez, M. Robles, F. Roman, C. Rubbia, J. A. Ryan, M. Sabaté-Gilarte, R. Sarmento,
A. Saxena, P. Schillebeeckx, S. Schmidt, D. Schumann et al.
Measurement of the ^{238}U(n, γ) cross section up to 80 keV with the Total Absorption Calorimeter at the CERN n_TOF facility
Phys. Rev. C **96**, 064601 (2017), DOI: 10.1103/PhysRevC.96.064601

P. Zugec, N. Colonna, M. Sabate-Gilarte, V. Vlachoudis, C. Massimi, J. Lerendegui-Marco, A. Stamatopoulos,
M. Bacak, S.G. Warren, and the n_TOF Collaboration
A direct method for unfolding the resolution function from measurements of neutron induced reactions
Nucl. Instr. & Meth. Phys. Res. A **875**, 41 (2017), DOI: 10.1016/j.nima.2017.09.004

INTERNAL REPORTS

N.P. van der Meulen
The production of exotic radionuclides for diagnostic and therapeutic application in nuclear medicine
NES Colloquium, 18 January, 2017

K. Domnanich
Studies towards "matched pair" theragnostics
UniBe Seminar Day, 10 March, 2017

K. Domnanich
Studies towards "matched pair" theragnostics
ASI, 5 July, 2017

CONTRIBUTIONS TO CONFERENCES, WORKSHOPS AND SEMINARS

I.I. Danilov, J. Neuhausen, A. Türler
Evaporation of Caesium from Liquid Lead Bismuthalloy – sample preparation and first transpiration experiments
NES PhD Day, Paul Scherrer Institut, Villigen, Switzerland, 22 May, 2017.

I.I. Danilov
Radionuclides release in liquid metal cooled nuclear reactor
1st year graduate student symposium, Departement Chemie und Biochemie, University of Bern, Switzerland,
4-5 September, 2017.

I.I. Danilov
Radionuclides release in liquid metal cooled nuclear reactor
Seminar of the Laboratory of Radiochemistry, University of Bern, Switzerland, 29 September, 2017.

I.I. Danilov
Radionuclides release in liquid metal cooled nuclear reactor
Seminar of the Laboratory of Radiochemistry, Villigen, Switzerland, 29 Oktober, 2017.

K. Domnanich
Studies towards "matched pair" theragnostics
Seminar of the Laboratory of Radiochemistry, University of Bern, Switzerland, 10 March, 2017.

K. Domnanich
Studies Towards the Production of ^{43}Sc & ^{47}Sc - a Novel "Matched Pair" for Radiotheragnostic Applications
GDCH - FG Nuklearchemie, Berlin, Germany, 13 September, 2017.

R. Eichler
Superheavy Element Chemistry
Colloquium: Element Inauguration Moscovium, Tennessine, Oganesson. FLNR Dubna, Russian Federation,
3 March, 2017.

R. Eichler
Prospects of gas phase chemistry with SHE
3rd International Symposium on Super-Heavy Elements "Challenges in the studies of super-heavy nuclei and atoms" (SHE 2017), Kazimierz-Dolny, Poland, 10-14 September, 2017.

R. Eichler
The Laboratory for Radiochemistry
Annual NES Event: NES präsentiert Kompetenzen und Highlights. Villigen PSI, Switzerland, 24 October, 2017.

R. Eichler
Prospects for Superheavy Element Chemistry
Working Meeting on the Prospects of Research on the Chemistry of Superheavy Elements at the new SHE factory, FLNR Dubna, Russian Federation, 6-9 December, 2017.

N. Gracheva
Improved Chemical Separation Method to Obtain ^{161}Tb – a Medically Interesting Radiolanthanide
25th AGRR, Munich, Germany, 5 October, 2017.

S.Heinitz
Preparation of radioactive lanthanide targets for nuclear physics experiments
6th Workshop on Nuclear Fission and Spectroscopy of Neutron-Rich Nuclei, Chamrousse, France, 22 March, 2017.

S. Heinitz
Radiochemical separation of ^{7}Be and ^{10}Be produced at the PSI accelerator facility
5th International Nuclear Chemistry Conference (INCC2017), Gothenburg, Sweden, 28 August, 2017.

E. Karlsson
Determination of adsorption properties of fission products released from HLM-coolant – toward realisation of the MYRRHA-reactor
Seminar of the Laboratory of Radiochemistry, University of Bern, Switzerland, 29 September, 2017.

B. Kraus
Isothermal vacuum chromatography of Pb on quartz as model to investigate superheavy elements
NES PhD Day, Paul Scherrer Institut, Villigen, Switzerland, 22 May, 2017.

B. Kraus
Isothermal vacuum chromatography of Pb on quartz as model to investigate superheavy elements
GDCh – Wissenschaftsforum Chemie 2017, Berlin, Germany, 10–14 September, 2017.

B. Kraus
Isothermal vacuum chromatography of Pb on quartz as model to investigate superheavy elements
9th Workshop on the Chemistry of the Heaviest Elements (CHE9), Ascona, Switzerland, 8–11 October, 2017.

B. Kraus
Isothermal Vacuum Chromatography of Superheavy Elements
Seminar of the Laboratory of Radiochemistry, University of Bern, Switzerland, 1 December, 2017.

E.A. Maugeri
Preparation and characterization of ^7Be targets for the measurement of $^7Be(n,p)^7Li$ and $^7Be(n,\alpha)^4He$ reaction cross sections
8th Nuclear Physics in Astrophysics International, Catania, Italy, 19 June, 2017.

E.A. Maugeri
Use of ^7Be for Nuclear Astrophysics Studies
9th International Conference on Isotopes, Doha, Qatar, 17-23 November, 2017.

E.A. Maugeri
Characterization of the ^7Be target used for the measurement of the $^7Be(n, p)^7Li$ reaction cross sections
n_TOF Collaboration meeting, Madrid, Spain, 11-12 December, 2017.

J. Neuhausen
Evaporation and capture of volatile radionuclides in ADS
NES-BERK, Paul Scherrer Institut, Villigen, Switzerland, 27 January, 2017.

J. Neuhausen
Release of volatile radionuclides from liquid metal reactors and their capture
VKI Lecture series: Thermohydraulics and Chemistry of Liquid Metal Cooled Reactors, Rhode-St.-Genèse, Belgium, 10 April, 2017.

J. Neuhausen
Chemistry of volatile radionuclides: Status and prospects of MYRTE-WP4
MYRTE-WP4 technical meeting, SCK·CEN Headquarters, Brussels, Belgium, 24 April, 2017.

J. Neuhausen
Chemistry of volatile radionuclides
MYRTE-TEC meeting, SCK·CEN Headquarters, Brussels, Belgium, 25 April, 2017.

J. Neuhausen
Liquid Metal Chemistry
NES-Colloquium, Paul Scherrer Institut, Villigen, Switzerland, 18 May, 2017.

J. Neuhausen
Chemistry of radionuclides in HLM Reactors
Heavy metal summer school, SCK·CEN, Mol, Belgium, 13 June, 2017.

J. Neuhausen
Chemistry of volatile radionuclides
MYRTE-TEC meeting, SCK·CEN Headquarters, Brussels, Belgium, 27 October, 2017.

J. Neuhausen
Chemistry of volatile radionuclides
MYRTE Governing Board meeting, SCK·CEN Headquarters, Brussels, Belgium, 27 October, 2017.

M. Lin
Treatment of Burned Nuclear Fuel Solution
Seminar of the Laboratory of Radiochemistry, University of Bern, Switzerland, 19 May, 2017.

M. Lin
Investigations of Cs Removal from Solutions Containing Burned Nuclear Fuel
NES PhD Day, Paul Scherrer Institut, Villigen, Switzerland, 22 May, 2017.

M. Lin
Investigations of A Novel Ion Exchanger for Cs Removal from Burned Nuclear Fuel Solution
5th International Nuclear Chemistry Congress, Gothenburg, Sweden, 28 August, 2017.

M. Lin
Treatment of The Spent Fuel Solution-Cs Removal
1st year graduate student symposium, Departement Chemie und Biochemie, University of Bern, Switzerland,
4-5 September, 2017.

M. Lin
The Treatment of Spent Nuclear Fuel Solution
Seminar of the Laboratory of Radiochemistry, University of Bern, Switzerland, 29 September, 2017.

D. Schumann
Radioactive isotope and target production for nuclear astrophysics
Inauguration of the "Felsenkeller"-underground laboratory, Dresden, Germany, 26-28 June, 2017.

D. Schumann
AMS standards for non-standard isotopes
AMS14, Ottawa, Canada, 13-18 August, 2017.

D. Schumann
Target production at PSI
CHANDA WP3 meeting, Jyväskulä, Finland, 21-23 August, 2017.

P. Steinegger, R. Dressler, R. Eichler
Diamond based α-detectors – properties, behavior, usage
9th Workshop on the Chemistry of the Heaviest Elements, Monte-Verità, Ascona, Ticino, Switzerland, 8 October, 2017.

Z. Talip
Determination of the long lived radionuclides from proton-irradiated heavy metal targets
Laboratory of Ion Beam Physics, ETH Zurich, Switzerland, 31 May, 2017.

Z. Talip, R. Dressler, J.-C. David, C. Vockenhuber, E. Muller, E. Strub, D. Schumann
Determination of the long lived radionuclides from proton-irradiated heavy metal targets
9th International Conference on Isotopes and Expo, Doha, Qatar 12-16 November, 2017.

Jiri Ulrich
Determination of astrophysical relevant properties of Mn-53
Seminar of the Laboratory of Radiochemistry, University of Bern, Switzerland, 1 December, 2017.

N.P. van der Meulen
^{43}Sc Production by the Cyclotron Irradiation of Enriched Ca and Ti
ISRS 2017, Dresden, Germany, 15 May, 2017.

N.P. van der Meulen
Tb radionuclides separated at ISOLDE; processed and used for radiolabelling and imaging experiments at PSI
Lecture, University of Bern, Switzerland, 31 May, 2017.

N.P. van der Meulen
Present work breakdown structure
NCCR "Radiation-based cancer therapy" meeting, Paul Scherrer Institute, Villigen, Switzerland, 30 August, 2017.

N.P. van der Meulen
An update on the chemical separation of ^{152}Tb and its subsequent application for PET imaging
ISOLDE Workshop and Users Meeting 2017, Geneva, Switzerland, 5 December, 2017.

C. Vermeulen
Recent trends in production of radionuclides for PET and radiotherapy
XIV Turku PET Symposium, Turku, Finland, 28 May, 2017.

Y. Wittwer, R. Eichler, A. Türler
Getting insights into the metal-carbonyl complex formation (poster)
NES PhD Day, Paul Scherrer Institut, Villigen, Switzerland, 22 May, 2017.

Y. Wittwer
Getting insights into the metal-carbonyl complex formation
1st year graduate student symposium, Departement Chemie und Biochemie, University of Bern, Switzerland, 4-5 September, 2017.

Y. Wittwer, R. Eichler, A. Türler
Getting insights into the metal-carbonyl complex formation (poster)
GDCH Wissenschaftsforum Chemie, Berlin, Germany, 10-14 September, 2017.

Y. Wittwer
Getting insights into the metal-carbonyl complex formation
9th Workshop on the Chemistry of the Heaviest Elements (CHE9), Ascona, Switzerland, 9-11 October, 2017.

Y. Wittwer
Getting Insight into the Carbonyl Complex Formation of Single Atoms
Seminar of the Laboratory of Radiochemistry, University of Bern, Switzerland, 1 December, 2017.

MEMBERS OF SCIENTIFIC COMMITTEES
EXTERNAL ACTIVITIES

Dr. Robert Eichler
- Associate Editor of the International Journal of Modern Physics E (IJMPE)World Scientific Publishing

Dr. Dorothea Schumann
- Nuklearforum Schweiz, member
- Schweizerische Gesellschaft der Kernfachleute, member

Dr. Nicholas van der Meulen
- United States Department of Energy (DOE Isotope R&D FOA), Panel Reviewer
- Accelerator for Research in Radiochemistry and Oncology at Nantes Atlanti (ARRONAX) International Scientific Committee, member
- PSI internal research commission (FoKo), member

SUMMER STUDENTS

Bianca Schacherl

Separation of lanthanides from proton irradiated tungsten targets

3 April - 30 June 2017

MASTER THESIS

Janosch Gartmeier

Electrochemical preparation of ^7Be targets

Dr. E. A. Maugeri/ PSI
Prof. Dr. A. Türler/ Uni Bern
PD. Dr. P. Broekmann/ Uni Bern
December 2017

DOCTORAL THESIS

Katharina Domnanich

Studies towards ^{43}Sc, ^{44}Sc and ^{47}Sc – a novel Matched Pair for Theragnostic Applications

Dr. N. van der Meulen / PSI
Prof. Dr. A. Türler / PSI & Uni Bern
December 2017

AWARDS

Erik Karlsson

Determination of adsorption properties of radionuclides released from HLM-coolant - toward realisation of the MYRRHA-reactor

Best presentation award (1st year PhD)
NES PhD Day, Villigen, Switzerland
May 2017

Katharina Domnanich

Studies towards Scandium-based matched pair theragnostics

Best presentation award (3rd/4th year PhD)
NES PhD Day, Villigen, Switzerland
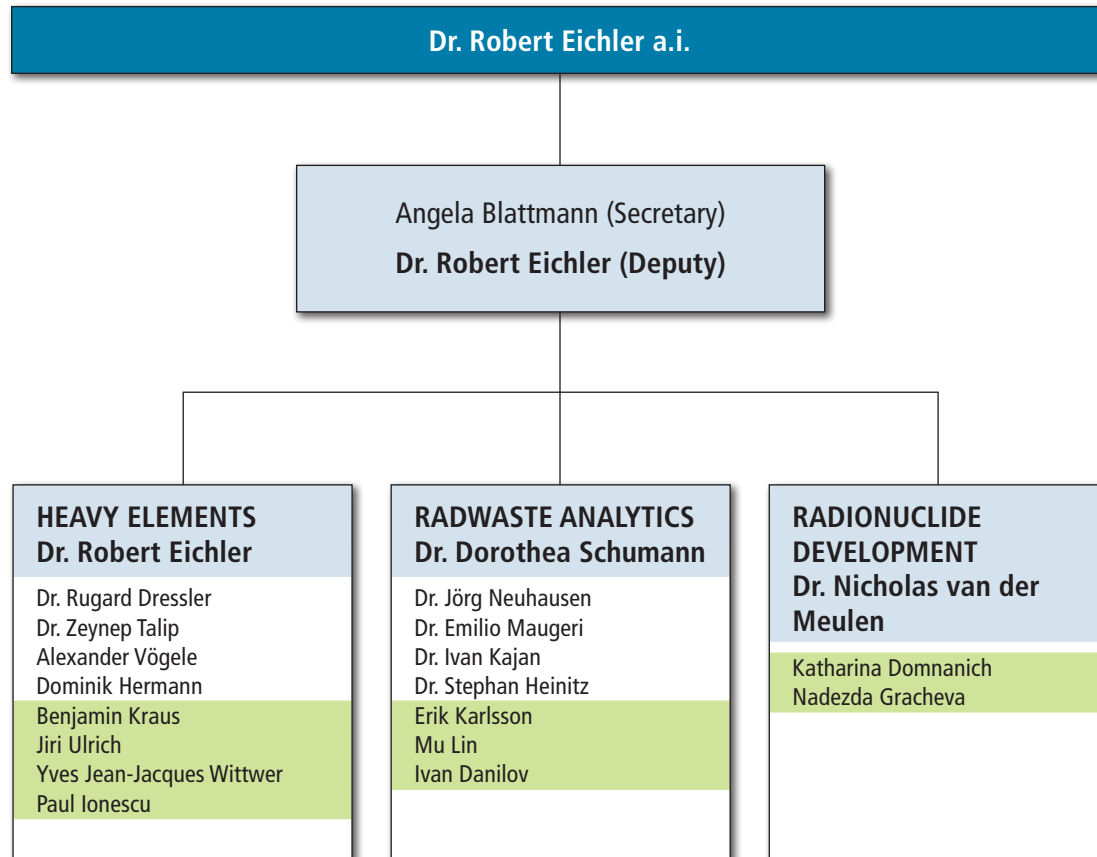May 2017

Patrick Steinegger

Promotionspreis 2017 / Award for the doctoral thesis 2017

Towards Vacuum Adsorption Chromatography of Superheavy Elements

Fachgruppe Nuklearchemie, Gesellschaft Deutscher Chemiker (GDCh)
September 2017

Bernadette Hammer-Rotzler

Promotionspreis 2017 / Award for the doctoral thesis 2017

Analysis of the nuclide inventory in MEGAPIE, a proton irradiated lead-bismuth eutectic spallation target

Fachgruppe Nuklearchemie, Gesellschaft Deutscher Chemiker (GDCh)
September 2017

Patrick Steinegger

Eduard-Adolf-Stein-Preis 2017

Towards Vacuum Adsorption Chromatography of Superheavy Elements

Faculty of Science, University of Bern
May 2017

Dr. Robert Eichler a.i.

Angela Blattmann (Secretary)
Dr. Robert Eichler (Deputy)

HEAVY ELEMENTS
Dr. Robert Eichler

Dr. Rugard Dressler
Dr. Zeynep Talip
Alexander Vögele
Dominik Hermann
Benjamin Kraus
Jiri Ulrich
Yves Jean-Jacques Wittwer
Paul Ionescu

RADWASTE ANALYTICS
Dr. Dorothea Schumann

Dr. Jörg Neuhausen
Dr. Emilio Maugeri
Dr. Ivan Kajan
Dr. Stephan Heinitz
Erik Karlsson
Mu Lin
Ivan Danilov

RADIONUCLIDE DEVELOPMENT
Dr. Nicholas van der Meulen

Katharina Domnanich
Nadezda Gracheva

■ Graduate student

AUTHOR INDEX

AFFILIATION INDEX

AHL	Hot Laboratory Division of the Nuclear Energy and Safety Department (NES), Paul Scherrer Institut, 5232 Villigen, Switzerland
CERN	European Organization for Nuclear Research, CERN, 1211, Genève 23, Switzerland
CIVIDEC	Instrumentation GmbH, Schottengasse 3A/1/41, AT-1010 Wien, Austria
CRS	Center for Radiopharmaceutical Sciences, Paul Scherrer Institut, 5232 Villigen, Switzerland
DFA	Dipartimento di Fisica ed AstronomiaUniversità degli Studi di Catania - Piazza Università, 2 - 95131 Catania, Italy
ETHZ	Eidgen. Technische Hochschule Zürich, 8092 Zürich, Switzerland
EU	European Union
FLNR	Flerov Laboratory of Nuclear Reactions, Joliot-Curie, 6, Dubna, Moscow region 141980, Russia
Goethe University	Goethe University Frankfurt, Theodor-W.-Adorno-Platz 1, 60323 Frankfurt am Main, Germany
Hebrew University	The Hebrew University, The Edmond J. Safra Campus - Givat Ram, Jerusalem 9190401, Israel
HZDR	Helmholtz-Zentrum Dresden-Rossendorf, Bautzner Landstraße 400, 01328 Dresden, Germany
IFIZ	Instituto de Física Corpuscular, Parque Científico, C/Catedrático José Beltrán, 2, 46980 Paterna, Spain
INFN	Laboratori Nazionali del Sud, Via S. Sofia, 62, 95125 Catania, Italy
Irfu	Irfu, CEA Paris-Saclay, Bât 141, 91191 Gif sur Yvette Cedex, France
JINR	International Intergovernmental Organization, Joint Institute for Nuclear Research Joliot-Curie, 6, Dubna, Moscow region 141980, Russia
KIT	Karlsruher Institut für Technologie, Kaiserstraße 12, 76131 Karlsruhe, Germany
LBR	Laboratory for Biomolecular Research, Paul Scherrer Institut, 5232 Villigen, Switzerland
LMX	Laboratory for Multiscale materials eXperiments, Paul Scherrer Institut, 5232 Villigen, Switzerland
LTP	Laboratory for Particle Physics, Paul Scherrer Institut, 5232 Villigen, Switzerland
NIAG	Neutron Imaging and Activation, Paul Scherrer Institut, 5232 Villigen, Switzerland
PSI	Paul Scherrer Institut, 5232 Villigen, Switzerland
Quirem Medical B.V.	Zutphenseweg 55, 7418AH Deventer, Netherlands
RTM Nijmegen	Radboud Translational Medicine B.V., Postbus 9101 (huispost 142), 6500 HB Nijmegen, Netherlands
TU Dresden	Technische Universität Dresden, TUD-INFORMATION, 01062 Dresden, Germany
Univ. Bern	Departement für Chemie und Biochemie, Universität Bern, Freiestr. 3, 3012 Bern, Switzerland
Univ. de Strasbourg	Université de Strasbourg, 4 rue Blaise Pascal, CS 90032, 67081 Strasbourg Cedex, France
Univ. Mainz	Johannes Gutenberg-Universität Mainz, Saarstr. 21, 55122 Mainz, Germany
Univ. of Cologne	Universität zu Köln, Albertus-Magnus-Platz, 50923 Köln, Germany
Univ Sevilla	University of Seville, 4 San Fernando Str. Sevilla 41004, Spain